Chromatic processing in the zebrafish (*Danio rerio*) inner retina:

Bipolar cell physiology and open hardware designs for spectrally accurate stimulation under two-photon

Maxime J.Y. Zimmermann

Submitted for the degree of Doctor of Philosophy

University of Sussex

September 2020

Declaration

The thesis entitled "**Chromatic processing in the zebrafish (*Danio rerio)* inner retina: Bipolar cell physiology and open hardware designs for spectrally accurate stimulation under two-photon**" submitted for the degree of Doctor of Philosophy only presents my own work. Collaborative work and external data are explicitly stated throughout the manuscript.

The following chapters partly contain elements that were published in peer-reviewed journals. All work was conducted after registration for the degree.

Chapter 2 has been published in Current Biology (Volume 28, Issue 13, P2018-2032.E5, July 09, 2018). DOI: https://doi.org/10.1016/j.cub.2018.04.075

Zebrafish Differentially Process Colour across Visual Space to Match Natural Scenes. Zimmermann MJY*, Nevala NE*, Yoshimatsu T*, Osorio D, Nilsson D-E, Berens P and Baden T.**equal contributions*.

In this chapter/publication, I performed a large fraction of the two-photon and confocal imaging experiments on bipolar cells, pre-processed resulting raw data and participated to their analysis.

Chapter 3 has been published in HardwareX (Volume 8 (2020) e00127). DOI: https://doi.org/10.1016/j.ohx.2020.e00127

LED Zappelin': An open source LED controller for arbitrary spectrum visual stimulation and optogenetics during 2-photon imaging. Zimmermann MJY, Chagas AM, Bartel P, Pop S, Prieto Godino LL, Baden T.

For this work, I conceived and implemented the spectral stimulator "LED Zappelin'". I designed the electronics and optical system it relies on and conducted experiments on zebrafish retinae to confirm the efficiency of the device. I composed a complete documentation for this project and rendered it open source, which in turn led to the writing of the published manuscript.

Chapter 4 has been published in eLife *(Volume 8*, e48779*, eLife Sep 23, 2019*).
DOI: https://doi.org/10.7554/eLife.48779

An arbitrary-spectrum spatial visual stimulator for vision research. Franke K, Chagas AM, Zhao Z, Zimmermann MJY, Bartel P, Qiu Y, Szatko K, Baden T, Euler T.

For this collaborative work, I have participated to the conceptualisation of this spatial stimulator by conceiving and implementing the zebrafish version. I have also conceived the ipython scripts necessary for the calibration of the tetrachromatic stimulator and validated its efficiency by investigating zebrafish retinal responses to spatio-chromatic stimuli.

I hereby declare that this thesis has not been and will not be, submitted in whole or in part to another University for the award of any other degree.

Summary

Colour vision describes the ability of animals to differentiate objects based on their spectral reflectance properties independent of light intensity. It is an essential evolutionary trait that allows species to efficiently forage for food, avoid predation, break camouflage, communicate with conspecifics, or to find mates. Zebrafish is a powerful model for studying colour vision as it possesses four cone-photoreceptor types which can be categorised as Red-, Green-, Blue- and UV- sensitive. From first principles, its retina therefore holds the potential to process diverse chromatic computations. In the presented work, the focus was on retinal bipolar cells (BC). These are the retina's first projection neurons. They receive inputs from the photoreceptors in the outer retina, and send their axon terminals to the inner retina, the inner plexiform layer (IPL). Diverse types within this class of interneuron shape light responses collected by the photoreceptor array into parallel channels with diverse spectral properties. BCs also make connections with all other neuron types within the retina, including horizontal cells in the outer retina, and amacrine as well as retinal ganglion cells in the inner retina. This makes them a central hub for spectral processing within the retina.

By combining genetically encoded calcium indicator and two-photon microscopy, light-driven activity from larval zebrafish BC synaptic terminals was systematically recorded *in vivo*. Synaptic responses to tetrachromatic light stimulation unveiled an unprecedented degree of visual specialisation, including retinal regions dedicated to distinct light-guided behaviours. These regional characteristics were further correlated to functional BC types which were strongly associated with specific retinal positions and axonal stratification depths. Overall, BC projections to the inner plexiform layer displayed a sophisticated level of organisation, structured into chromatic and achromatic functional layers which systematically adjusted their response profiles across the eye to match natural spectral input statistics.

Together, these findings bolster our understanding of "colour-processing" in this animal's inner retina and suggest that unlike in mammals, teleost fish BCs already encode complex chromatic responses in the inner plexiform layer before driving retinal ganglion cells.

Additionally, the study of colour vision from an organism requires precise control over the light stimuli's temporal, spatial and spectral features. Therefore, chromatic stimulators, designed to be combined with two-photon microscopy, were developed throughout this work. These devices allowed circumventing experimental limitations,

such as spectral crosstalk between the microscope and the stimulus light. Furthermore, they were conceived as open source projects to be easily replicated and adapted to any organism's retina with different spectral sensitivities through the free control over the number and spectra of stimulation light sources. These open source projects originated from the desire to set up a stimulation standard for the field of visual neuroscience.

Acknowledgments

I wish to thank my supervisor Tom Baden, first for giving me the opportunity to work on such insightful and diverse projects, then for his continuous support, guidance, and patience throughout the years. His communicative enthusiasm along with our friendly interactions steered me through these projects.

I am very grateful to all fellow lab members for their regular collaboration: Takeshi Yoshimatsu for his precious technical advice and insights on molecular biology. Andre Maia Chagas for initiating me to good open source practices. Our continued exchanges brought many projects to life and hopefully many more are still to come. Filip Janiak, for his advices on optics and electronics. Natalia Pouchkina-Stancheva, for her continuous support and administrative help which were essential in difficult times. Philipp Bartel, for teaching me programming languages which over the course of this thesis became an indispensable skill. I furthermore thank all members of the CRPC especially Marvin Seifert and George Kafetzis for all the inspiring and casual discussions we had.

Numerous side projects that do not appear on this dissertation were the result of many interactions with colleagues from the University of Sussex who I cannot all named here but to whom I extend my gratitude.

I had the chance over the last years to visit and reside with many collaborative vision labs in Europe and abroad. I am thankful to the fellow neuroscientists who warmly received me and shared their expertise with me. I am particularly grateful to Thomas Euler, my grant scientific coordinator, and his team from the university of Tubingen, from whom I gained valuable experiences.

I also have a thought for my fellow ESRs from the Marie Sklodowska Curie Action group “switchBoard” and especially to Lucia Zanetti whose friendship and fruitful interactions contributed to the completion of this Ph.D.

Finally, I have a thought for Agathe, my beloved partner in life, who endured me during the writing of this manuscript while being confined during the COVID period. I am deeply obliged to her for never ceasing pushing me forward.

Table of contents

Appendix 2 – Material and Instruction manuals for the Open Visual stimulator

List of figures

Chapter 1

Chapter 2

Chapter 3

List of tables

Abbreviations

Ab: Antibody

AC: Amacrine Cell

AL: Antennal Lobes

α: Cone Specific Absorbance

API: Application Programming Interface

b: Blue

BC: Bipolar Cell

BoM: Bill of Materials

ctpb2: C-terminal Binding Protein

DAQ: Data Acquisition system

DLP: Digital Light Processing

DMD: Digital Micromirror Device

dpf: Days-post-fertilisation

ETA: Event Triggered Average

eV: electronVolt

g: Green

GCaMP: GFP-Calmodulin-Myosin Protein

GCL: Ganglion Cell Layer

GECI: Genetically Encoded Calcium Indicator

GFP: Green Fluorescent Protein

GUI: Graphical User Interface

γ: Quantum efficiency

hpf: Hours Post Fertilisation

IDE: Integrated Development Environment

INL: Inner Nuclear Layer

IPL: Inner Plexiform Layer

J: Joule

JST: Japan Solderless Terminal

kB: kilobit

kHz: kilohertz

LCD: Liquid-Cristal Display

LCoS: Liquid-Cristal on Silicon

LCr: LightCrafter

LED: Light Emitting Diode

L-Opsin: Long wavelength-sensitive Opsin

MHz: MegaHertz

MOEMS: MicroOptoElectroMechanical System

MOM: Movable Objective Microscope

MOSFET: Metal Oxide Semiconductor Field Effect Transistor

ms: millisecond

M-Opsin: Medium wavelength-sensitive Opsin

µs: microsecond

nW: nanoWatt

OMR: OptoMotor Response

OKR: OptoKinetic Response

OPL: Outer Plexiform Layer

OS: Outer-Segment

OSA: Outer-Segment Area

OSL: Outer-Segment Length

PC: Principal Component

PCA: Principal Component Analysis

PCB: Printed Circuit Board

PMT: Photomultiplier Tube

PR: Photoreceptor

PSF: Point Spread Function

PTU: 1-Phenyl-2-Thiourea

PWM: Pulse-Width Modulation

r: Red

RF: Receptive Field

RGC: Retinal Ganglion Cell

Rh: Rhodopsin

ROI: Region of Interest

RPE: Retinal Pigmented Epithelium

s: second

SAC: Starbust Amacrine Cells

SD: Standard Deviation

SOD: Specific Optical Density

SPI: Serial Peripheral Interface

SSE: Sum of Squares Due to Errors

SWS1-Opsin: Short wavelength-sensitive 1 Opsin

SWS2-Opsin: Short wavelength-sensitive 2 Opsin

TFT: Thin-Film-Transistor

Tg: Transgenic

uv: Ultraviolet

UV: Ultra-Violet

UV-Opsin: UV-sensitive Opsin SWS

Chapter 1

General Introduction

Danio rerio colour vision

For the rays to speak properly are not coloured. In them there is nothing else than a certain power and disposition to stir up a sensation of this or that Colour […], so Colours in the Object are nothing but a disposition to reflect this or that sort of rays more copiously than the rest; in the rays they are nothing but their dispositions to propagate this or that Motion into the Sensorium, and in the Sensorium they are sensations of those Motions under the forms of Colours.

Sir Isaac Newton, Opticks (1704)

1.1 – Seeing the world in colour

For many animals, vision is the primary sense through which they build a representation of the outside world. Within the animal kingdom, a plethora of diverse eyes' structure and function can be characterised, each being specifically adjusted to its own environment to detect specific light signals from its surrounding (Baden and Osorio 2019; Land and Nilsson 2013). Visual ecology describes the study of these diverse visual systems in relation to their natural environment and the evolutionary processes by which they adapt their functions to meet their organism's needs (Cronin 2008). Recent studies have illustrated such adaptation of visual systems to scene statistics in mice and zebrafish retinas (Baden et al. 2013; Zhou et al. 2020; Yoshimatsu et al. 2020; Szatko et al. 2020; Dehmelt et al. 2019; Bleckert et al. 2014). Many visual features and retinal processing are to be considered, however, throughout this work the focus will be placed on colour vision, and particularly on how the neuronal inner-retinal circuits of a tetrachromatic animal model, the larval zebrafish, process chromatic signals.

Colour vision describes the ability for an organism to differentiate objects based on their reflectance spectra independently of light intensity. This implies that objects discrimination is based on hue or saturation variations in addition to brightness contrast. To achieve colour vision, an organism requires a minimum of two receptor systems able to detect different spectral sensitivities and a neural system to compute the differences detected by these sensors (Walls 1982). This mechanism was first described by Thomas Young in its *Bakerian lecture on the Theory of Light and Colours* (T. Young 1802). In his lecture, Young described the wave aspect of light and stated that *"The Sensation of different Colours depends on the different frequency of Vibrations excited by light in the Retina"*. He hypothesised three distinct *"Sensations"*, each sensitive to one "*principal colour"*: red, green and violet, other colours resulting from mixtures of these three "*primaries"*. He therefore postulated that the eye contains three types of photoreceptors, one for each of these "primaries", leading to the understanding that "secondary colours" emerge from the superposed images detected by these three photoreceptors (Fig. 1.1a). Later James Clerk Maxwell demonstrated in a classic paper entitled *"Experiments on colour as perceived by the eye, with remarks on colour-blindness"*, that any colour can be generated by a mixture of three monochromatic lights (red, green and blue) (Maxwell 1857). Referring to Young's theory, he stated: *"We are capable of feeling three different colour-sensations. Light of different kinds excites these sensations in different proportions, and it is by the different combinations of these*

three primary sensations that all varieties of visible colour are produced" (Maxwell 1860). This tristimulus then set up the basis of colorimetry by differentiating between hue, tint, and shade, which respectively correspond to spectra, saturation and luminance of colours (Fig. 1.1b). Hermann von Helmholtz, then completed Young's theory by suggesting that the human retina is indeed composed of three distinct photoreceptors, each sensitive to a distinct portion of the spectrum (short- medium- and long-wavelength) (Helmholtz 1866) (Fig. 1.1a). Thus, by varying the relative intensities of the three light-signals that each photoreceptor type receives, arbitrary colour perception could be achieved, while black and white would reflect the amount of light perceived (Fig. 1.1c). This led to the Young-Helmholtz trichromacy theory describing how humans perceive colours (Lee 2008).

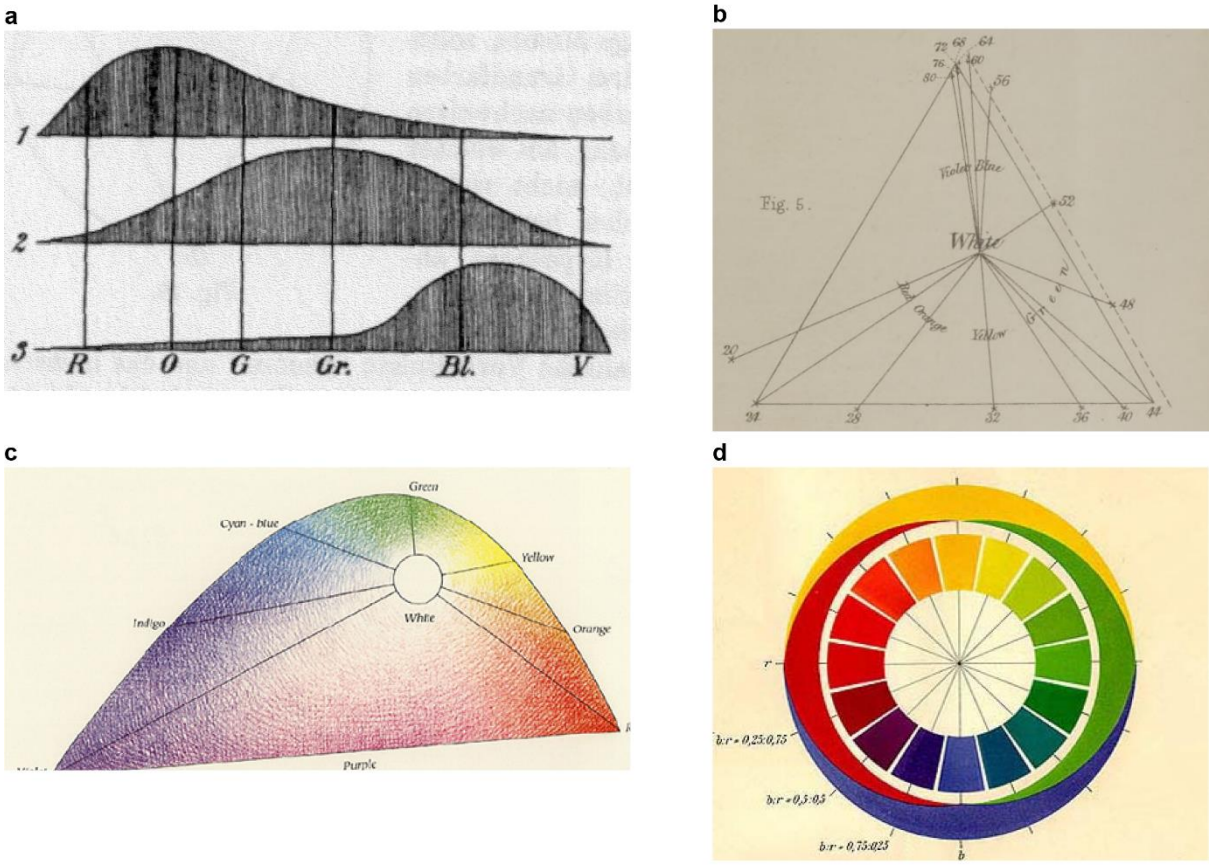

Figure 1.1 | An overview of early colour vision models: a) The Young and Helmholtz trichromatic theory supposed three "*types of fibres*" in the retina with different "*excitement*" along the colour axis. The first curve represents the degree of excitement for fibres sensitive to red, the second for fibres sensitive mainly to green and the third one to blue/violet. **b)** Maxwell's chromatic triangle summarising experiments carried on himself where different combination of tristimulus (RGB) produces a constant white. These experiments set the basis for the determination of the CIE colour space still in use today. **c)** Helmholtz's hypothesized chart of colour mixing based on the relative intensities needed to produce white(Helmholtz 1866). **d)** Hering's circle of chromatic colours describing four fundamental sensations of colour.

The trichromacy theory was then challenged by Ewald Hering with the opponent process theory of colour (*original german text translated by* MacLeod et al. 1967). He stipulated that colours are perceived through mechanisms sensitive to three opponent processes within the human retina (red-green, yellow-blue and white-black (*gegenfarben*)) which cannot be simultaneously perceived. For Hering, there are four primary colours (Red, yellow, green & blue), organised in pairs, each sharing one "*chromatic property*". For example, a pure yellow to which red is added, displays different orange tints until no trace of yellow could be found, only leaving a pure red (Fig. 1.1d). This colour description also explained forbidden colours such as reddish green or yellowish blue.

With the characterisation of retina neuronal circuits, the trichromacy and colour opponent theories were later reconciled: The human retina possesses three types of cone photoreceptor as suggested by Young, Maxwell and Helmholtz. And the characterisation of colour-opponent retinal ganglion cells combining inputs from opponent colour-tuned BCs (Fig. 2.1a) into three colour opponent channels, validating Hering's work (Johnston, Esposti, and Lagnado 2012). Along with colour constancy (that will not be detailed in this work), trichromacy and opponency constitute the fundamental processes for human colour vision.

Organisms with colour vision use this ability to generate unique chromatic identities that can then be employed to direct behavioural response in a colourful environment (Jacobs 1993). Animals' natural environments are usually rich in colour and consequently their chromatic sensitivities have evolved alongside to allow amongst others, efficient foraging for food, the avoidance of predators, navigation or social communication with conspecifics, etc. (Osorio and Vorobyev 2008; Radonjić, Cottaris, and Brainard 2015). This is particularly evident in aquatic environments which present a broad variability of illumination spectra depending on the depth considered and short-wavelength absorption, the nature of dissolved organic matter, etc. (Loew and McFarland, 1990; Losey et al., 1999; Jerlov, 1976). Thus, to fully understand an animal's retinal organisation, the image statistics from the specific natural habitat in which the animal has evolved must be considered (Carleton et al. 2020; Luehrmann et al. 2020). In 1992, John Endler developed his sensory drive hypothesis (Endler 1992b; 1992a) which stipulates that an organism's environmental components influence the evolutionary features of its sensory characteristics in a predictable direction. Thus, by analysing the chromatic statistics from a natural habitat, one could predict the chromatic-related behavioural demands of its inhabitants.

The aim of this Ph.D. is to investigate how zebrafish retinal circuits compute the chromatic light input and compare it to the chromatic distribution of this species' natural habitat. Zebrafish is a powerful model for studying colour vision as it is a tetrachromat with four distinct cone photoreceptors (Fig 1.2a), a wide sensitivity range (~300 – 700 nm) (Fig 1.2b) and the potential to perform diverse and potentially complex chromatic computations. In comparison, the trichromat human retina has a narrower sensitivity range (~400 – 700 nm) and only processes two colour opponent systems (red vs. green and yellow (red + green) vs. blue) (Fig 1.2c).

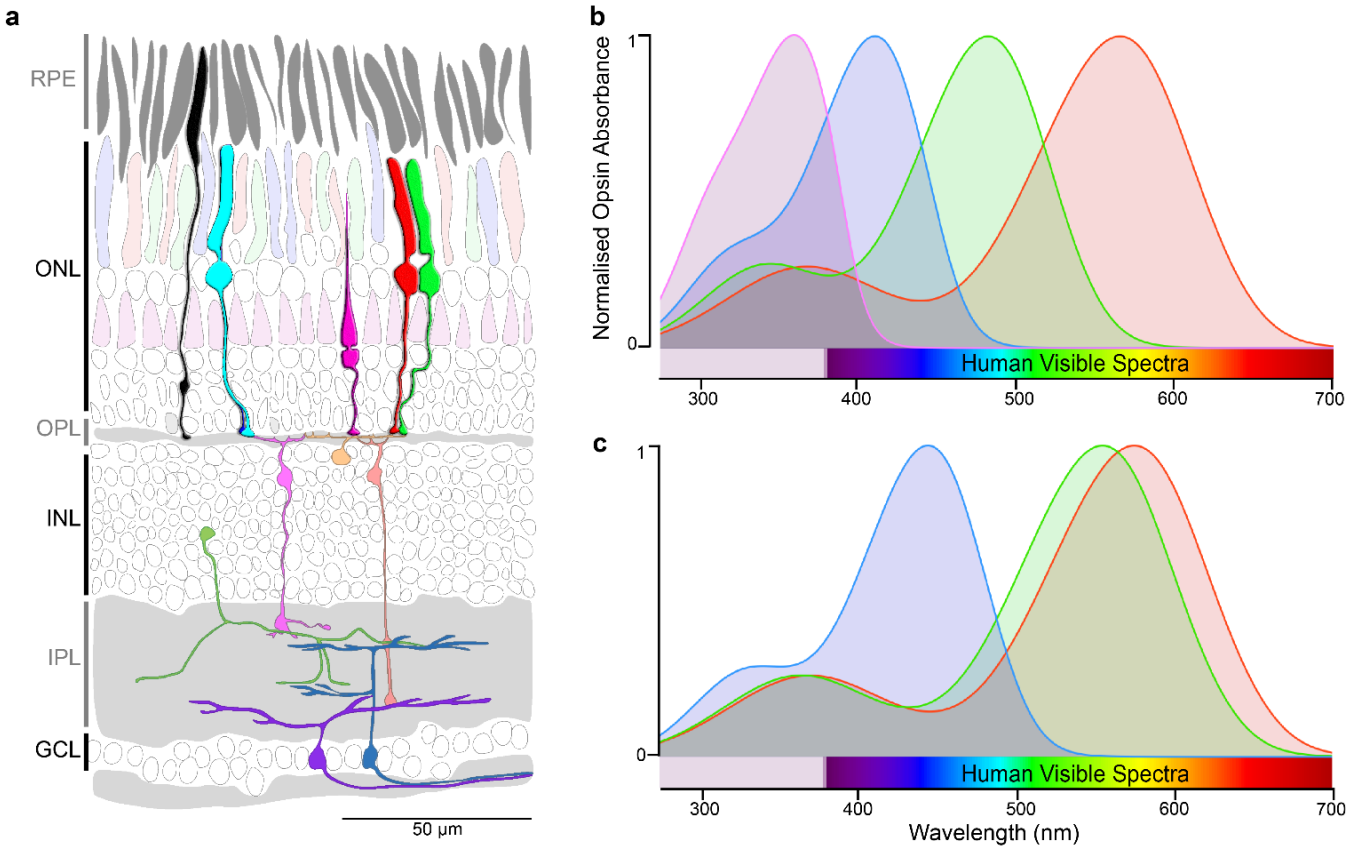

Figure 1.2 | Zebrafish retina organisation: a) Adult zebrafish retinal cells organisation schematics, adapted from (Baden, Euler, and Berens 2020). **b)** Zebrafish cone photoreceptor absorption spectra. **c)** Human cone photoreceptor absorption spectra.

1.2 – Zebrafish retinal organisation

Vertebrate retinal organisation is evolutionary conserved and consists of three discrete neuronal layers transmitting light information from the light-sensitive cells to the projecting neurons; synaptic contacts being limited to two plexiform layers (Fig. 1.2a) (Lamb, Collin, and Pugh 2007; Baden 2020).

Photoreceptors (PR) constitute the first order sensory neurons. They are located at the back of the retinal tissue and their outer segment (OS), embedded in a pigmented epithelium (RPE), contains a visual pigment (opsin) which initiates the visual transduction cascade following light activation. The opsin photoisomerization, from a *cis*- to a *trans*- form, activates the G-protein transducin which in turn decreases the level of cyclic GMP, causing the closure of cGMP-gated cation channels on the photoreceptor membrane which then hyperpolarises (Purves et al. 2004). Unlike other retinal neurons, photoreceptors continuously release glutamate at their synapses in the dark and only modulate its release rate upon light activation (Massey and Redburn 1987). Zebrafish possess five distinct PR types, one rod and four cones, each expressing one of four opsins sensitive to specific parts of the visible spectrum (Davies et al. 2011). They will be categorised in the following work as Red-, Green-, Blue- and UV-sensitive. The zebrafish spectral sensitivities can be described by modelling its photopigment absorption spectra which ranges from ~250 to 700 nm (Fig 1.2b).

PRs synaptic outputs are further modulated by horizontal cells (HC) inhibitory feedback, which maintains the visual system sensitive to luminance variations (Xin and Bloomfield 1999). HCs possess large receptive field and are extensively coupled to each other via gap junctions which allow them to measure the average illumination level that falls onto a relatively wide retinal region. HCs thus subtract a proportionate value from the PR output, maintaining it within an operating range (Masland 2012). Their wide connectivity also generates the centre/surround sensory antagonism (Hartline 1938; Kuffler 1953).

PRs then synapse with BCs in the outer plexiform layer (OPL) (Fig. 1.2a). There are two main types of BCs: OFF BCs which preserve the sign of the cone PRs and are therefore hyperpolarised by light; and ON BCs which reverse the sign of the cones and are depolarised by light. The selective response to light observed in ON and OFF BCs, can be explained by the fact that they express different types of glutamate receptors at the dendrites: OFF BCs express AMPA and kainate ionotropic receptors, thus forming a sign conserving synapse with PRs. Since PRs

depolarise as light level decreases, these BCs increase their activity accordingly and are therefore dubbed OFF BCs (Puller et al. 2013; DeVries and Schwartz 1999). In contrast, ON BCs express metabotropic glutamate receptors which, upon activation, indirectly close cGMP-gated Na^+ channels, reducing inward current thus causing the BCs to hyperpolarise and therefore invert the polarity of their light response. As these BCs consequently depolarise while light level increases, there are dubbed ON BCs (Ghosh et al. 2004). Distinctively, rod BCs (only connected to rod PR) are ON cells as they depolarise in response to light increment, but do not connect directly to retinal ganglion cells (RGC). In mammalian retina, they connect onto AII amacrine cells (AC) which in turn relay the signal to the "cone pathway" by relaying through a sign conserving gap junction synapse onto the synaptic terminal of ON cone BCs, and inverts the signal through an inhibitory glycinergic connection onto the synaptic terminal of an OFF cone BC (Young and Vaney 1991).

BCs are the first retinal neurons with a centre-surround antagonist receptive field organisation; a synaptic circuit required to process spatial information. Let's consider a small spot of light falling onto a single centre PR, connected to a ON BC and flanked by surround PRs "in the dark". When only the centre is illuminated by light the centre PR is hyperpolarised and hence release little glutamate, whereas the surround PRs are depolarised and therefore still release neurotransmitters. The HC is excited by this neurotransmitter release and continues to send high level of inhibitory feedback to all PRs it makes connection with. Such inhibitory feedback causes the centre PR to release even less neurotransmitter leading to a maximally post synaptic excitation of the ON-centre BC. However, if the light expands to the surrounding PRs, all PRs become hyperpolarised, leading to a less excited HC which in turn decreases its inhibition onto the centre PR to finally reduce the ON-centre BC excitation. Reciprocally, when light only reaches the surround PRs, their neurotransmitter release is reduced and since they are more numerous than the centre PR, the HC is minimally excited and its inhibitory signals quite low. The centre PR, already depolarised in the absence of light, is barely inhibited by the HC and therefore release high levels of neurotransmitters, leading to the least excited state of the ON-centre BC. Conversely, the exact opposite is true for a centre PR connected to a OFF-centre BC (Zhang and Wu 2009).

BCs then project their axons in the inner plexiform layer (IPL) where they form synapses with RGC, whose axons bundle together to form the optic nerve. Additionally, ACs modulate the BCs outputs and synapse with both BCs and RGCs by making both GABAergic and glycinergic contacts.

RGCs inherit the ON/OFF centre/surround patterns from the BCs. Their receptive fields are categorised as two concentric circles, a small circular centre, and a broader surrounding ring. They are dubbed ON-centre/OFF-surround when the RGC firing rate is at its maximum when the light spot coincides with the ON-centre; and vice versa for OFF-centre/ON-surround BCs (Barlow 1953; Kuffler 1953). The receptive fields of both type of RGCs are overlapping across the retina so that every region of the visual space is assessed by multiple ON and OFF RGCs in order to enhance object edges sensitivity (Marr and Hildreth 1980).

Studies on zebrafish retinal development (Schmitt and Dowling 1999; 1994) have previously reported an asymmetric distribution of retinal neurons in larvae. At this age the temporal region of the retina displays a high density of cones and very few rods which was thought to be linked to a retinal differentiation of a high visual acuity region similar to the *area centralis* in some vertebrate or to fovea in primates (Zimmerman, Polley, and Fortney 1988). Since this specialised region was temporally located, it was then dubbed *area temporalis* and suggested a high visual acuity in the animal anterior field of view. Similar specialised regions have also been described in other teleost's temporal retinae (Walls, 1942; Ito and Murakami, 1984; Collin and Pettigrew, 1988a).

Peculiarly, the adult zebrafish outer retina does not display any asymmetry in the distribution of cones (Engström 1960; Allison et al. 2010). In contrary, cones are neatly arranged in crystalline arrays, in a regularly alternating fashion: One row of alternating Blue and UV outer-segments (OS) are followed by two rows of Red and Green OS (Fig 1.3a) (Robinson et al. 1993; Li et al. 2012) It will be noted, that zebrafish possesses Blue and UV single cones, the Red and Green ones being fused into double cones and arranged in an alternate pattern (Collin and Shand 2008).

However, in the larval form, cone distribution varies across the retina (Fig 1.3b). In our common publication (Zimmermann et al. 2018), fellow post-doc T. Yoshimatsu immunolabelled individual photoreceptor populations and assessed their distribution densities across the eye. Unlike in adults, which exhibits a neat mosaic pattern, PRs in larvae were anisotropically distributed, with a higher RGB cone density along the horizon (~92% of the overall population) (Fig 1.3c&d).

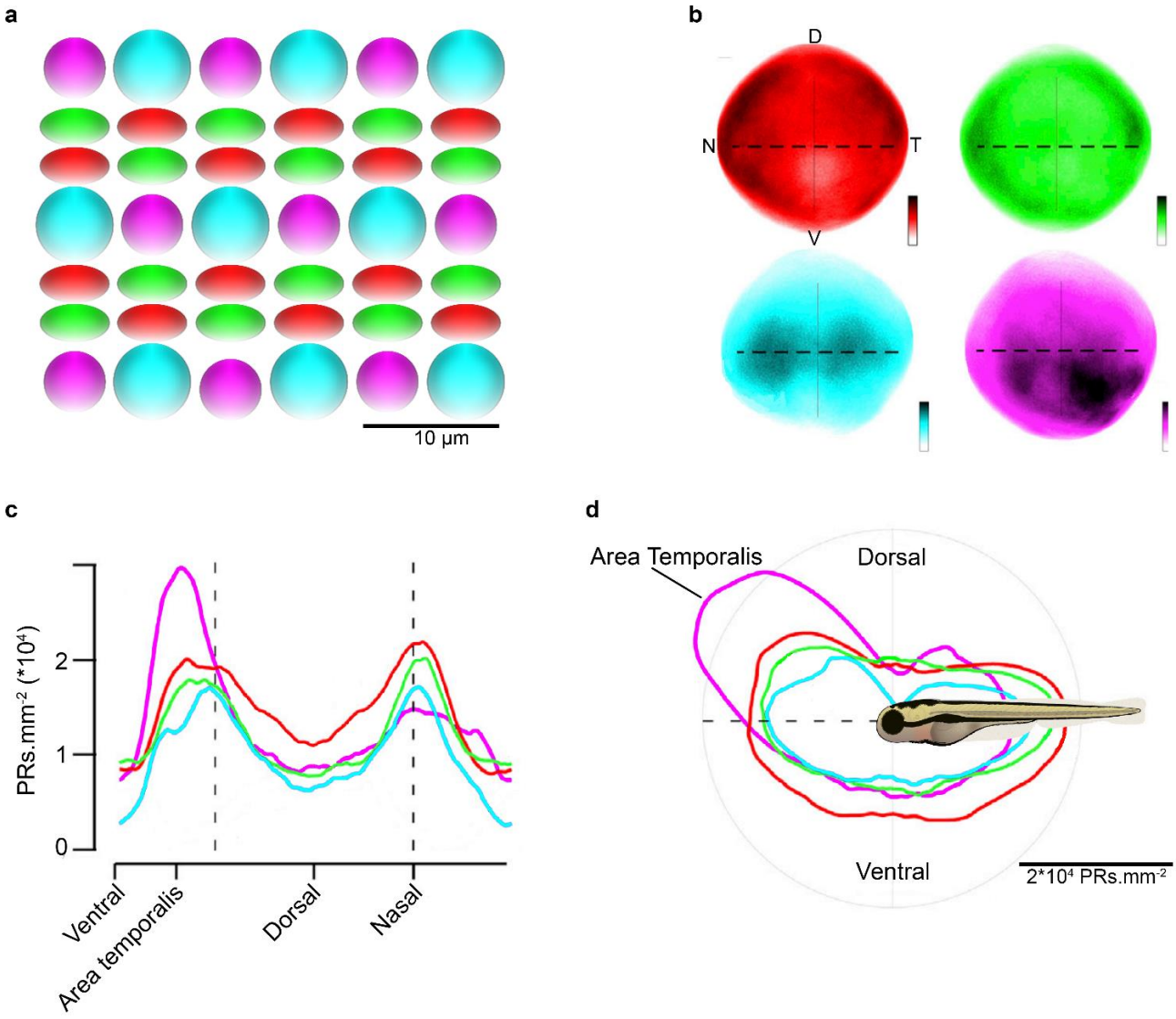

Figure 1.3 | Zebrafish outer retina organisation: a) Adult zebrafish cone photoreceptor mosaic (adapted from (Robinson et al. 1993)). **b)** Average densities of all four cone types across the retina. **c)** Cone distributions across retinal positions on the sagittal plane. N: Nasal, D: Dorsal, T: Temporal, V: Ventral. **d)** Same as **c)** with cone densities plotted in polar coordinates relative to the larval eye as indicated. Dash lines represent the horizon. Panels b-d were adapted from (Zimmermann et al. 2018).

In contrast, the UV ones were packed in the upper-frontal field of view (~30° above the horizon). This UV specialised retinal region coincides with the previously described *area temporalis* which therefore highlights a high retinal acuity for UV signals in this part of the eye (Yoshimatsu et al. 2020).

The larval zebrafish outer retina is then non-uniform and displays a structural and functional anisotropy with a “fovea-like” PRs specialisation for UV signals coming from the upper-anterior field of view (Yoshimatsu et al. 2020). However, these chromatic specialisations appear to be specific to the larval stages as PRs and their

arrangement evolve over the organism development, probably to adapt to the organism's new feeding strategies (Collin and Shand 2008; Bowmaker and Kunz 1987). How are the chromatic light signals received by the regionally-specialised outer retina and then further computed in the inner retina?

One specificity of visual systems compared to other sensory neural systems is the addition of a third layer relaying the information from the primary sensors to the long projecting neurons: The BCs. They are also the only neurons in the visual system making connections to all other retinal neurons. The IPL, where BC terminals project, thus serves as a "switchboard" between the PRs terminals in the OPL and the long-projection RGCs (Euler et al., 2014).

1.3 – The inner plexiform layer organisation

BCs' synapses are the last to mature in the zebrafish retina (~74 *hpf*) (Schmitt and Dowling 1999; Biehlmaier, Neuhauss, and Kohler 2003). In this species, BC axon terminals consist of punctate varicosities that differentially stratify across the IPL depth. The IPL is organised in regular strata, in zebrafish it is traditionally described as two anatomical sublaminae of equal thickness each subdivided into three strata (layers) where BC axonal boutons terminate. BCs convey the light signals by either conserving or reversing the sign of the response to light (Mayer and Dowling 1988). As detailed above, depending on the response to a spot of light presented in the centre of their receptive field, BCs are either categorised as ON or OFF cells (Werblin and Dowling 1969). By convention, BCs stratification pattern is used to define the functional type: BCs with axons terminating within the three top layers of the IPL are categorised as OFF-BCs, while those terminating in the bottom three are categorised as ON-BCs (V. P. Connaughton and Nelson 2000; V P Connaughton 2011). Cajal already noticed two types of BC with distinct projection patterns in avian retinae (Ramón y Cajal 1892). He described rod BCs systematically stratifying at the bottom edge of IPL, close to the RGC layer, while cone BCs stratified at different depth within the IPL. In consistence with these early retinal observations, later electrophysiology work demonstrated that all rod BCs depolarise to light, validating their unique stratification within the ON sublamina (Dowling 2009).

To our current knowledge, 17 cone BC types have been identified based on their overall morphology, their stratification pattern and their dendritic arborisation (Fig 1.4a). The zebrafish retina thus possesses more BC types than most mammalian

retinae (9 in cats, 11 in primates, 13 in mice) (Silke Haverkamp et al. 2005; Helmstaedter et al. 2013; Richard H. Masland 2012b; Kolb, Nelson, and Mariani 1981), but is however similar to other cyprinid fish eyes (Sherry and Yazulla 1993). Seven of these BC types stratify (eight with the account of rod BCs) in single layers, concomitant with mammalian retinal organisation (Euler et al. 2014a; Helmstaedter et al. 2013) which facilitate their functional identification. The remaining BC types are either bi- or tri-stratified within one sublamina or across them, giving rise to potential "mixed" types, which were nonetheless categorised as distinct ON- or OFF- type following light occurrence (V. P. Connaughton and Nelson 2000), although some display both ON and OFF components (Wong, Adolph, and Dowling 2005; Wu, Gao, and Maple 2000; Ammermüller and Kolb 1995).

Furthermore, BC response polarities can vary depending on the light spectra they are stimulated with (Wong, Adolph, and Dowling 2005; Shimbo et al. 2000), suggesting the existence of colour opponent mechanisms at the BC level, and calling for an investigation of BC-type connectivity to PRs, HCs and ACs. Studies assessing zebrafish BC connectivity in the OPL highlight that BCs with similar axonal stratification pattern display a broad variety of PRs connectivity (Li et al. 2012). However, insofar as this has been experimentally explored, a given BC categorically only receives either sign-conserving (OFF) or only sign-inverting (ON) drive from cones across all its contacts. Accordingly, any dendritically derived BC opponency, where present, would presumably be inherited from its presynaptic elements (PRs and HCs) rather than built de-novo at this site.

Next, unlike in mice (Behrens et al. 2016), in zebrafish the axonal stratification patterns by themselves are insufficient to define BC types because BCs with distinct dendritic connectivity patterns can exhibit highly similar axonal stratifications (Fig 1.4b). Similarly, BCs with apparently identical dendritic trees share a common PR connectivity pattern but their axon terminals can stratify at different IPL depths. It will also be noted here that the zebrafish retina only possesses one type of purely monochromatic BCs which solely synapse with green cones. In comparison, dichromat mice possess one pure ON-blue BC (type 9) which post-synaptically generates a blue-ON centre (Breuninger et al. 2011). Mice also possess a green cone-biased OFF BC (type 1) though to supply a green OFF antagonism to this blue-ON signal (Behrens et al. 2016).

To therefore fully understand how the inner retina shapes the chromatic light signal, a renewed look at BC-type specification in zebrafish will also be required. Investigating these neurons' response to various chromatic stimulation and their correlation to established morphological types promises to go partway to achieving this goal.

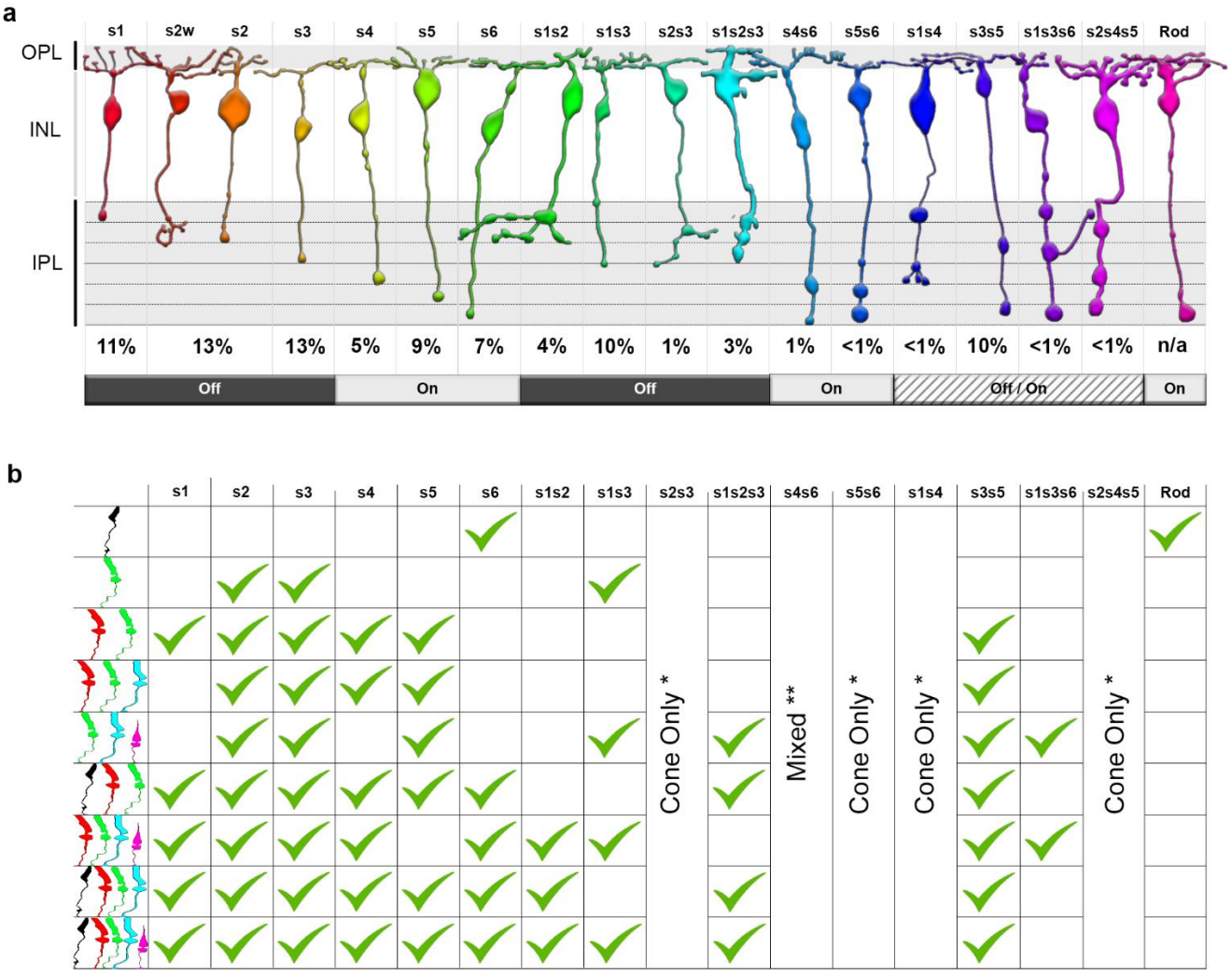

Figure 1.4 | Zebrafish inner retina organisation: a) Representation of known BC types in the zebrafish retina highlighting dendritic field, soma position, stratification patterns. Below is the population estimation of each BC type within the retina and their expected response polarities. **b)** Connectivity table between photoreceptors and BC types. Figures and data derived from (Li et al. 2012; V. P. Connaughton, Graham, and Nelson 2004)

1.4 – Colour vision retinal processing in the outer retina

We previously detailed how PRs transduce light signals and how HCs modulate the overall luminance, adapt their synaptic output to light variations and generate centre/surround antagonisms which set the basis for spatial vision. Similarly, colour vision processing also begins at the very first synapse within the visual pathway: As previously mentioned, cone PRs in zebrafish allow the visual system to be sensitive to wavelength ranging from UV to red. They are interconnected via HCs in the outer retina with which they make specific connections. Depending on the combination of synaptic contacts between HCs and PRs types, diverse spectral responses between the four colour channels will emerge (Baden 2021; Connaughton and Nelson 2010). BC inputs are then modulated by spectrally-coded HCs resulting in spatial colour opponency responses (Fig. 1.5).

Early electrophysiological studies described two types of HC: the luminosity units (L-types) which hyperpolarise in response to light of any wavelength, and chromaticity units (C-types) which hyperpolarise to certain wavelength but depolarise to others (Toyoda, Saito, and Kondo 1978; Svaetichin and MacNichol 1958). L-type HCs display a monophasic feedback effect on cone pedicles while C-types exhibit multiphasic spectral response properties reflecting synaptic inputs from all cone types. These electrophysiology recordings were then the first evidence to support Hering's opponency theory where chromatic information is transmitted to higher cerebral via three colour opponent channel (c.f. 1.1) (Hurvich and Jameson 1960). Such early colour opponency processing also leads to the definition of the colour axes described by Hering.

Zebrafish retina, like most non-mammalian species, possess three types of cone-HC (H1, H2 & H3) and one rod-HC (H4) (Klaassen et al. 2016; V. P. Connaughton, Graham, and Nelson 2004). H1 contacts all four cone types, H2 synapses with green blue and UV cones, and H3 mostly connects with UV cones with minor contributions from the blue ones. H1 HCs, the most numerous in the zebrafish retina display L-type responses, hyperpolarising to all wavelengths (Fig. 1.5a). H2 HCs are biphasic; and while they do not directly synapse with red cones, they depolarise to red light stimulation while hyperpolarising to green, blue and UV (Fig. 1.5b). Finally, H3 HCs display triphasic and tetraphasic response to spectral stimuli, contributing to more complex opponency mechanism (Fig. 1.5c&d) (Connaughton and Nelson 2010; Li, Matsui, and Dowling 2009).

The number and spectral properties of C-types HC vary extensively between species. In comparison, mammalian retinae possess two C-types HCs, one generating a yellow (red + green) surround in blue cones and one setting the red / green opponency (Crook et al. 2011; Lee, Martin, and Grünert 2010). Most dichromat only possess one class of C-type HC with biphasic response profiles (Twig, Levy, and Perlman 2003; Stone, Witkovsky, and Schutte 1990). And up to six different chromatic C-type HC can be found in the sturgeon fish (Govardovskii et al. 1991). However, the role of HC feedback and feedforward mechanisms in its contribution to colour vision remains unclear.

Overall, the cone connectivity patterns with HCs and BCs along with HC tuning properties modify the spectral signals in the outer retina, generating spatio-chromatic centre/surround components which BCs will relay to the IPL and where they will be further modulated by ACs feedback while being passed on to RGCs.

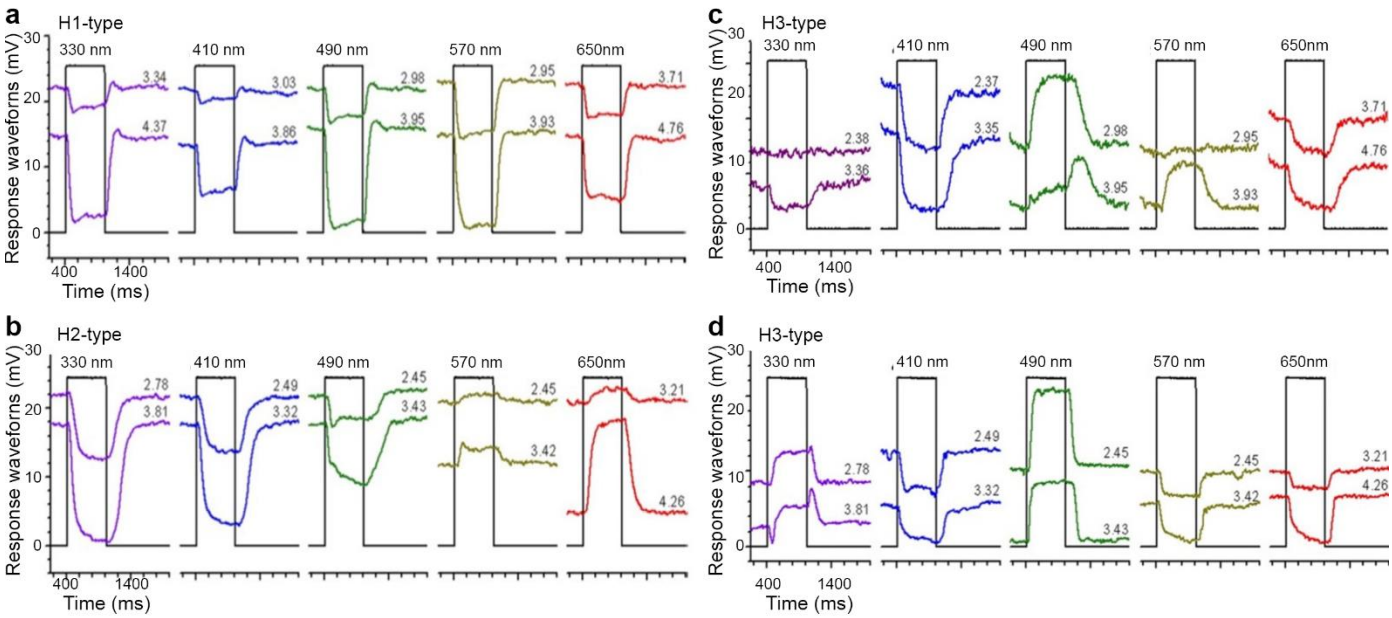

Figure 1.5 | Zebrafish horizontal cell spectral tuning: Examples of HC responses to different wavelength stimuli **a)** H1-HC hyperpolarise to all wavelengths. **b)** H2-HC showing biphasic spectral responses. **c,d)** H3-HC displaying tri- and tetra-phasic chromatic profiles respectively. *Figures adapted from (Victoria P. Connaughton and Nelson 2010)*

1.5 – Zebrafish as a model organism

Zebrafish (*Danio rerio)* is a common animal model for studying neural development and allowed for a broad variety of mutant and transgenic lines to study visual

system functions (Renninger et al. 2011). The larval form of this model is particularly interesting as its small size and its body transparency make it an ideal candidate to be placed under a microscope for *in vivo* functional imaging (Antinucci and Hindges 2016). Furthermore, retinal pigmentation can be prevented genetically (Kelsh et al. 1996; Kameyama et al. 1989), and/or by addition of 1-phenyl-2-thiourea (PTU) which blocks melanogenesis (J Karlsson, von Hofsten, and Olsson 2001), improving the fluorescence signal detection that would otherwise be distorted.

Zebrafish is also a model of choice for the generation of transgenic lines. Any genetic construct comprising fluorescent probes under the regulation of a promoter of interest can be directly inserted in the fish egg at the first cell stage. Thus, the constant development of new genetically encoded biosensors coupled with the high fecundity rate of the zebrafish permits the continuous exploration of its visual system activity.

The zebrafish visual system develops rapidly: The optic stalk is formed within the first 24 hours (Schmitt and Dowling 1994). Photoreceptors become active when their synapses reach maturity at 60 hours post fertilisation (*hpf)* (Schmitt and Dowling 1999; Biehlmaier, Neuhauss, and Kohler 2003). The eye is fully developed by the time of hatching at 4 days post fertilisation (*dpf*) and the larva exhibits basic visual functions such as an optokinetic response (OKR) (Easter and Nicola 1996; 1997; Portugues and Engert 2009). However, the visual system only becomes fully functional by 5 *dpf* with optomotor responses (OMR) (Portugues and Engert 2009). At this stage, the yolk deposit on which the larva was so far feeding is depleted, forcing the animal to find its own food source (Kimmel et al. 1995). From then on, the larval zebrafish mostly rely on vision to navigate their close environment to detect and capture microorganisms. OMRs are reliably evoked by 7 *dpf*, and successful prey capture rates increases during the development to become optimum by 9 *dpf* (Avitan et al. 2020).

Previous studies have reported the larval zebrafish prey capture behaviours to be evoked by small moving spots of light or dark contrast (Bianco, Kampff, and Engert 2011; Trivedi and Bollmann 2013; Semmelhack et al. 2014). It further appeared that prey detection in this animal model was enhanced if elicited by UV cues (Nava, An, and Hamil 2011; Thomas W. Cronin and Bok 2016; Yoshimatsu et al. 2020). Larval zebrafish feed on zooplankton, often-translucent surface-dweller micro-organisms which scatter light underwater in the UV band, hence appearing as UV-bright spot

for UV-sensitive zooplanktivores (Flamarique 2013; Novales Flamarique 2016; Browman, Novales-Flamarique, and Hawryshyn 1994; E. R. Loew et al. 1993; Jordan et al. 2004; Yoshimatsu et al. 2020).

The larval zebrafish retina is then ideal for studying chromatic visual processing and throughout this work, a particular emphasis will be put on UV-light signals processing which appears to be linked to prey capture behaviours.

1.6 – Retinal chromatic stimulation

Investigating retinal neuron's chromatic sensitivities requires an accurate and flexible control over the stimulation light's spectral, temporal, and spatial composition. For studying a tetrachromatic visual system, a stimulator with at least four distinct and narrow spectra is necessary to differentially activate cone PRs. Narrow light bandwidth cannot independently stimulate an individual cone due to cross activation between all cones (Fig. 1.2b). The objective is rather to meet the cone peak absorbance spectra for maximally activate the cone of interest resulting in four LED/cone colour channels. Next, any stimulus-independent temporal flicker in the stimulus light must be well above the animal's flicker-fusion frequency, and the spatial resolution must be beyond its peak visual acuity as defined by receptor spacings. Since the desired stimulation spectrum ranges from ~ 300 to 700 nm (Fig 1.2b), the optical system must be suited for UV light and correct any potential chromatic aberration.

Currently, no commercially available stimulator solution both readily meets these criteria and be easily coupled to an existing 2p-microscope setup. Accordingly, there is a need to develop custom stimulation devices addressing the requirements of a particular experimentation paradigm for a specific animal model. Thus, an important part of the presented work relates to the development of chromatic stimulation equipment. By combining optical systems with 3D-printing and off-the-shelf electronics, efficient and flexible visual stimulation devices were conceived. Here, recent developments in high-performance micro-controllers allowed the generation of complex stimuli while driving LED light sources with sub-millisecond temporal precision, suited for the coupling with two-photon microscopy. The continuous development of these devices overcame key experimental limitations encountered during the investigation of retinal chromatic processing.

Beyond zebrafish, flexible and accurate spectral stimulation is a general experimental requirement for vision studies (Euler, Franke, and Baden 2019). In an reffort to engage with the open source philosophy (Bonvoisin et al. 2017; Pearce 2012), all hardware created here were therefore made versatile and shared as open source hardware projects on open access platforms along with extensive documentation (Maia Chagas 2018) to render each design adaptable to any recording system. Additionally, as spectral sensitivities vary between studied organism models, each system was designed to be flexible for integrating arbitrary light sources spectra.

Since most commonly used stimulation devices employed in the retinal studies or in visual psychophysics were originally designed for primate trichromatic vision, they typically only integrate three spectral channels (red, green blue) and usually fail to drive short wavelength (UV) light. The developed open hardware visual devices aim to set a standard for chromatic stimulation experiments with the objective to increase replicability and improve data transfer between animal models. All hardware projects are under open source licenses (Morin, Urban, and Sliz 2012) so they can be easily replicated, adapted to different recording systems, and further upgraded within the field of visual neuroscience.

1.7 – Thesis expectations:

In the presented work, we will cover the work performed to understand how the chromatic signal, detected by PRs and modulated by spectrally tuned HCs, is processed and transmitted by BCs within the IPL. Our aim was to describe how the tetrachromatic zebrafish larva perceives the outside world by understanding how it breaks chromatic visual inputs into relevant parallel channels. In this work we will focus on the second synapse of the visual system, but we will also acknowledge the work carried on by fellow lab members working on other retinal structures as well as ecological field studies relating the chromatic visual content of larval zebrafish natural environment. Altogether, these parallel studies will hopefully bring a better comprehension to this species colour vision strategies.

Similarly to work carried on mice (Franke et al. 2016; Baden et al. 2016; Szatko et al. 2020; Baden et al. 2013), we aim in this work to characterise functional BC types and to describe their location within the eye. In comparison mice PRs are symmetrically distributed, with green sensitive cones located in the dorsal retina and UV sensitive ones located in the ventral region. Such distribution complies with

the ecological need for mice to detect flying predator in the upper part of his visual field of view. Consequently, the underlying retinal circuits in this part of the eye is tuned to detect dark contrast against a short wavelength luminous background. We thus expected to observe similar chromatic retinal specialisation in our model retina which has evolved in a more “complex” chromatic environment as shallow waters where this species dwell alters the natural light entering the waters, and objects will have their chromaticity alter along with their distance from the observer (Bartel et al. 2021).

Also, as investigations of retinal circuits underlying colour vision in non-primate models are not fully developed. We had to dedicate an important part of our work to the development of custom-designed chromatic stimulators that could be coupled with our two-photon recording system. The development of such devices will not only help to further investigate chromatic processing within the IPL, but also any other neuronal structure of the fish visual system, from PRs to tectum. All devices were developed as flexible open source hardware project with extensive and accessible documentation in order to be easily reproduce by fellow scientists working on similar topics but in animal models requiring dedicated spectral stimulation. In the end, every eye is different.

Chapter 2

A structurally and functionally anisotropic retina

How does the asymmetric IPL organisation reflect how bipolar cells process chromatic information across visual space to match natural scenes?

[I]f any variation or modification in the organ be ever useful to an animal under changing conditions of life, then the difficulty of believing that a perfect and complex eye could be formed by natural selection, though insuperable by our imagination, can hardly be considered real.

Charles Darwin, On the Origin of Species (1859)

In the following chapter I will present the work conducted to unveil BC working mechanisms in response to tetrachromatic stimulation. This work was used for the publication of ***Zebrafish Differentially Process Colour across Visual Space to Match Natural Scenes.*** *Zimmermann MJY, Nevala NE, Yoshimatsu T, Osorio D, Nilsson D-E, Berens P and Baden T.*

2.1 – Introduction

Conventionally, BC terminals within the IPL are categorised into two main structural categories that corresponds to their distribution across the IPL and their correlated functions (Euler et al. 2014a). As discussed in the previous chapter, these categories are associated with the IPL's anatomical division into two sublaminae: BC axonal boutons stratifying in the upper ("inner", INL-adjacent) sublamina tend to display OFF features, while those stratifying in the bottom ("outer", GCL-adjacent) one tend to display ON features. The aim of this chapter is to understand how chromatic signals are processed within the IPL, how chromatically-responding BC terminals stratify within the ON / OFF sublaminae and if chromatic information is encoded in a BC-type specific manner.

BCs, like PRs, possess ribbon synapses, large lamellar structures responsible for the high release rates of neurotransmitter observed from these synapses (Heidelberger, Thoreson, and Witkovsky 2005; Schmitz 2009; Richard H. Masland 2012b). Continuous release of neurotransmitter is necessary to relay the visual information in response to continuous fluctuations in light intensity (Lagnado and Schmitz 2015). The ribbon synaptic structure allows both tonic and transient release of neurotransmitter through continuous docking and exocytosis of synaptic vesicles. The purification of synaptic ribbons from retina samples lead to the characterisation of a unique component homologous to the transcription co-repressor CtPB2 protein, dubbed here as Ribeye (Schmitz, Königstorfer, and Südhof 2000). Transgenic zebrafish lines have been generated to express genetically encoded calcium indicators (GECI) under the control of the Ribeye promoter (Dreosti et al. 2009), enabling selective expression of GECI in PRs and BCs. In the following work, transgenic zebrafish larvae were used, expressing GCaMP6f fused to the synaptic protein synaptophysin under the ctpb2 (RibeyeA) promoter: *Tg(-1.8ctbp2 : SyGCaMP6f)*. This results in the expression of calcium indicators in all BC synaptic terminals for these larval eyes (Fig 2.1a), from which stimulus-evoked calcium transients can then be optically interrogated.

Transgenic larvae were then imaged under a custom-built MOM-type (Movable objective Microscope) two-photon microscope (Euler et al. 2009) and their retinae were stimulated with a custom-built tetrachromatic stimulator (cf. Chapter 3). The stimulator consisted of four filtered LEDs chosen to match the zebrafish's four cone-opsin absorption peaks (Fig 3.2a), thus generating four spectral channels.

2.2 – Encoding of chromatic information in the inner retina

To assess the BCs' temporo-spectral sensitivity, a tetrachromatic binary noise stimulus was presented (Korenberg and Naka 1988). Specifically, each of four LEDs ran a random binary white noise sequence at 12.8Hz. A white noise stimulus displays a flat spectrum to a sensory system in an uncorrelated sequence with zero mean and a gaussian distribution. Such sequence is designed to avoid adaptation to strong or prolonged stimuli (Chichilnisky 2001). A frequency of 12.8Hz was arbitrary chosen as the BCs in the larval zebrafish retina respond well within this range, and this value does not generate alias against the scanning rate. Using the calcium-event triggered average (i.e. similar to reverse correlation), kernels can be extracted for each spectral channel which can be loosely considered effective opsin-derived inputs. The analysis aims to characterise the linear response properties of sensory neurons (Sakai 1992). The resulting kernels summarise the preferred temporo-spectral input that each stimulated BC terminal maximally responds to.

This tetrachromatic white noise was presented for a duration of 258 s to zebrafish retinae aged 5-8 *dpf* expressing RibeyeA::SyGCaMP6f. Fish were immobilised in agar and positioned on the side, allowing two-photon scanning of the retina's sagittal plane. Scans consisted of 64*32 pixel image sequences (pixel size = 0.56 µm) captured at 15.625 frames per second (32 lines at 2 ms line duration). Scans were acquired using ScanM (developed by W. Denk, M. Müller and T. Euler), an IGOR-pro custom-written software (Fig 2.1a top). Regions of interest (ROIs), corresponding to BC axon terminals, were defined semi-automatically using CellLab, a custom software designed by D. Velychko, CIN (Fig 2.1a bottom (Baden et al. 2016)). Calcium traces were extracted and detrended using a high pass filter >0.1Hz and z-normalised (Fig 2.1b). Fluorescence traces were matched to the stimulus sequence, and through reverse correlation (Chichilnisky 2001), four temporo-chromatic kernels were then extracted for each BC terminal, one for each LED input. The time of the triggered calcium-transient is represented here by a vertical line (i.e. t = 0 s) (Fig 2.1c). BC terminals revealed various chromatic sensitivity profiles that can be categorised into three distinct groups:

1- Achromatic, when kernels displayed both consistent polarities and similar sensitivities to all LEDs. Such profiles indicated an approximately wavelength-independent response to light stimulation (Fig 2.1c (1)).

2 - Chromatic, when the extracted kernels had consistent polarities but presented different sensitivity preferences towards one or multiple LED channels. These profiles highlighted wavelength preferential responses (Fig 2.1c (2)).

3 - Colour opponent, when terminals showed opposite polarities across LED channels. Colour opponent profiles denoted antagonistic processing of different wavelengths of light in those BC terminals (Fig 2.1c (3)).

BC spectral profiles were then mapped back onto the scan images to assess their distribution within the IPL. Consistent with other vertebrate retinae, BC OFF-responses tended to occur in the upper half of the IPL, while ON-responses mainly occurred in its lower half for all spectral channels (Richard H. Masland 2012c). However, in larval zebrafish the transition depth between OFF and ON layers differed between spectral channels and moreover varied with the BC's position within the eye. In the example scan taken from the nasal part of the retina (Fig 2.1d), Red ON-responses transitioned higher in the IPL (closer to the Outer Plexiform Layer, OPL) compared to the other three spectral channels. This "higher transition" thus generated a colour opponent layer in this part of the eye, where BCs tended to differentially process long-wavelength signals originating from the temporal side of the fish visual space. Additionally, a long- versus short-wavelength layer can be noted at the bottom of the IPL, just below a layer of BC synapses that displayed various chromatic profiles not detailed here.

In the nasal region of the eye, BC terminals with similar response characteristics appear to segregate into seven distinct layers within the IPL (Fig 2.1d), revealing a structural organisation where BC axonal stratification patterns within the IPL sublaminae were correlated to their functional profiles (V P Connaughton 2011; Nevin, Taylor, and Baier 2008; Li et al. 2012). However, this functional layering was not consistent across the eye. On the second example scan taken from the temporo-ventral part of the retina (Fig 2.1e), the functional layering organisation was predominantly taken over by Blue and UV ON-responses which stretched nearly across the entire IPL depth. Now, responses to Red and Green stimulations seemed to have all but disappeared. Still, a functional organisation can be observed with fewer functionally distinct layers (Fig 2.1e). Moreover, this second example region did not appear to be strongly tuned for opponency but rather for the detection of short-wavelength signals.

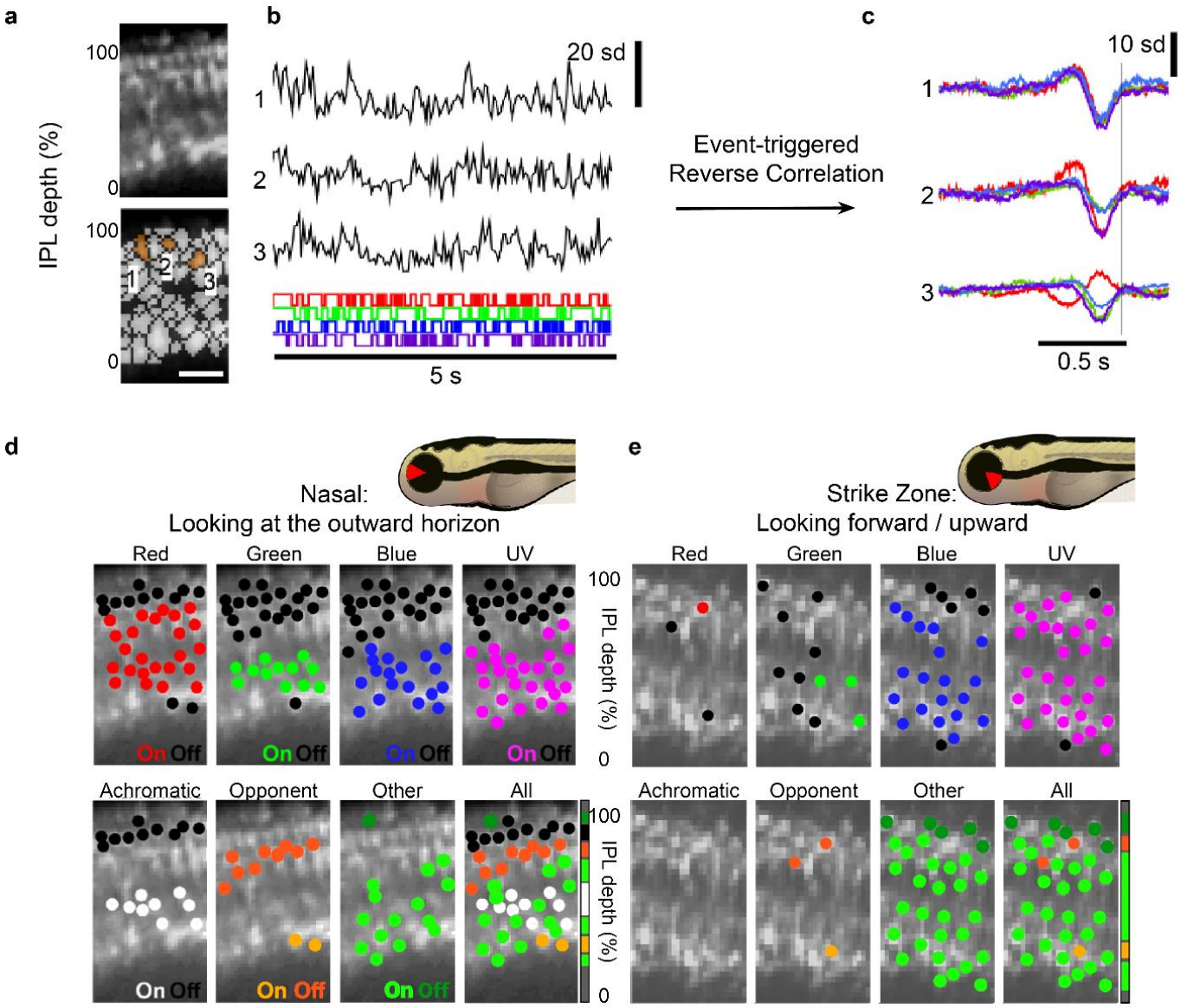

Figure 2.1 | Tetrachromatic response to white noise in the IPL: a) Two-Photon scan field of a *Tg(RibeyeA:SyGCaMP6f)* larval fish IPL (top), with semi-automated selected ROIs (bottom). **b)** Calcium traces extracted from ROIs (top), in response to tetrachromatic white noise stimulus (bottom). **c)** Tetrachromatic kernels recovered through reverse correlation exhibiting 1) Achromatic, 2) Chromatic, 3) Colour Opponent profiles. **d), e)** ROIs chromatic ON- OFF-kernel profiles mapped back on their recording scans in the nasal and the temporo-ventral (*strike zone*) retinal region. The bars on the right are visual estimations of the BC terminals functional stratification highlighting the disparity in the IPL layering organisation across the retina.

These two examples suggested that the larval zebrafish IPL was functionally anisotropic: Different parts of the eye appeared to be functionally organised in a different manner. A more complete examination of the fish inner retina was therefore necessary, with the goal to assess how the BC temporo-spectral profiles were distributed across the eye, how their functionality transitioned from one region to another, and which specific chromatic or colour opponency computation predominated in these regions. In our two-photon microscope, the laser excitation and the light stimulation both come through the objective; the larval fish required then to be mounted on its side for the stimulation light to pass through the lens and reach the retina, enabling sagittal-plane recordings.

Recordings were performed on a standard diffraction-limited two-photon microscope, designed to obtain the highest image resolution (Helmchen and Denk 2005; Denk and Svoboda 1997). This configuration reduces the point spread function (PSF) on our setup to 0.5 µm on x and y axis, and 3.5 µm on z. Hence, we need to consider that the PSF on the z axis may generate a mixture of fluorescence signals from two adjacent overlapping BC terminals which are within that distance. However, the expression profile of the calcium indicator at higher resolution imaging recorded at different depth (above and below the targeted BC terminals), did not display any fluorescence profile on other structures, which may have generated signal overlaps. We then assume that imaging on defined ROIs did not generate additional overlapping signal. Moreover, only ROIs where at least one of the four spectral kernels peak-to-peak amplitudes exceeded a minimum of two standard deviations were kept for further analysis. A total of 113 scans were taken along the eye's sagittal plane, from which n=6,568 ROIs were selected. 4,099 (62%) passed the above-mentioned quality criterion (cf. Methods 6.3) revealing a large diversity for BC chromatic profiles along the inner retina (Fig 2.2a). The relative fraction of kernels passing the arbitrary chosen selection criteria value, was analogous all along the eye and therefore did not have a major effect on the results (Fig 2.2 b).

The complete functional tetrachromatic mapping confirmed that the IPL was highly anisotropic (Fig 2.2c). BC OFF- and ON-responses were mapped for each spectral channel across the IPL depth (vertical axis) and along the eye position (divided into 12 bins on the horizontal axis). The vertical dashed lines representing the horizons and the horizontal ones indicating the traditional anatomical separation between the two IPL sublaminae, as demarked by the upper starburst amacrine cell layer.

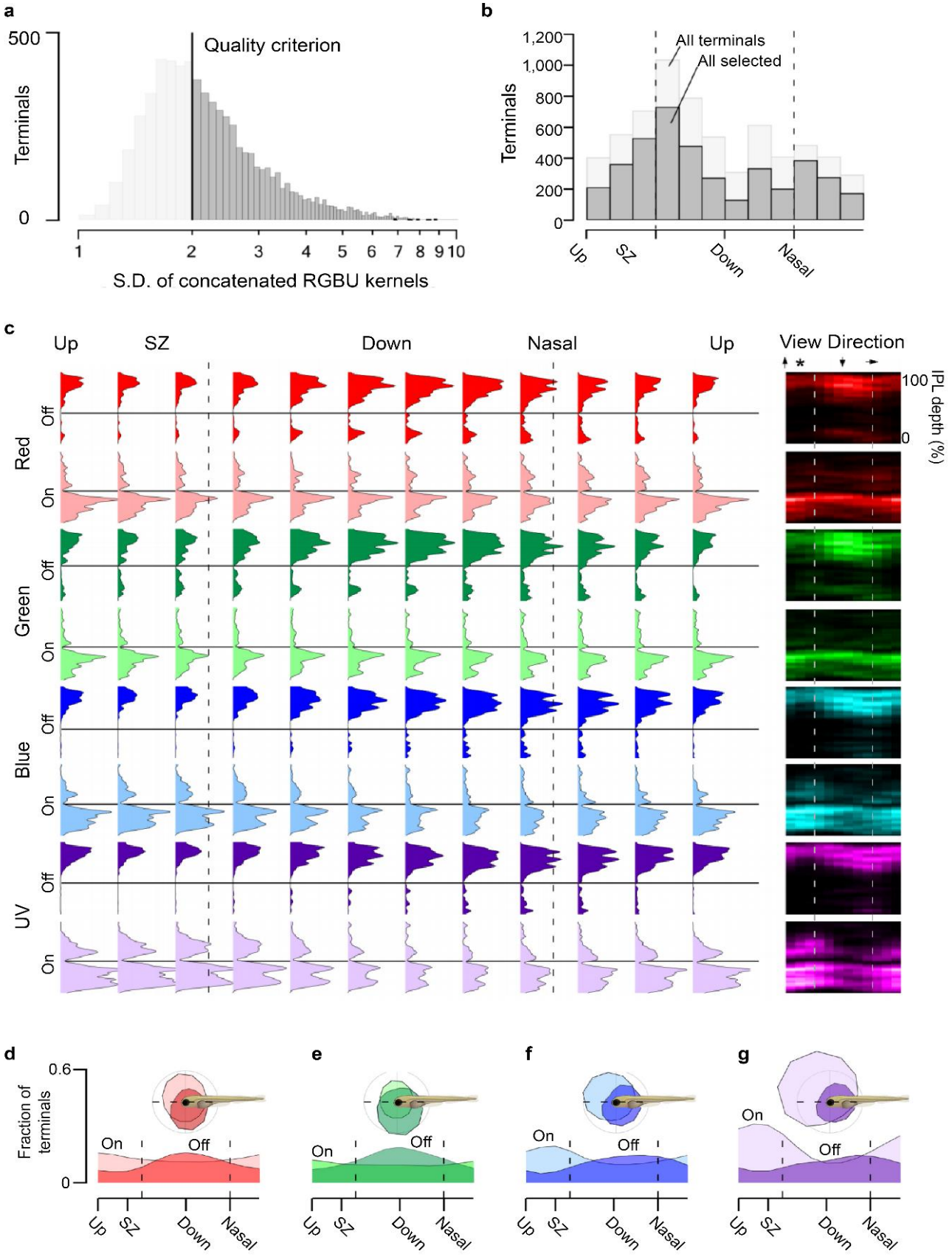

Figure 2.2 | Functional tetrachromatic bipolar cell mapping: a) Histogram of quality criterion for all recorded terminals with cut-off value of 2 SD. **b)** Distribution of all (light grey) and selected (dark grey) BC terminals across the eye positions. **c)** Distribution of R, G, B and UV responses along the IPL

depth and eye position. Insets on the right displays the data as heatmaps. **d,e,f,g)** Distribution of all ON and OFF responses for each colour channel. *Figures generated by T. Baden for the publication (Zimmermann et al. 2018).*

This map revealed the functional distribution of BC terminals into continuous but positionally shifting layers along the IPL. It appeared that each spectral channel followed its own stratification pattern with anatomical preferences. For example, ON-Red responses were represented in the top layer of the bottom sublamina without much fluctuation across the retina. In contrast, other layers showed a neat predominance for the dorsal region surveying the lower visual field (Fig 2.2c heatmap inset). All spectral channels except for UV displayed a preference for the lower visual field. This can be linked to the chromatic composition of the fish's natural habitat where short-wavelength signals were relatively less abundant below the horizon (Zimmermann et al. 2018). Interestingly, for Red, Green, and Blue channels, ON-responses were systematically biased towards the upper visual field while OFF-responses predominantly surveyed the lower visual field (Fig 2.2 d,e&f).

Next, Blue ON-responses (Fig 2.2f) followed the UV bias towards the upper frontal visual field (Fig 2.2g), which could be linked to the cross activation of UV-cones by the blue LED, which despite being set and filtered towards the SWS2 opsin (expressed in Blue cone) peak absorbance spectra, was also overlapping with a portion on the SWS opsin (UV cone) absorbance spectra (Fig 3.2a). In support, the UV channel displayed a stronger bias towards this region compared to the Blue one. Also, the lack of Blue and UV responses on the dorsal regions makes intuitive sense, as UV signals underwater rapidly decay with depth, and poorly reflect off the riverbed. Furthermore, zebrafish larvae prey on translucent zooplanktons, microorganisms that absorb and/or scatter UV light, a characteristic which enhances their contrast to a UV-sensitive predator (Novales Flamarique 2016; Yoshimatsu et al. 2020). The presence of a specialised retinal region for short-wavelength light confirmed the need for the zebrafish larvae to detect UV bright objects in their upper frontal field of view. It can then be hypothesised that the blue and UV responses observed in the temporo-ventral region of the retina are both part of a dedicated UV colour channel.

This UV-specific region of the retina will from now on be designated as the "*strike zone*" as it appears that this functional anisotropy was directly correlated to the described "striking" prey capture behaviour (Kalueff et al. 2013), where the fish after having located its UV-bright prey in its frontal-upper visual space, rapidly orients

towards it and captures it. In the previous chapter, we reported a temporal retinal specialisation observed in the young zebrafish. This *area temporalis* exhibits a high cone density (Schmitt and Dowling 1999), suggesting an improved visual acuity similar to the *area centralis* observed in other vertebrates (Zimmerman, Polley, and Fortney 1988). The *strike zone* therefore might be the location of a potential high visual acuity for short-wavelength objects presented in front of the fish (Yoshimatsu et al. 2020).

In summary, the IPL is functionally highly anisotropic with a compartmentalisation of RGB profiles orientated towards the lower part of the visual world, and a UV predominance for the upper part, especially within the *strike zone* for the upper-frontal visual space. Additionally, the functional anisotropy was also linked to differential BC stratification in different parts of the eye, including a clear differential representation of ON- and OFF- bands. This is particularly striking for UV-ON responses in the ventral part of the retina where they cover approximately 70-80% of the IPL (Fig 2.2c UV-insets).

2.3 – The inner retina anatomy reflects the functional chromatic organisation

With the *area temporalis* / *strike zone*, it was previously demonstrated that BC position within the larval zebrafish retina can be correlated to specific chromatic functions. Further structural organisations in this model retina could therefore highlight supplemental functional anisotropies observed on the BC tetrachromatic response mapping.

To anatomically interrogate the organisation of BC synaptic terminals across the eye and IPL, intact eyes of the same transgenic line (RibeyeA::SyGCaMP6f) were immunolabelled at 8 *dpf* against GFP (primary Ab binds on GCaMP expressed in all BC terminals), displayed here in green (Fig 2.3a). To assign terminal positions within the retinal structures, samples were incubated with Hoechst 33342 (a fluorescent DNA stain solution) here in grey to highlight nuclear layers. Additionally, anti-PKCα antibodies (magenta) were used to identify rod-input receiving (Greferath, Grünert, and Wässle 1990) and ON-BCs(sometimes called “mixed BCs”) (Haug et al. 2019). Anti-ChAT antibodies (cyan) was then added to label starburst amacrine cells (SAC) (S. Haverkamp et al. 2009) whose dendrites are organised in two layers, dubbed the ChAT bands. The lower CHaT band (towards the RGC) demarks the anatomical separation between the traditional ON and OFF

IPL sublaminae (Sánchez-González et al. 2009). These bands are commonly used to assigned BC-RGC synapse positions in various species (Moritoh et al. 2013).

The anatomical labelling again confirmed that the IPL was not uniform across the eye (Fig 2.3a). Most notably, its thickness varied approximately two-fold with retinal position, with the thickest part in the nasal and temporal areas which survey the horizon (Fig 2.3b&c). In counterpart, regions surveying the upper and lower visual field comprised a much narrower IPL (Fig. 2.3d). Moreover, the *strike zone*, as previously reported (Schmitt and Dowling 1999), displayed a marked IPL enlargement. A clear structural anisotropy on the eye's sagittal plane can then be reported and grouped into four distinct groups: The horizon regions (nasal and temporal), the dorsal region (looking down) and the ventral regions (looking up) with a particularly thin IPL, and immediately adjacent the much thicker *strike zone*.

A closer look at IPL local organisation highlighted more regional specific features: For example, terminals of "mixed" BCs (which in adults integrate cone and rod inputs), are generally thought to be easily identified due to their large expanded soma confined at the very bottom of the IPL (Stell 1967; Li et al. 2012) and their high specificity for PKCα (Haverkamp and Wässle 2000). However, terminals matching this description could only be found in the ventral and dorsal retina, but not around the horizon. Interestingly, this particular anisotropy reflected the rod distribution, which also only exist in these parts of the eye at 8 *dpf* (Zimmermann et al. 2018).

In the literature, the larval zebrafish IPL is commonly depicted to possess six equal sublaminae (Connaughton 2011). Nonetheless, from both the functional data and the immunostainings it can be observed that only the horizon regions possessed six distinct layers with round-shaped terminals organised in a brick-wall manner and with distinct ChAT bands clearly separating the ON- and OFF- sublaminae. Notably, only the nasal horizon, possessed ON-BC terminals (stained with PKCα) above the lower ChAT band, corroborating previous functional shift observations (Fig 2.1d).

Compared to the horizon, the thinner ventral and dorsal IPL displayed smaller and visibly "flattened" BC terminals, organised into apparently fewer than six layers. ChAT bands were also much less defined in these parts of the eye, and no longer demarcated two distinct bands. To better visualise the overall layering anisotropy of BC terminals, we computed the mean GFP signal along the entire IPL of the sagittal plane and normalised to local IPL thickness (Fig 2.3e, top). This showed clear

banding at the two horizons, but much less obvious banding in the remainder of the eye.

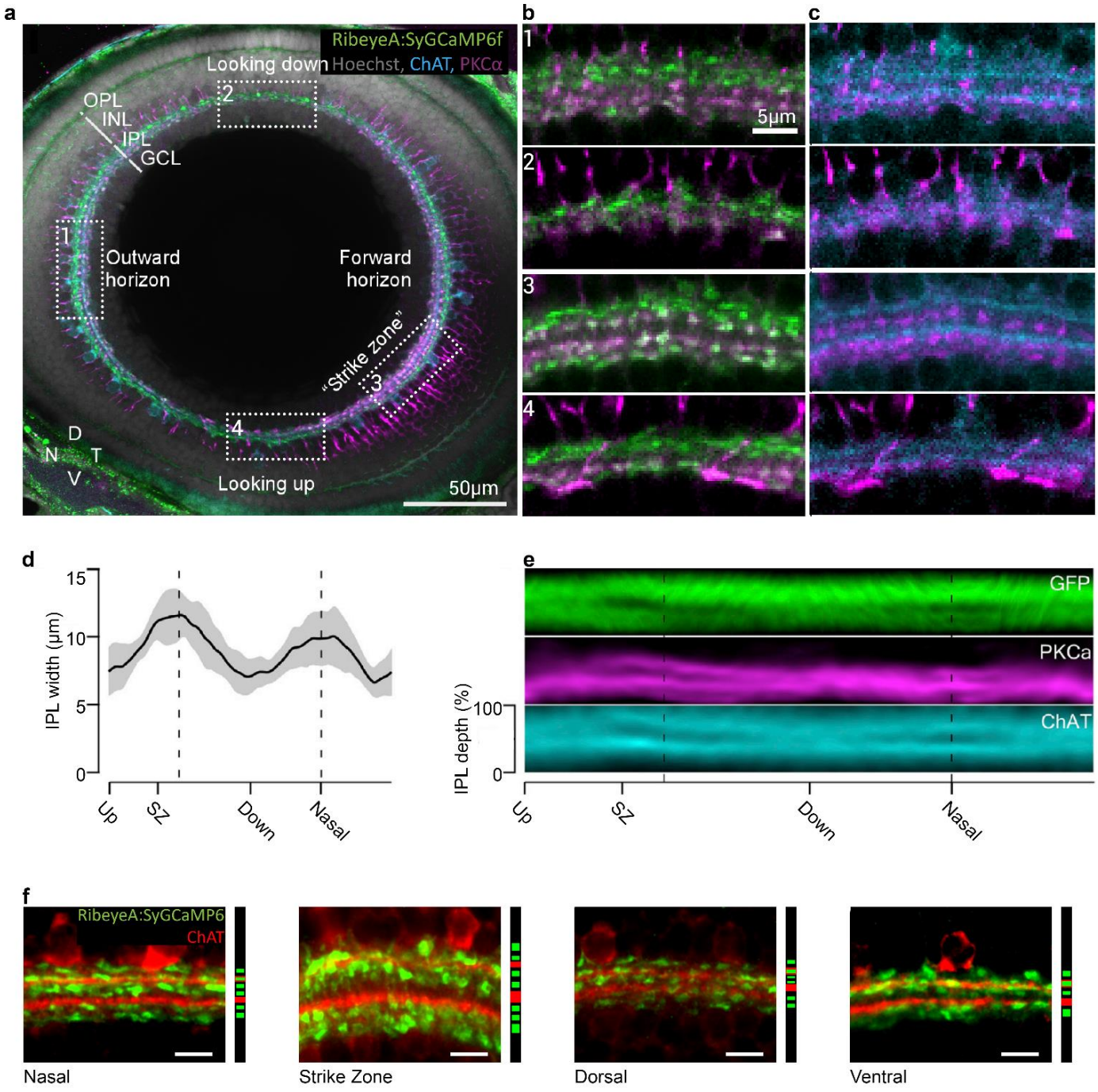

Figure 2.3 | An anisotropic retinal structure: a) Whole eye immunostaining of a 8 dpf larva in the sagittal plane expressing Ribeye:SyGCaMP6f, labelled against GFP (green), ChAT (cyan), PKCα (magenta) and nuclear structures (grey). **b) & c)** Higher magnification of the same eye at different eye positions (1: Nasal, 2: Dorsal, 3: *Strike* Zone 4: Ventral. **d)** Mean IPL thickness across n = 5 whole eye immunostainings. **e)** Mean signal for the three fluorescence channels in those same eyes, linearly represented along view direction. **f)** Magnified immunostainings of the four aforementioned regions using ChAT bands (red) as markers for BC terminals (green) positions across the IPL depth. Scale bars = 5 µm.

Next, the *strike zone* displayed enlarged round terminals with larger diameter. This region of the IPL also comprised many PKCα-positive terminals that reached far into the traditional OFF layer – much unlike in the remainder of the eye, but in line with the striking ON dominance of terminals in the *strike zone* (Fig 2.3e). More generally, BC terminals in the strike zone appeared to be particularly neatly organised into well-defined layers (Euler et al. 2014b). Interestingly, in the *strike zone*, and to some extent along the horizon, a sparse additional presence of terminals above the final OFF band or below the final ON band seemed to form potential seventh and eighth layers.

Next, we exploited the ChAT immunostaining, which labels the cholinergic SAC neurites, as depth markers (Fig 2.3f). In the nasal region two distinct layers can be observed below the lower band, two between the bands, and two more higher in the IPL (one on the upper band itself and one above). This could be written: 2/2/2. In comparison, the *strike zone* BCs distribution featured sporadic terminals beyond the traditional confines of the IPL and could therefore be described as 2-3/2/2-3. The thinner dorsal region appeared despite its "disorganised" arrangement similar to the nasal region with a 2/2/2 configuration. And finally, the ventral region displayed a 1/1/2 pattern, suggesting a less complex retinal organisation for surveying the upper visual field. The overall observed anisotropic stratification of BC terminals thus highlighted an anatomical specialisation with a variety of circuitry organisation confined to restricted areas of the retina, which was at least partially overlapping with differential labelling for PKCα and CHaT.

In contrast, confocal imaging of the zebrafish eye in the frontal plane – traversing the eye's horizon in full - (Fig. 2.4a) showed a thick and uniform IPL with concisely well-ordered layering, suggesting that the "brick wall" organisation observed in the nasal region of the sagittal plane (Fig 2.3f) spreads across the entire horizon, from nasal to temporal. This suggested that this neatly arranged organisation observed nasally is continuous across the entire horizon, implying a harmonized functional stratification of BC terminals in the IPL regions that serves the lateral horizontal visual field.

This frontal plane imaging also allowed the estimation of the full field of view covered by the sagittal plane two-photon recordings, indicated by the red band (Fig. 2.4a). From here, the effective field of view from functional recordings was estimated to be ~130° (represented in red Fig. 2.4b). The eye being still under development at this stage, parts of the retina positioned on the lens plane or ahead

of it may not be functionally mature. In comparison, the full monocular field of view for a larval zebrafish (grey) has previously being estimated to be ~163° by optokinetic reflex (OKR) experiments (Easter and Nicola 1996; Bianco, Kampff, and Engert 2011). At rest, the eyes are rotated forward at an angle of 18.5° relative to the sagittal body axis. This eye vergence appears to remain relatively constant (±7°) (Patterson et al. 2013). In this position, each eye surveys an essentially non-overlapping field of view on both side of the fish (Fig. 2.4b top).

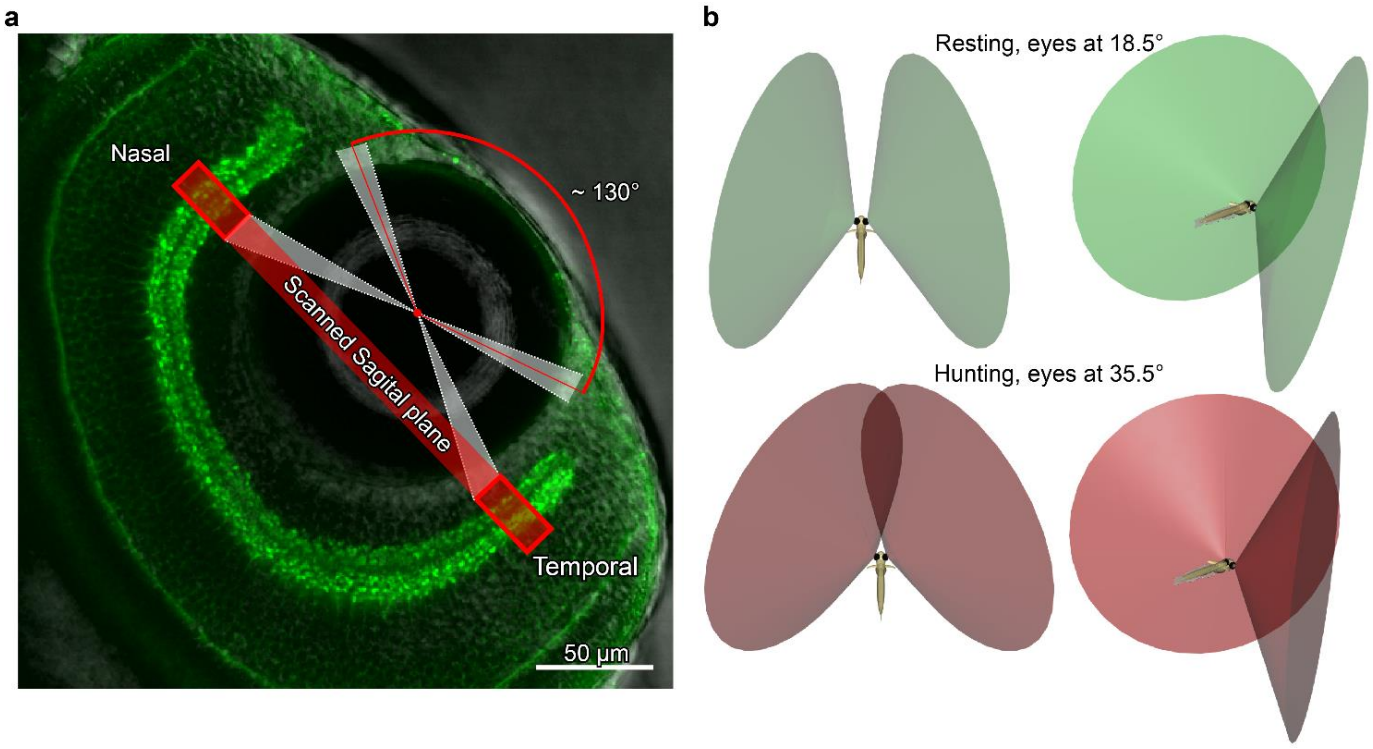

Figure 2.4 | A binocular vision: a) Whole eye immunostaining of a 7 dpf larva in the frontal plane (insert) expressing RibeyeA:SyGCaMP6f, labelled GFP (green). The two-photon recording sagittal plane was here highlighted in red, its field of view anatomically estimated. **b)** Representation of the larva field of view depending on its eyes orientation while resting or preying.

When hunting, the eyes converge to an angle of 35.5° relative to the body axis (Patterson et al. 2013). In this position, the fields of view overlaps in front of the animal giving rise to a binocular line of sight that presumably aids depth estimation, amongst other benefits (Fig. 2.4b bottom). Interestingly the part of the visual field that becomes binocular corresponds to the one processed by the temporal area, including the *strike zone*. This hereby increased the interest for this part of the eye to detect UV bright objects and to be able to assess the distance separating the larva from its target, which can then estimate an efficient and optimised striking / preying capture behaviour. While larval zebrafish adjust their eye position for

multiple purposes, such as gaze-stabilisation like during the OKR behaviour mentioned earlier (Dehmelt et al. 2018), the orientation of the eyes while preying is of particular interest here as it can be related to the need to detect UV-bright preys such as paramecia (Browman, Novales-Flamarique, and Hawryshyn 1994).

Taken together, structural differences observed within the IPL unveiled a broad range of anatomical specialisations across the visual field, and some of these regionalised organisations occurred to fit the previously described anisotropic functional mapping of BC terminals.

2.4 – A functionally chromatic anisotropy

In the above, we showed that the IPL structure and its BC terminals' chromatic profiles are position dependent. Larval zebrafish possesses at least 17 morphological BC types that can be either mono, bi or multi-stratified. And even though the larval retina was previously hinted to be non-uniform (Schmitt and Dowling 1999), no study to date has linked BCs morphology and function with eye position. Here we assessed functional BC types according to their chromatic profiles to establish if eye-wide functional variations can be linked to equally eye-wide morphological variations amongst specific BC types.

As a first step towards this goal, we assigned BC terminals to functional clusters. For this, our collaborator Philipp Berens used a mixture of Gaussian model to sort terminals based on their full temporo-chromatic response kernels (Fig 2.5). BC terminals fell into n = 26 clusters, which were assigned as before into three broad categories: Achromatic, chromatic, opponent. In addition, we divided the chromatic group into "standard chromatic" as well as "UV-dominated-chromatic" based on a striking predominance of UV kernels in several clusters – these latter were then dubbed "UV(Blue)-monochromatic", while the formers were titled simply as "chromatic", just as before. The resultant four major functional groups comprised: n = 5 achromatic clusters (Fig 2.5, 1–5); n = 9 UV(B)-monochromatic clusters (Fig 2.5, 6-14); n = 6 chromatic clusters (Fig 2.5, 15–20); n = 5 colour opponent clusters (Fig 2.5, 21–25); n = 1 discard cluster that comprised a wide mix of low signal amplitude ROIs. These groups were formally defined based on the relative amplitudes and polarities of each cluster mean's four chromatic kernels (Methods). Here again, the insets attached to each cluster represent their anatomical distributions within the retina along the IPL depth (dash lines representing the horizon).

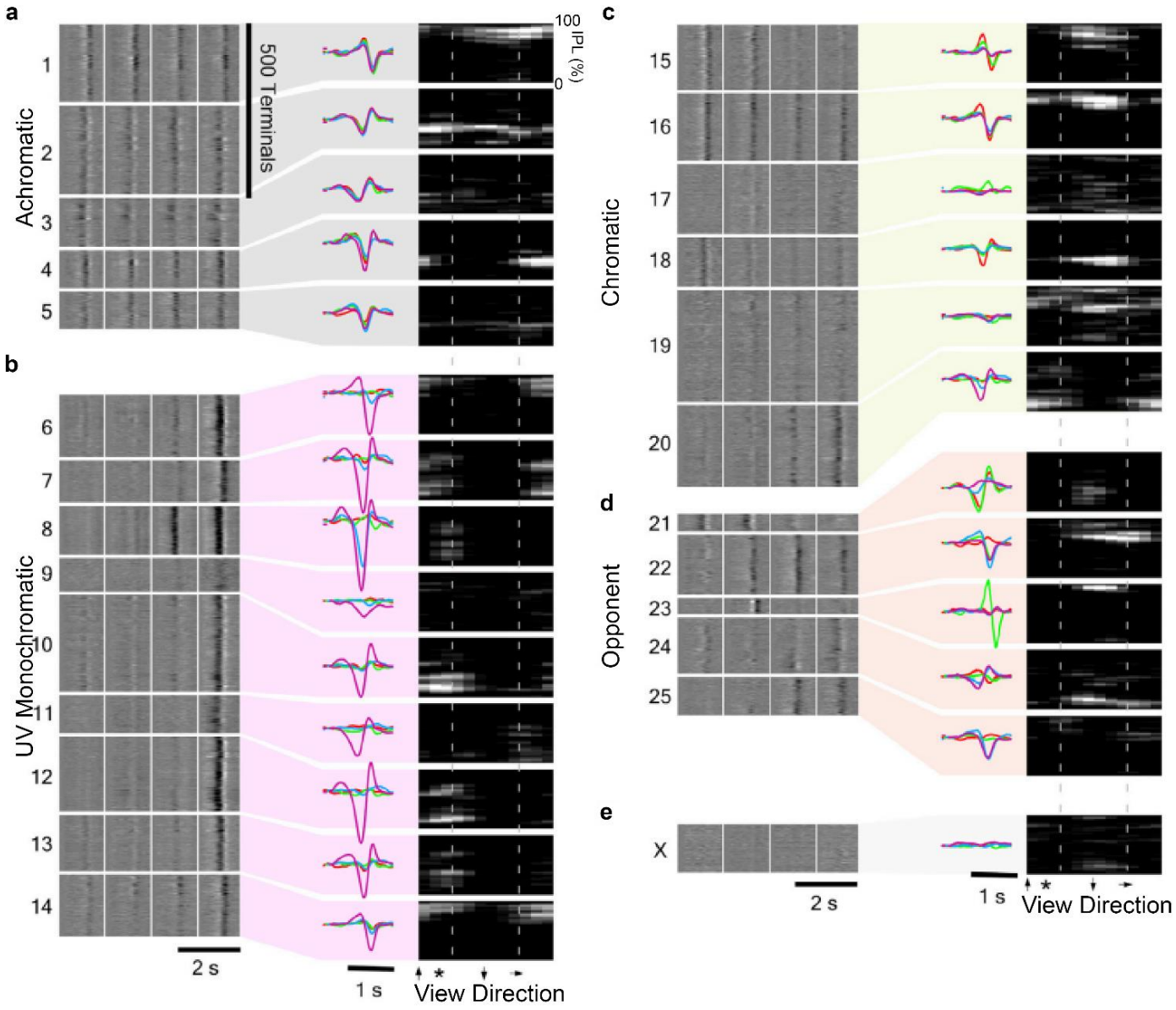

Figure 2.5 | Functional clustering of BC terminal responses: Mixture of Gaussian clustering of all n=4099 terminals based on their full temporo-chromatic kernels. Number of clusters defined by the Bayesian Information Criterion. **a)** Achromatic. **b)** UV-Monochromatic. **c)** Chromatic. **d)** Colour Opponent. **e)** Discarded kernels. *Clustering performed by P. Berens and figures generated by T. Baden for the publication (Zimmermann et al. 2018).*

Surprisingly, no cluster group was uniformly distributed across the entire eye (Fig 2.5 insets). Instead, individual clusters appeared to be neatly defined to an eye position and to a specific depth within the IPL either predominating in its upper or lower half. Amongst these, achromatic cluster 2 showed the most uniform distribution across the eye – in contrast to, for example, achromatic cluster 4 which was entirely absent from the dorsal eye. Notably, the vast majority of clusters were

restricted to one or two specific IPL-depth bands, tentatively suggesting that they may be linkable to specific BC types that stratify at different depths. This was also supported by the general absence of sparsely-distributed functional BC clusters.

Particularly striking were the UV-clusters, which were all essentially restricted to the ventral eye. A subset of these clusters exhibited an additional forward-bias to the *strike zone* – which were also the only clusters that displayed triphasic kernels (7,8,10,12&13).

In contrast, the dorsal retina was dominated by non-UV clusters, including several chromatic and all colour opponent clusters. The Red vs Green-Blue-UV opponency channel described earlier fell into cluster 22, and surprisingly extended from the nasal region up to the most dorsal part of the retina. BC terminals exhibiting this red-opponent kernel were found in the expected IPL layer, just above the lower ChAT band. Notably, in the dorsal regions, this specific profile could be found in an additional "upper" layer, suggesting a more complex retinal circuitry to differentiate long-wavelength signals coming from the lower field of view. Furthermore, this dorsal region was the only one containing terminals solely sensitive to green-OFF signals, just above the aforementioned Red-opponent layer. Therefore, despite being anatomically thinner and less obviously arranged into anatomical layers compared to e.g. nasal retina (Fig 2.3f), the dorsal region of the IPL appears to compute the most complex chromatic signals, well ordered in functional layers. These results called for an evaluation on how different groups of BC clusters types were distributed across the IPL layers.

2.5 – The functional anisotropy is organised in specific layers

To describe this functional layering, a map of the clusters' four functional groups was generated (Fig 2.6a). For each group, clusters were further subdivided into their ON and OFF components and the lower ChAT band was represented as a horizontal line to appreciate the anatomical IPL separation. As previously, horizons were represented by vertical dashed lines.

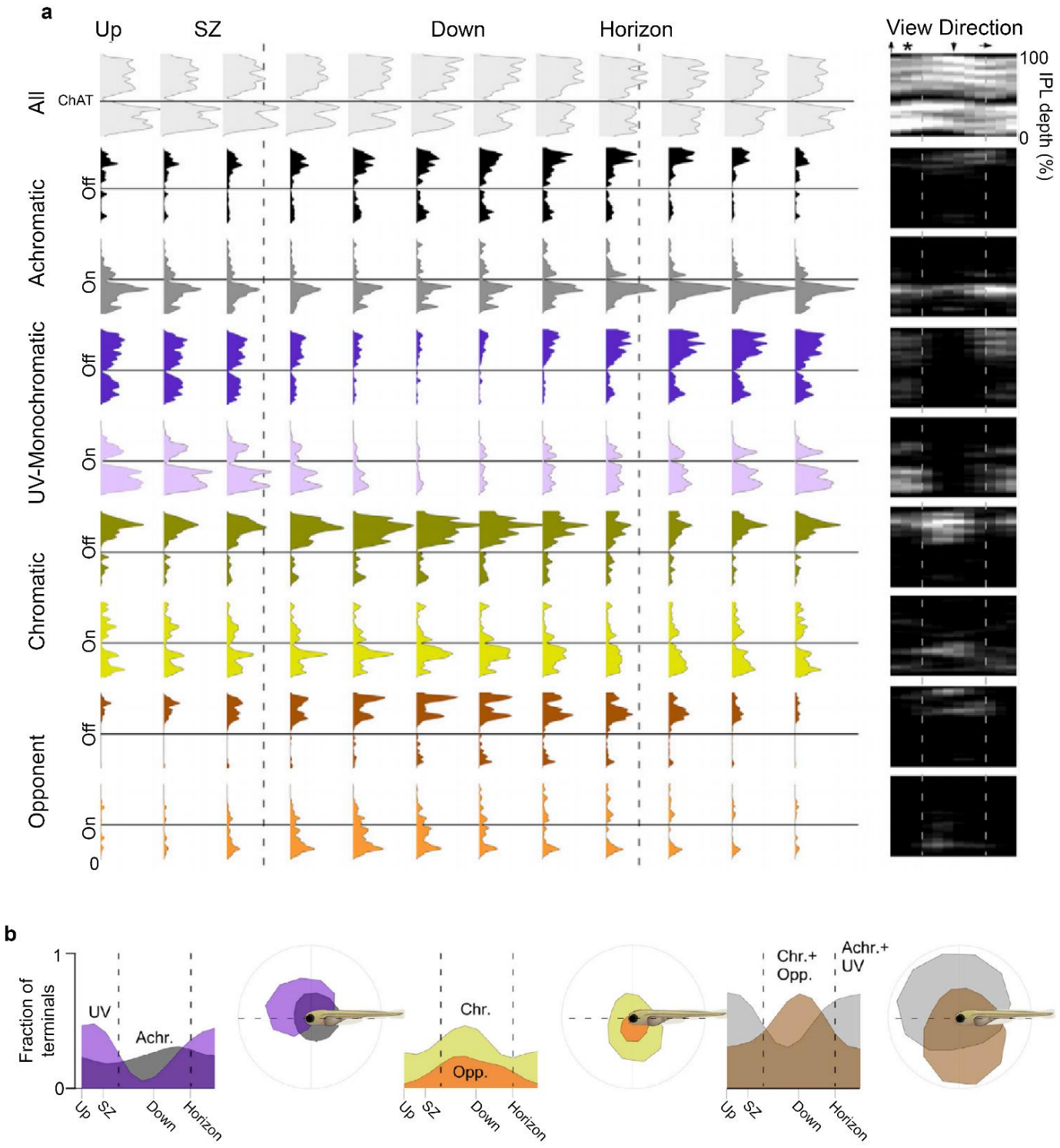

Figure 2.6 | BC functional distribution across the IPL: a) Histograms of terminal abundance across IPL depth and eye position for each functional group, subdivided into their ON- and OFF- component. **b)** Linear and polar representation of terminals functional groupings across the fish visual field. *Figures generated by T. Baden for the publication (Zimmermann et al. 2018).*

In addition, a map of all BC responses was added at the top (light grey). From this, the anatomical variation of IPL layer numbers along the retina was highlighted – now showing 6-7 layers in the region surveying the horizons compared to 4-5 layers ventrally. Second, only the ON and OFF achromatic groups stretched across the entire retina in their corresponding sublaminae, while other categories overall were more regionally biased. Though some OFF chromatic layers stretched through the retina, their position varied along the eye, getting closer to the ChAT band in the dorsal regions, apparently giving space for an additional OFF chromatic layer.

This confirmed previous observations that the dorsal IPL performs additional chromatic computations, but also gave an insight into general functional stratification: This was particularly clear from the OFF- colour-opponent terminals which only stratified in layers 1 and 3, leaving a gap that appeared to be filled by OFF- chromatic BCs.

From this map, one could suggest that the number of IPL layers fluctuated along the eye to incorporate additional chromatic circuits necessary to process asymmetric chromatic inputs from the visual world. Overall, the retinal anisotropy appeared balanced between the ventral regions specialised for UV processing and the dorsal regions for the computation of various chromatic stimuli (Fig 2.6b).

To better appreciate the stratification of these two domains, their response profiles were superimposed and plotted against each other. The resulting histograms revealed the functional layering arrangement for four retinal positions each representing an eight of the entire retina length (Fig 2.7a) (cf. Methods 6.6).

The UV-dominated ventral retina, for example, yielded two clear layers, 2 and 5, for a substantial population of chromatic and achromatic BC terminals, respectively. Temporally (in the *strike zone*), the ventral region was further intensified towards a UV dominance although the second layer conserved its OFF-chromatic dominance, suggesting that despite being dedicated to UV detection, the *strike zone* preserved some OFF- chromatic preferences. However, UV profiles were absent in the dorsal region such that chromatic and colour opponent layers were organised in an alternated fashion relative to UV clusters. In this region, each layer appeared to be chromatically dedicated to a specific function. In contrast, the nasal region displayed the most balanced number of terminals from each functional group along with a layered arrangement amongst all of them.

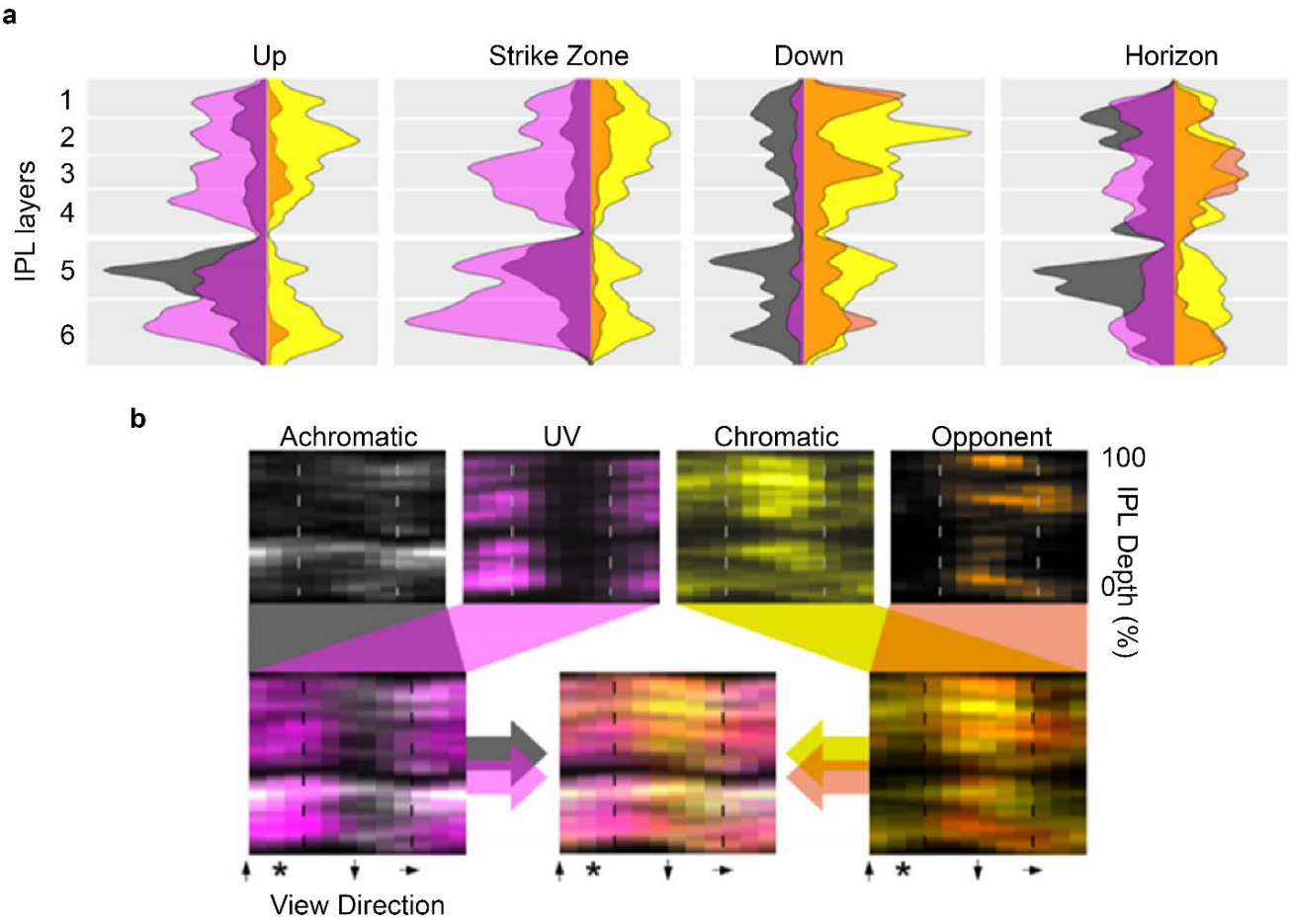

Figure 2.7 | A functional layering organisation: a) ON and OFF-collapsed histograms of the four response groups for four retinal regions. **b)** Colour-coded response groups plotted against eye position (x) and IPL depth (y). Throughout, colours indicate the functional groups: Achromatic (gray), UV(B)-monochromatic (purple), chromatic (yellow), and colour opponent (orange). *Figures generated by T. Baden for the publication (Zimmermann et al. 2018).*

Alternating functional layering thus appeared to be a fundamental basis of the IPL's chromatic processing circuitry. While achromatic and UV-monochromatic bands seemed to "merge" with each other, the chromatic and colour-opponent ones interdigitated much more perfectly (Fig 2.7b). This revealed a complex level of organisation for the naso-dorsal retina to process chromatic inputs. This was mostly interesting as the dorsal region, compared to the nasal retina, did not possess the thickest retina, nor the most well-organised anatomical layering and not even the largest number of IPL layers, but still conserved this chromatic functional layering. In the remaining part of the eye, the association of UV-monochromatic and achromatic BC terminals appeared to intertwine with the chromatic bands where the colour-opponent layers were now absent.

It is tempting to use the BC terminal population peaks from the above histograms to determine functional BCs stratification. However, it remains unclear how these functional layers should map onto the anatomically discernible 5-7 ones described in the literature. For example, the nasal region seemed to exhibit ~12 distinct interdigitated functional IPL streaks (Fig 2.7a), which long exceeds the detail of anatomical descriptions. Notably, BC functional types have traditionally been categorised based on the assumption of a small number of neat anatomical layers, which may have masked some of the nuance of their true functional-anatomical organisation (R. H. Masland 2001; Wässle 2004; Franke et al. 2017). Certainly, a complex chromatic layering as observed here for larval zebrafish has not yet been described in any other vertebrate.

Taken altogether, how does the inner retina develop such a rich functional division across the visual space?

2.6 – Building a functional anisotropic retina.

Our current knowledge on vertebrate retinal organisation detailed a diversity of BC types with distinct photoreceptor connectivity and functional properties stratifying in distinct layers (Euler et al. 2014b; Franke et al. 2017). As detailed in the previous chapter, the larval zebrafish retina possesses at least 17 distinct types of BCs, one being described as a mixed-BC. In comparison the well-studied mouse retina only possesses 14 types, one being a rod-BC (Wässle et al. 2009; Behrens et al. 2016). From these 14 types, only 2 appeared to process chromatic information based on their connectivity to either S- or M-cones (Chang, Breuninger, and Euler 2013; Behrens et al. 2016).

In this study at least 25 functional clusters of BCs were identified with distinct chromatic properties. This exceeds the 17 BC morphological types described in adult zebrafish based on connections to cone photoreceptors (Fig 1.3).

To reconcile this apparent mismatch between anatomical and functional BC descriptions, two non-mutually exclusive alternatives present themselves. First, anatomical descriptions may simply have underestimated the true number of BC types, and two, individual anatomical types might adopt different functional properties depending on their position in the eye. The latter could for example be facilitated by the distinct photoreceptor-type densities across the retina (Fig 1.2). To

explore these two possibilities, we next explored functional BC profiles in a genetically defined subset of BC terminals.

For this, we used the *xfz43* enhancer trap line, previously generated by fellow lab member T. Yoshimatsu (D'orazi and Yoshimatsu 2016) and in our possession. This *xfz43* enhancer drives the expression of reporter genes in a subpopulation of BCs during the larval development. Transgenic lines expressing this marker have been described to label three morphologically well-characterised types of BCs in larval retina: one OFF and two ON BCs (Zhao, Ellingsen, and Fjose 2009). Furthermore, *xfz43*-labelled BCs are expressed throughout the retina without any apparent regional specialisation, thus making them good candidates to test functional differences amongst similar BC types in different retinal positions. These three BC types possess distinct stratification patterns as well as PR-specific connections in the OPL. Two of these neuron types (1 OFF and 1 ON) preferentially contact R- and G-cones across large dendritic trees while the third one (ON) possesses a smaller dendritic field and indifferently form synapses with all cone types. It was therefore expected that *xfz43*-labelled BCs should display either achromatic or long-wavelength selectivity profiles.

A transgenic line was generated by crossing of the previously used *RibeyeASyGCaMP6f* (expressing a green calcium indicator in BC terminals) and a line expressing *Tg(xfz43:Gal4;UAS:ntr-mCherry)* which labelled *xfz43*-positive BCs in red. This allowed the recording of calcium response from all BC terminals (as before) while simultaneously identifying *xfz43* positive cells in the red fluorescence channel (Fig. 2.8a).

Using the same experimental protocols as before, 620 *xfz43*-positive terminals were recorded from 5 fish aged 5-8 *dpf*. Through reverse correlation, kernels were extracted from each BC terminal (Fig. 2.8b), of which 392 (63%) passed the quality selection criteria.

The anatomical distribution of *xfz43*-positive terminals (red) was superimposed over the distribution of all terminals previously recorded (green). As expected, they tended to stratify in two approximately confined IPL layers, one in the OFF band and another in the ON band. Next, although a small number of terminals expressing this marker was found all along the eye (Fig 2.8c), as a population they exhibited a clear bias for the ventral retina as well as the horizon.

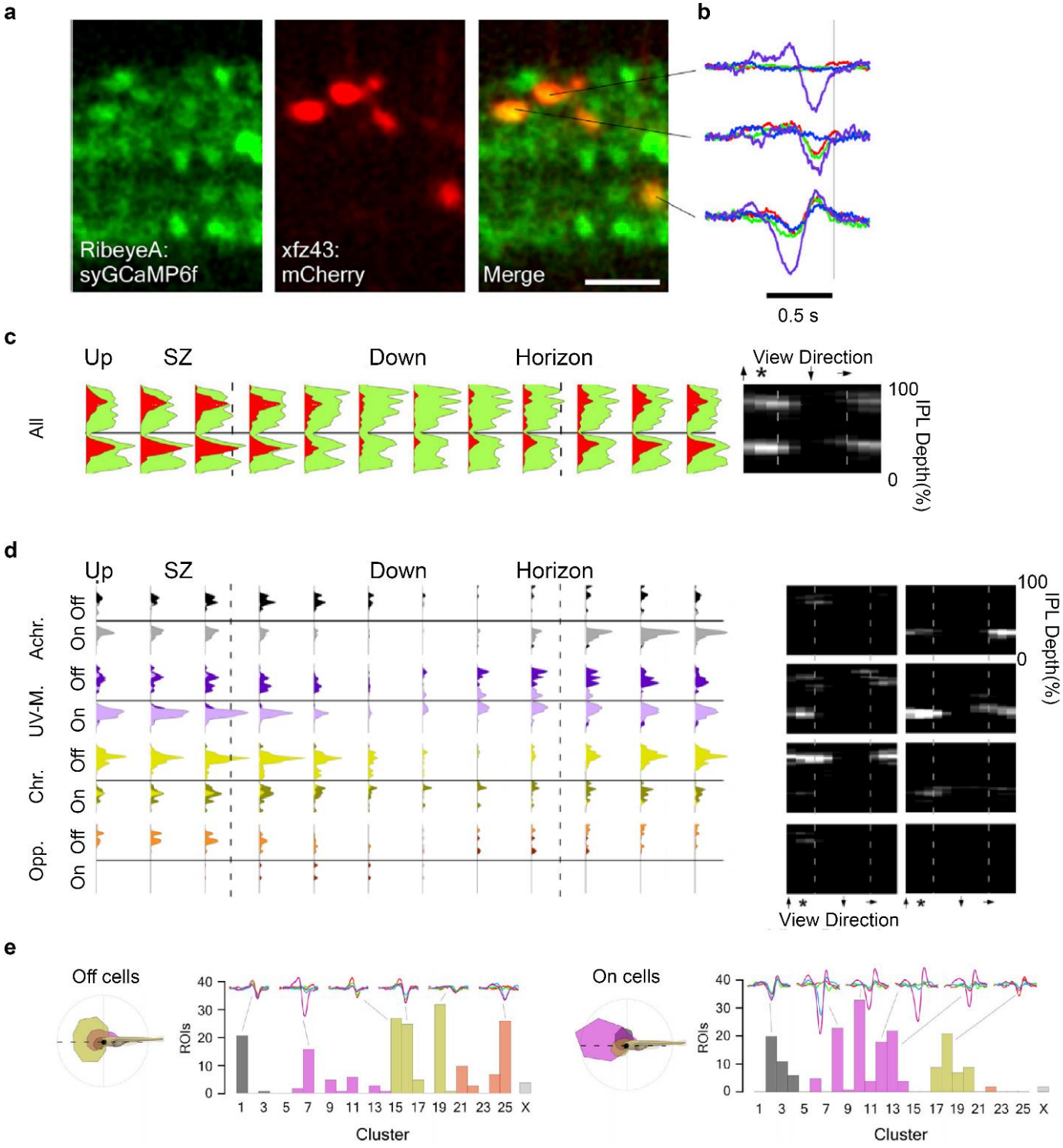

Figure 2.8 | Distribution of xfz43-expressing BC types: a) High-resolution two-photon scan of an IPL section in 7dpf larvae expressing *RibeyeA:SyGCaMP6f* (green) as well as mCherry under *xfz43* (red). The scale bar represents 5mm. **b)** Subsequent higher rate scans during light stimulation allowed recovering of tetrachromatic kernels from individual *xfz43*-positive terminals. **c)** Distribution of 392/620 *xfz43*-positive BC terminals (64 scans, 5 fish) across the IPL (y) and eye (x), superimposed on the distribution of all terminals from the same scans (green). Dashed lines indicate the forward and outward horizon, whereas the solid horizontal line indicates the position of the lower ChAT band. **d)** Histograms of xfz43 terminals abundance and their eye distribution (insets). **e)** Allocation of all *xfz43*-

positive anatomical OFF-terminals (left) and ON-terminals (right) to functional clusters and distribution of these terminals across the eye by functional group. *Figures generated by T. Baden for the publication (Zimmermann et al. 2018).*

xfz43 functional profiles were then assessed and assigned to the previously established functional clusters (Fig 2.8d&e). This revealed that while functional cluster allocation far from random, allocation was also substantially broader than the 3 profiles that might be expected from their dendritic connections to cones. Moreover, despite a general absence of direct connections to UV cones amongst *xfz43* BCs (D'orazi and Yoshimatsu 2016), UV-monochromatic were dominant amongst *xfz43*-labelled BCs located in the ventral retina. Nevertheless, about half of *xfz43* BCs did display the expected red-green bias. Together, this strongly suggested that BC functional profiles were shaped by both the direct cone inputs, as well as additional mechanisms, which appeared to differ with eye position.

Overall, *xfz43*-positive BCs displayed a broad functional diversity which cannot easily be explained by a possible misattribution of a small number of cell-types to functional profiles. Instead, it appears that a single BC "type" can give rise to more than one functional phenotype – likely at least in part driven by its local surrounding network – for example by way of amacrine cells. This was particularly striking in the *strike zone* where the UV cone densities were the highest and where UV-circuits predominated (Zimmermann et al. 2018). For example, the ON-T1 achromatic *xfz43*-positive BC which barely connects to a dozen cones, could theoretically be subject to an unusual high-gain UV input through a small number of contacts that could, in theory, shift the BC towards a UV-dominated response profile (Fig 2.1).

This hypothesis appears to be supported by more recent work from fellow lab members who demonstrated an enlargement of UV cone outer segments and an increased gain in the *strike zone* (Yoshimatsu et al. 2020). Additionally, these UV cones exhibited a slower recovery as a result of inputs from horizontal cells, which could lead to improved signal integration over time by postsynaptic circuits.

2.7 - BC chromatic processing match natural scenes chromatic statistics.

The zebrafish possesses 4 distinct cone photoreceptor types. If each cone input to a given BC can be either positive, negative, or absent (3 states), this could in theory lead to any of $3^4 = 81$ different chromatic computations (Fig 2.9a). However, most of

the possible spectral combinations appeared to not be used by BCs (Fig 2.9b). Instead, the larval zebrafish retina mostly relied on a small number of relatively simple short vs long wavelength opponency computations alongside achromatic and spectrally-biased channels (Fig 2.5).

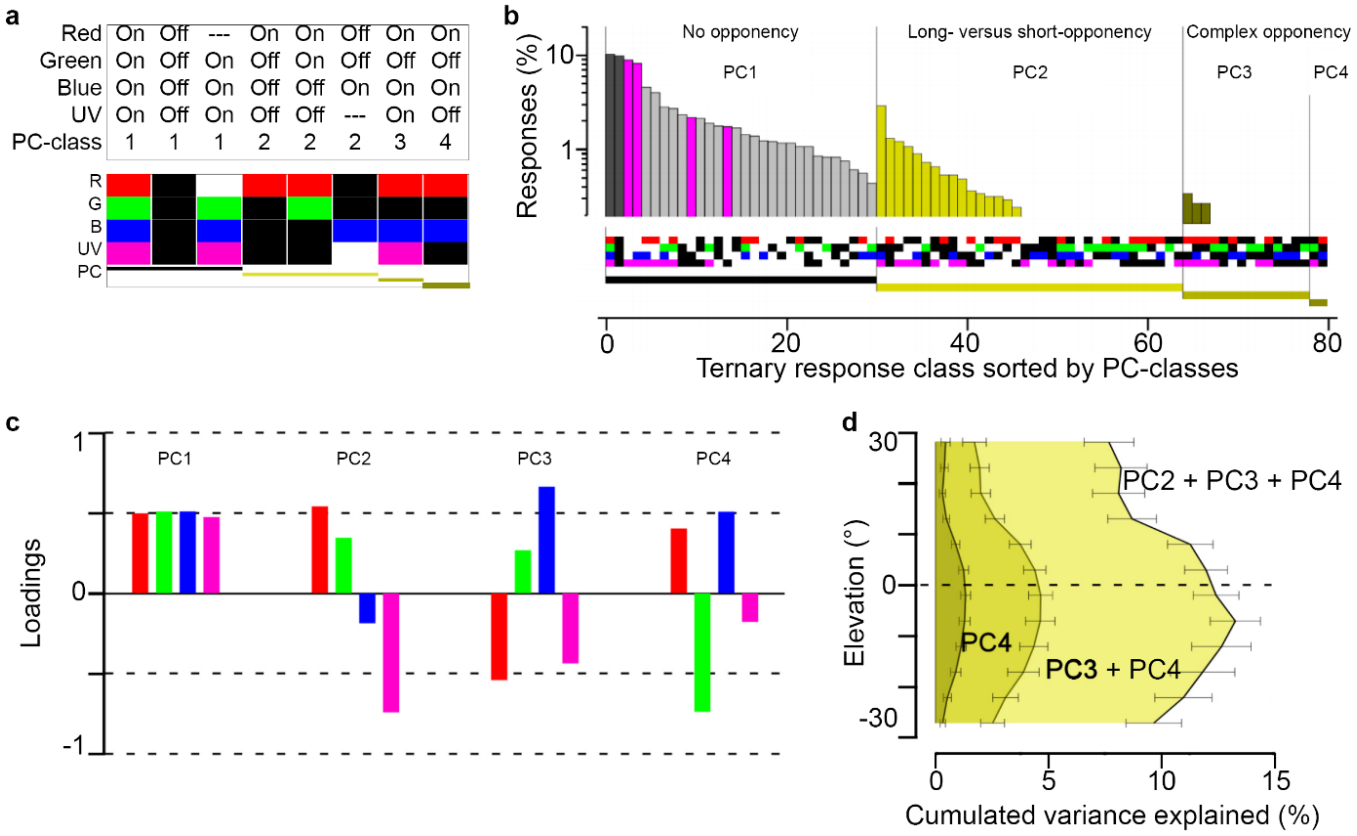

Figure 2.9 | BC chromatic profiles match natural statistics first principal components: a) Chromatic profiles association with the first four PCs. **b)** BC clusters ordered by PC class and population for the 80 possible RGBU combinations. Achromatic and UV monochromatic clusters were grouped together as non-opponent (PC1). **c)** Mean RGBU opsin loadings for four first PCs across all hyperspectral recordings. **d)** Cumulative variance explained by PC 2-4 calculated separately for 5° vertical slices across all hyperspectral recordings. *PC analysis and figures generated by T. Baden for the publication (Zimmermann et al. 2018).*

At various occasions we have discussed the necessity for this organism to survey chromatic light for specific tasks, like assessing a bright UV-bright prey in the upper frontal region (Novales Flamarique 2016). Understanding the developmental BC organisation and their anisotropic chromatic profiles therefore called for a study of chromatic light distribution in the natural environment where the zebrafish has evolved (Collin and Marshall 2003; Collin et al. 2009). As part of this published work

(Zimmermann et al. 2018), fellow Ph.D. student, N.E. Nevala recorded hyperspectral images from Indian rivers where zebrafish population can be found (cf. Chapter 3).

These recordings indicated that the chromatic content in nature varies with elevation (along the vertical axis) with most chromatic content being restricted along the horizon line. As expected, a diffuse UV background was identified in the upper visual field, and in opposition, long wavelengths corresponding to Red and Green colour channels were characterised in the lower visual space. This chromatic distribution appears to match the functional anisotropy described earlier (Fig 2.2, 2.6).

The sensory information theory discussed by Horace Barlow (Barlow 1961) suggested a link between natural visual scene statistics and neuronal response. In this regard, the efficient coding hypothesis predicts that the sensory processing should be adapted to natural stimuli (Simoncelli and Olshausen 2001). Sensory systems should therefore have evolved to extract as much information as possible while limiting neuronal resources by minimising visual redundancies (Attneave 1954; Olshausen and Field 1996; Ma and Wu 2011; Zhaoping and Zhaoping 2014).

To therefore assess which chromatic contrast predominated in the fish natural habitat, principal component analysis (PCA) was computed on these hyperspectral images across the zebrafish spectral dimension by using the RGBU channels as basis vectors (Fig 2.9c). Most of the image variance (~90%) was extracted form the first principal component (PC1) which characterised the image achromatic luminance information with near equal loadings across the colour channels, in agreement with previous work (Ruderman, Cronin, and Chiao 1998). PC2 corresponded to long versus short wavelength opponency and were mostly constricted to the horizon and lower visual field (Fig 2.9d). PC3 and PC4 reflected more complex opponencies and accounted together for less than 3% of the total image variance. Following PCs were not included as the amount of variance they accounted for was not significant.

Inner retina responses followed this distribution with the majority of BCs exhibiting achromatic (and UV-monochromatic) profiles. These non-opponent terminals can then be correlated to PC1 (Fig 2.9b). The second BC group in term of population response comprised long versus short opponency profiles which corresponded to PC2. It will be noted here that only about half of the possible long versus short opponencies were identified in the IPL. It only seems that such opponency

concerned the Red, and/or Green channels against the other ones (i.e. RGB against UV did not seem to be computed by this system). Finally, only a fraction of BC terminals appeared to compute more complex opponencies. In fact, only three combinations were identified, all extracting either Green or Blue channels from the association of the Red one with shorter wavelength channels. This group will therefore be associated with the third PC class. Interestingly, PC4 which corresponded to the intertwining of all colour channels were not computed by the BC terminals.

Overall, the zebrafish retina besides being optimised to assess asymmetric chromatic light signals, also computed the natural chromatic information in an efficient manner, extracting the achromatic and chromatic signals in such way that it almost perfectly fit the prediction model obtained from natural statistics. Here, about all visual scenes chromatic variance can be projected into three basic vectors (PCs), suggesting that the fish cone sensitivities and their underlying retinal circuit processing were determined by the colour statistics from its natural habitat (Lewis and Li 2006).

2.8 – Conclusion

In this chapter, we detailed our attempt to functionally characterise BC chromatic profiles. We identified more functional BC types than morphology types previously reported in the literature. However, our approach that classified functional profiles relies on the identification of ROIs which correspond to single BC terminals. Therefore, mixed BCs with multiple terminals, which may display different chromatic responses along the axonal tree depending on lateral inhibition from ACs, may end up in distinct functional clusters despite belonging to the same neuron. However, we observed in several clusters, especially the UV-monochromatic ones, that defined chromatic profiles, while constrained to a specific retinal region (Fig. 2.5 insets, y-axis) were present at two or three distinct IPL depths (Fig. 2.5 insets, x-axis). Such distribution likely indicates multi-stratified BCs whose terminals exhibit similar chromatic profiles along the axonal length. Interestingly, we will note here again that such profiles are mostly confined to the *strike zone*. Overall a full investigation of BC chromatic profiles would need to be performed with specific BC type promoters or molecular marker. The research for developing transgenic lines with such markers is still ongoing at the time of writing. Also, EM reconstructions would in the future help determining the correlation between BC functional type and

anatomy (PRs connections, receptive field size, soma position, axonal stratification, ACs and RGCs connections).

While assigning BC terminals to chromatic profiles, we also raised concerns about potential fluorescence signal interferences between neighbouring BC terminals that in turn might lead to a chromatic profile misclassification. As previously detailed, the key parameter by which our microscopy setup PSF could generate an apparent signal overlap is the expression profile of the calcium indicator (the pixel size being related to the digital zoom (angle of mirror deflection) and the scanning resolution). Such expression profile was regularly checked by imaging at high resolution (slow) scans at different depth, both above and below the targeted BC terminals. If during this control check we did not observe fluorescence expression on other structures, we assumed that imaging on these ROIs would not generate additional overlapping signal. Furthermore, where such overlap would happen, our ROI selection criterion which discards ROIs with at least one spectral kernel peak-to-peak amplitudes that does not exceed a minimum of two standard deviations, would have likely disqualified it (About a third of ROIs are excluded in each experiment). Moreover, the probability that a signal mixture between two overlapping BC terminals gave rise to a genuine temporo-chromatic kernel is low and would have end up in the x cluster (about ~50 ROIs (Fig. 2.5e)). Finally, when we consider that our less populated cluster account ~50 ROIs; if such miscategorised unique kernel was to be generated it is unlikely that it will systematically be spatially distributed in distinct retinal position and IPL depth. Though, we observe that all functional clusters are distinctly distributed along these two axes.

Nonetheless, our work highlighted an unprecedented degree of visual chromatic specialisation in a vertebrate retina. It was shown that the distribution of retinal functions finely matched the distribution of chromatic features in the larval zebrafish environment by functionally surveying the entire BC class *in vivo*. This is particularly clear for the chromatic circuits predominately processing chromatic signals from the horizon and lower visual spaces where most chromatic content could be found in the fish natural habitat (Fig 2.10a). These retinal circuits displayed a striking level of organisation within the IPL through a neat arrangement of functional layers which matched the differential chromatic contrasts observed in nature (Fig 2.9 c&d).

The number of BCs exhibiting UV-monochromatic profiles and their functional diversities (Fig 2.5) favour the consideration of UV as a separate chromatic channel that almost exclusively exists within the *strike zone.* UV-sensitivity in the anterior

field of view is necessary for the detection of UV-bright prey and body positioning for estimating movements required for capturing prey. Moreover, short-wavelength light being scattered in shallow water by a combination of the Rayleigh effect and interaction with dissolved organic matter and sediment generates a UV-diffuse background in under-surface waters where the larval zebrafish navigates (Cronin and Bok 2016). Landscapes, most larger objects, and likely predators, which usually do not strongly reflect UV light, will then appear as UV-dark-silhouettes for the UV-sensitive larva (Fig 2.10b). UV photoreception may thus additionally participate in navigation and predator detection (Losey et al. 1999), as well as – presumably - traditional colour vision.

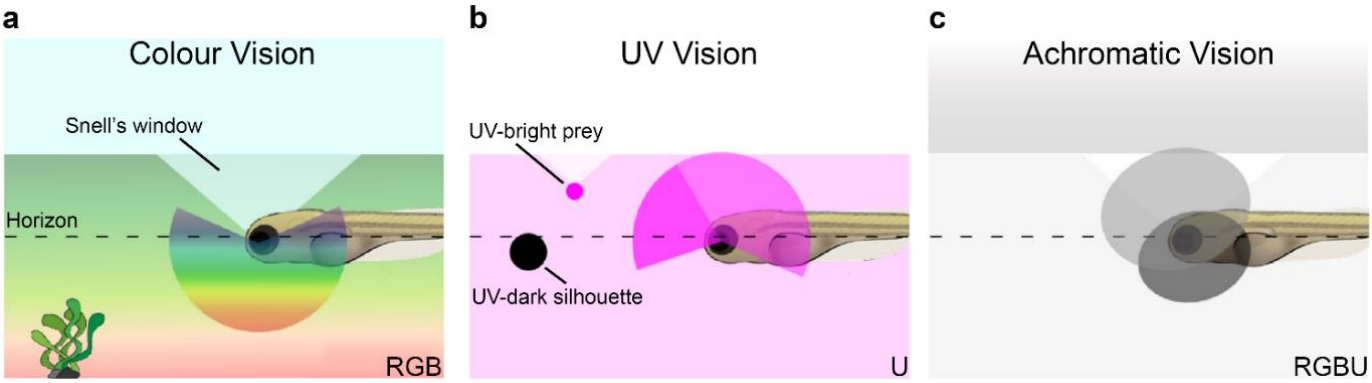

Figure 2.10 | The larval zebrafish eye's chromatic organisation for vision in nature a) Retinal circuits for colour vision are biased towards the horizon and lower visual space where most of the chromatic content could be found in the fish natural environment. **b)** UV circuits dominate the upper visual field where short wavelengths arise underwater. An emphasis was put on the highly UV-sensitive strike which surveys the upper-frontal visual field (darker purple) which is probably used for prey capture and the detection of UV-dark silhouettes. **c)** Achromatic circuits can be found across the entire eye with ON-circuits (light grey) principally dominating the upper visual field while the OFF-circuits (darker grey) dominated the lower one. Above each fish (and paramecia), the clear triangles represent the Snell's window (~97°). *Figures generated by T. Baden for the publication (Zimmermann et al. 2018).*

Furthermore, the dedication of the *strike zone* region to the detection of short wavelengths could be anticipated by the anatomical specialisation of the region: Higher UV cones density, longer UV cone outer segment, larger INL and IPL and increased number of IPL sublaminal layers, all suggesting an enhanced BC processing of short wavelength signals in this part of the eye. Moreover, these unique structures being specifically located in the part of the eye where the

detection of UV would be the most relevant to the organism, highlights an evolutionary strategy to develop dedicated structures, functionally specialised to the detection of short wavelengths.

The intricate structural and functional organisation of chromatic circuits within the retina of a developing organism that just started autonomous feeding demonstrated the importance of spectrally nuanced vision for the survival of this organism. Previous studies have identified retinal and pre-tectal neuronal pathways dedicated to the identification of preys (Semmelhack et al. 2014; Bianco, Kampff, and Engert 2011; Antinucci, Folgueira, and Bianco 2019). Additionally, UV photoreception was demonstrated to enhance feeding behaviours in zooplanktivores (Browman, Novales-Flamarique, and Hawryshyn 1994; Jordan et al. 2004; E. R. Loew et al. 1993). Here, it is hypothesised that UV circuits in the *strike* zone form a dedicated retinal pathway for the detection of UV-visual cues involved in feeding and, and possibly in escape behaviours.

If adaptation of retinal processing for asymmetric natural features have previously been reported in previous studies and other vertebrate models (Szatko et al. 2020; Sabbah et al. 2017; Warwick et al. 2018; Tom Baden et al. 2013; Behrens et al. 2016), the presented work particularity was to show a highly specialised retinal region (the *strike zone*) where UV-ON circuits dominated the upper frontal visual space, at the expense of all other chromatic processing. Although, while the retinal UV specialisation appeared to be the most prominent, other regional-specific structural features displayed anisotropic chromatic functions: Dorsal BC terminals for example, which form a neat brick wall organisation (Fig. 2.3f), also displayed the highest level of chromatic organisation into a well-defined functional layering organisation (Fig. 2.6a, 2.7), suggesting here as well a strong correlation between structural and functional organisation.

It should be noted here that fish used for experimentation have been bred indoors for many generations and have never been accustomed to UV light until they were placed under the microscope to be stimulated with these short wavelengths. It can be hypothesised that zebrafish larvae in the wild may be more sensitive to UV light or may display a different set of chromatic profiles. However, despite having been housed and bred in “unnatural” conditions zebrafish larvae still possess a regional UV specialisation, suggesting that many of these specialisations are hard coded within the retinal development, reinforcing their importance for this organism’s vision.

Data discussed in this chapter were obtained by stimulating the colour channels with equal light intensities corresponding to a low photopic regime. Such light stimulation does not reflect what the larval zebrafish eye might be tuned to perceive in natural scenes. It is rather expected that natural chromatic statistics describe lower light intensities for short wavelengths. In consequence the PRs UV high-gain observed in the *strike* zone (Yoshimatsu et al. 2020) might cause a local saturation following the UV light stimulation, potentially concealing the identification of other chromatic profiles in this region. Overall, this calls for further inner retinal investigations under “natural chromatic light” conditions.

Another point to note regarding the stimulation approach is that in this chapter, only full field stimulation was used, giving indications on BC chromatic preferences but lacking information about spatial chromatic contrast, the ability for a visual system to differentiate two neighbouring objects with similar intensities (Witzel and Gegenfurtner 2015). Future investigations therefore also call for a spatio-chromatic approach under “natural” light conditions.

Over developmental time, the outer retina gradually adopts a mosaic photoreceptor pattern, presumably adapting its visual circuits to the changing visuo-ecological needs. It is therefore expected for the inner retina to adapt accordingly, potentially rendering the extreme UV-light sensitivity of the *strike zone* role obsolete as the adult zebrafish is expected to rely on a wider range of spectral and other cues to detect prey and other high acuity tasks (e.g conspecific/mate recognition). A proper categorisation of BC types linking genotyping, anatomy, distribution, and functionality is then needed to understand how this retinal system develops over time. Visual adaptation to new chromatic cues within the same natural scenes potentially yields a better representation of different characteristics from similar stimuli.

Chapter 3

Development of Open Source Hardware to circumvent experimental limitations.

Designing flexible wavelength light stimulators for coupling with two-photon microscopy.

If we seek for the simplest arrangement, which would enable it (the human eye) to receive and discriminate the impressions of the different parts of the spectrum, we may suppose three distinct sensations only to be excited by the rays of the three principal pure colours, falling on any given point of the retina, [...] while the rays occupying the intermediate spaces are capable of producing mixed sensations.

Thomas Young, Chromatics – Encyclopaedia Britannica (1824)

In the following chapter we will detail the work carried out to improve our recording systems by focusing on the chromatic stimulation part. This led to the development of an opensource stimulator which was published as **LED Zappelin': An open source LED controller for arbitrary spectrum visual stimulation and optogenetics during 2-photon imaging.** Zimmermann MJY, Chagas AM, Bartel P, Pop S, Prieto Godino LL, Baden T.

3.1 – Introduction

In the previous chapter we have seen that the larval zebrafish retina is anatomically and functionally organised in an anisotropic manner. This organisation is thought to have evolved to optimise the detection of chromatic cues from this organism's environment to direct behavioural responses (Collin and Marshall 2003; Collin et al. 2009). We particularly focused on the *strike zone* organisation which displayed the larger density of UV-cone photoreceptors and contained BCs apparently specialised for UV light detection. Moreover, the *strike zone* corresponded to the region of the retina surveying the frontal-upward visual field of the zebrafish, namely a position in which the fish was expected to detect and capture prey. Thus, the location, structure and function of the *strike zone* appeared optimal to direct UV-guided behaviours.

The sensory drive hypothesis, states that an organism's environmental components influence the evolutionary trait of its sensory features in a predictable direction (Endler 1992b; 1992a; Cummings and Endler 2018). Therefore, to accurately appreciate the functional organisation of an organism's retina, one must assess the natural environment in which its vision has evolved (Munz and McFarland 1977; T. Baden and Osorio 2019; Luehrmann et al. 2020). This is even more necessary since visual ecology studies have reported aquatic environments to be fairly variable in illumination spectra (Lythgoe 1979). Such variation mostly being due to the diversity of water composition on dissolved organic elements and sediments (Jerlov, 1976; Loew and McFarland 1990).

If we could extract from the zebrafish natural scene statistics, the average underwater illumination spectra, we could then reproduce it in our laboratory to stimulate larval zebrafish retinae. As feature selectivity in sensory neurons is maximally informative to low stimulation dimension variations (Sharpee, Rust, and Bialek 2003; 2004; Rajan and Bialek 2013), it is expected to extract more information from neuronal responses to natural signals.

3.2 – Determining naturalistic light illumination

In 2017, fellow lab members designed an open source hyperspectral scanner consisting of a compact CCD spectrometer (CCS 200/M, Thorlabs, Germany) ranging from 200 to 1000nm coupled with two mirrors mounted on servomotors (Nevala and Baden 2019). Such device was used to take thousand pixels spectra

images, centred on the underwater horizon of zebrafish natural habitat in north-east India. Images resolution was set to correspond to the reported larval zebrafish visual acuity from behavioural studies: ~1.6° (Haug et al. 2010). Data collection resulted in a series of full-spectrum images from multiple sites, from which an average illumination spectrum was extracted (Zimmermann et al. 2018). As previously described in chapter 2, the spatial distribution of chromatic content within a natural scene matches the distribution of photoreceptors and BCs functional tuning. Compared with an illumination spectrum taken above the water in similar condition, a shift towards long wavelengths can be observed, due to a Rayleigh scattering of short wavelengths in the medium (Fig 3.1a). This suggested that the zebrafish red cones were strongly driven in its natural habitat in comparison to shorter wavelength sensitive cones. As we have seen in the previous chapter, the *strike zone* appeared to be dedicated to UV-light detection. With UV-light being strikingly attenuated in these shallow waters, a sensitive detection system is then required for these survival-necessary wavelengths. This also indicated that UV-light stimulation performed under our two-photon microscope might be significantly tuned down to not over-stimulate this already highly sensitive system.

To estimate the spectral content available to the larval zebrafish retina in natural conditions, the above-mentioned underwater spectrum was multiplied with each fish opsin spectral sensitivity template (Fig 3.1b). This yielded an estimation of the relative photon catch rates in nature for each opsin. It can be noted that the red channel one had the highest absorption and peaks at the same wavelength as the mean underwater spectrum peak, which suggested that red cones were strongly driven by these natural chromatic statistics. Overall, a clear decreasing chromatic ratio towards shorter wavelengths appeared (Fig 3.1c), confirming the necessity for a highly sensitive UV channel, as the signal power for this channel was about 7% of the red one.

This chromatic ratio was instructing as it enabled the calibration of the stimulation LEDs in relation to each other. Nonetheless, to avoid over-stimulation of the sensitive UV-channel and to match the light stimulation a zebrafish larva might receive in the wild, it was first needed to estimate the amount of photons each cone received to then adjust the LEDs power accordingly.

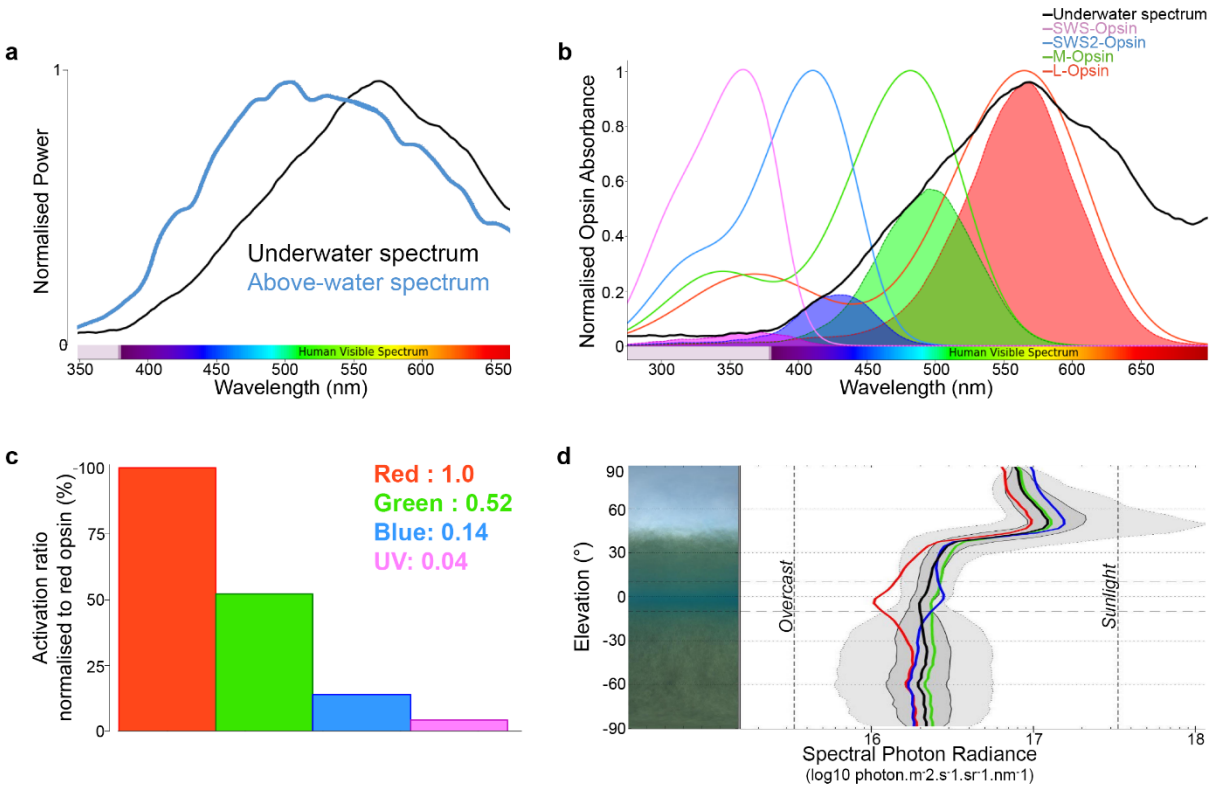

Figure 3.1 | Chromatic content distribution from the zebrafish natural habitat. a) Mean of n = 31,000 peak-normalized underwater spectra (31 horizon-aligned scenes of 1,000 pixels each) and mean spectrum of the sky in zenith above the water. **b)** Convolution of the zebrafish's four cone absorption spectra with the mean natural spectrum were used to estimate the relative photon catch rates in nature. **c)** Estimation of the relative power each cone receives under natural light conditions, normalised to red cones. **d)** (Left) Mean of n=43 scenes from the outer barrier site in Australia. (Right) Mean spectral radiances from the environmental scenes as a function of elevation angle. Red, green and blue spectral bands are represented by coloured traces, with a black trace for the full spectral width, and the range of radiances (the contrast range for white light) for 50% (dark grey) and 95% (light grey) confidence intervals. The dashed lines are arbitrary indications intended to aid orientation on the radiance scale (Adapted from unpublished dataset shared by Dan-Eric Nilsson. (Nilsson and Smolka 2021).

Internal discussions with our collaborator Dan-Eric Nilsson from the university of Lund, led to a photon radiance (L_p) estimation of $12*10^{16}$ photon.m^{-2}.s^{-1}.sr^{-1}.nm^{-1} for red-light illumination (600-700nm) at the underwater horizon (Fig 3.1d). To obtain this estimation, Pr. Nilsson and his associate Michael Bok measured the illumination spectra in various natural scenes with a filtered-monochromatic camera and extracted from it the spectral photon radiance for specific wavelength along with their distribution across scenes elevation (Warrant, Johnsen, and Nilsson 2020).

Since our stimulation LEDs were focusing onto the retina, the number of photons that each cone was receiving needed to be estimated. First, we had to consider the amount of light that reached the retina. As we work on *in vivo* animals, the amount of light passing through the eye pupil must be taken into account. The pupil diameter was estimated to 50 µm (Fig 2.4a). Therefore, the amount of red-light (angular photon flux, P_{α}) reaching the retina was:

$$P_{\alpha\,(Red)} = L_{p\,(Red)} \times \pi . r_{(pupil)}^{2}$$

From the chromatic ratio, the photon radiance each cone is receiving from the natural white light could be estimated, along with the angular photon flux for each opsin:

Colour channel	Red	Green	Blue	UV
Chromatic ratio	1	0.52	0.14	0.04
Angular photon flux (photon.sr^{-1}.s^{-1}.nm^{-1})	9.42*10^{7}	4.9*10^{7}	1.32*10^{7}	3.77*10^{6}

Cone outer segment diameter have previously been measured for the zebrafish (Allison et al. 2004). Therefore, the collection angle for each cone can be measured:

$$\Omega_{(Cone)} = \frac{A(Cone)}{r^2}$$

Where Ω is the cone collection angle in steradian, A the cone outer-segment area and r the eye radius (150µm, c.f. Fig 2.3a).

The photon flux (φ) in photon.s^{-1} for each cone can then be determined:

$$\Phi_{(Colour\ channel)} = P_{\alpha\,(Colour\ channel)} \,.\, \Omega_{(Cone)} . \sigma$$

σ being the half-width of the opsin absorption spectra and corresponds to ~ 100nm

Colour channel	Red	Green	Blue	UV
Outer-segment diameter (µm)	2.4	2.4	2.8	2.6
Outer-segment area (µm^{2})	4.52	4.52	6.16	5.31
Cone collection angle (Sr)	2.01*10^{-4}	2.01*10^{-4}	2.74*10^{-4}	2.36*10^{-4}
Photon flux (photon.s^{-1})	2.22*10^{9}	1.16*10^{9}	3.11*10^{8}	8.90*10^{7}

Such information was highly valuable to generate a light stimulation similar to the zebrafish natural scene statistics. As stated in the previous chapter, we were using a tetrachromatic stimulator from which each LED has been selected and filtered to match the peak spectral sensitivity for each cone. In the experiments detailed in this chapter, these four LEDs had been equally calibrated to a power of 40 nW corresponding to a low photonic regime. Now the task was to estimate the power of each LED that will correspond to the photon flux each cone could have received in the wild.

The energy flux (P_{eFlux}) which determines the rate of energy transfer through a surface (here the cone outer-segment areas) is wavelength dependent and depends on the wavelength-dependent photon energy (Q) described by the Planck-Einstein relation:

$$Q_{(\lambda)} = \frac{c.h}{\lambda}$$

Where c is the speed of light (299,792,458 $m.s^{-1}$), h the Planck constant ($4.135667.10^{-15}$ eV.s) and λ the considered wavelength.

$$P_{eFlux(\lambda)} = \Phi_{(Colour\ channel)}.\ Q_{(\lambda)}$$

Colour channel	Red	Green	Blue	UV
LED peak wavelength (nm)	587	487	427	372
$Q_{(LED)}$ ($eV.photon^{-1}$)	2.11	2.55	2.90	3.33
$P_{(eFlux)}$ ($eV.s^{-1}$)	$4.7*10^{9}$	$2.94*10^{9}$	$9.04*10^{8}$	$2.96*10^{8}$
$P_{(eFlux)}$ (nW) *	7.53	4.72	1.45	0.47

* 1eV = 1,602,176,364 10^{-19} J

In conclusion, to reproduce a “natural white light” during imaging experiments, the stimulator LEDs must be set at 7.5, 4.7, 1.5 and 0.5 nW. This is quite different from the equalised settings at 40 nW that was used in the experiments described in Chapter 2. Therefore, by applying these light intensities, it was hoped to observe different functional profiles, especially from the *strike zone* which was apparently saturated by UV-light.

3.3 – Overcoming hardware limitations

In the previous chapter, we described tetrachromatic light stimuli that were presented to the larval zebrafish retina. Such stimuli were generated by a custom-built electronics system consisting of four LEDs driven by a microprocessor board controlled through the Arduino IDE software. This system was an adaptation from the one described and implemented in previous studies from the Euler lab at the university of Tuebingen, Germany) (Euler et al. 2009; Breuninger et al. 2011; Tom Baden et al. 2016; Franke et al. 2017).

The aim of this stimulator was to drive LEDs in synchronicity with two-photon microscopy. Combining light stimulation with two-photon imaging can prove to be challenging due to potential interferences between the fluorescence emission and the stimulus light spectra. Usually, stimulation lights are band-passed filtered, so their wavelengths do not overlap with the fluorescence detection bands. However, the previous tetrachromatic experimental design did not permit a neat spectral separation from the PMTs detection range (Fig 3.2a). To then avoid light artefacts in the image and prevent rapid decay to the sensitive fluorescence detection equipment (in our case photomultiplier tubes, PMTs), a temporal separation could be made between these lights to reduce the crosstalk, for example during the scan retrace of a raster scan (Fig 3.2b). The stimulator system therefore aimed to limit flickering artefacts by keeping the rate of interweaving stimulation beyond the integration time of the to-be-recorded stimulated system (Euler, Franke, and Baden 2019).

This system achieved its goal for our first study (Zimmermann et al. 2018). However, it presented major defaults which limit experimental designs. In particular, the stimulator relied on the popular ATMega328 processor, which output 8 bits PWM (Pulse-Width Modulation) resolution, meaning that LEDs duty cycle can only be modulated through 256 values. The white noise stimulation in the previous chapter consisted of switching on and off LEDs up to their maximal values (0 to 255). To apply natural statistics values to the stimulators (while keeping an equal LED calibration to 40 nW, which needed to remain constant for co-running experiments), these 256 degrees of freedom were far too small to be sufficient. For example, the UV LED cannot be accurately tuned from the equal power value (40 nW) to the natural statistics (0.47 nW). Also, any smooth sigmoidal modulation of light intensity would not be achievable. Moreover, driving LEDs with a microcontroller led to a non-linear relationship between PWM and light intensity

(brightness), which caused misinterpretation between the stimulation light value applied and the actual light reaching the fish eye.

Another negative point of the ATMega328 was its relative slow processing power (16 MHz). If no flickering artefact was observed in the recording images, a handful of pixels were systematically being detected at the very end of the scanning lines. Such artefacts were manageable at the previously used scan rate (2 ms), but at higher rates an important portion of the recording image had to be truncated during the image pre-processing. Consequently, there was a trade-off between frame rate (scan rate x number of row pixels) and the image resolution. Since we were using the GECI GCaMP6 we needed to keep a sufficiently high frame rate to follow calcium transient evolution in the responding synaptic terminals. Here, we aimed for a frame rate of 15 Hz, which correspond to an image resolution of 32*64. Such resolution was not optimal to identified structures and place ROIs. Thus, optimising the stimulation timing would lead to an increase of recorded image resolution. Moreover, increasing the scanning rate would allow the use of faster fluorescent biomarkers, like the glutamate sensor iGluSnFR.

Additionally, traditional microcontrollers, like the ATMega328, possess a short flash memory (32 kB), making it impossible to upload long and/or complex stimulus sequences, therefore limiting the range of potential experimental protocol.

Finally, driving LED with PWM from a microcontroller resulted in modulating their voltage, which is not ideal for LED lifespan, especially for short-wavelength LEDs which tend to rapidly decay as they usually require higher power supply which leads to higher thermal runaway. As a result, stimulation LEDs required regular recalibration if not replacement, which was not ideal for experimental consistency.

Facing all these issues, we developed a versatile LED stimulator designed to be used in combination with any two-photon microscopes. Built around an ESP32 microcontroller and a TLC5947 LED driver, the device offered new horizon for experimental protocols (Zimmermann et al. 2020).

3.4 – Hardware description

Precise temporal separation between light stimulation and fluorescence recording is paramount for efficient recording. High-efficiency LEDs, unlike conventional light sources, near instantly illuminate at full intensity when current is applied. They emit narrow-spectrum light and can be switched on and off within nanoseconds while

providing high emission stability (Hohman 2007). They are perfect candidates to be controlled to interweave the laser excitation timing with the light illumination: By turning off the LEDs during the laser scanning period and turning them on during the mirror retrace period, a clean separation between stimulation and emission lights can be achieved while nevertheless delivering sufficient average light to stimulate the photoreceptors (Fig 3.2b).

To interweave the light stimulation with the imaging system, we exploited a 5V digital signal which most conventional two-photon systems use to synchronously run their fast scanning mirrors through their digital acquisition (DAQ) system. This signal was also used here to synchronise a Pockels' cell for rapid regulation of laser power during the retrace period of a raster scan to avoid phototoxicity (Icha et al. 2017). The two-photon system is detailed in Fig 3.2c. On this schematic, the digital signal, here dubbed "*blanking signal"* was additionally integrated by the stimulator system for synchronising the stimulation LEDs.

To integrate the *blanking signal* and drive the LEDs in a finely time-efficient manner, it was decided to use the recently released (sept. 2016) ESP32 micro-controller (Adafruit ESP32 feather, built around the ESP32 system on a chip, Espressif). Compared to traditional microcontroller (i.e. Arduino Nano, ATMega328), it operates at 240 MHz (16 MHz for the Arduino Nano), which provided sufficient processing power to control the light output in the kHz range. It also possesses a 520 kB flash memory (32 kB for the Arduino Nano) allowing the storage and uploading of several complex stimulation sequences.

During the stimulator development, the ESP32 was coupled to an LED driver (Adafruit TLC5947, built around the TLC5947 chip, Texas instruments), a constant current-sink driver with the ability to linearly drive up to 24 LEDs. The use of such driver therefore did not require further gamma correction from the experimenter to correct the sigmoidal intensity dependency observed when directly controlled by a micro-controller (current modulation vs voltage modulation) (Fig 3.2d,e). Furthermore, the use of a dedicated constant current LED driver tended to improve LED stability over time as well as its life span. Such a driver ensured that the current drawn by the LED did not lead to thermal runaway which can cause irreversible damage. Additionally, this driver can be controlled through Serial Peripheral Interface (SPI) with 12 bits resolution (4,096 "grey levels", compared to 8 bits: 256 grey levels).

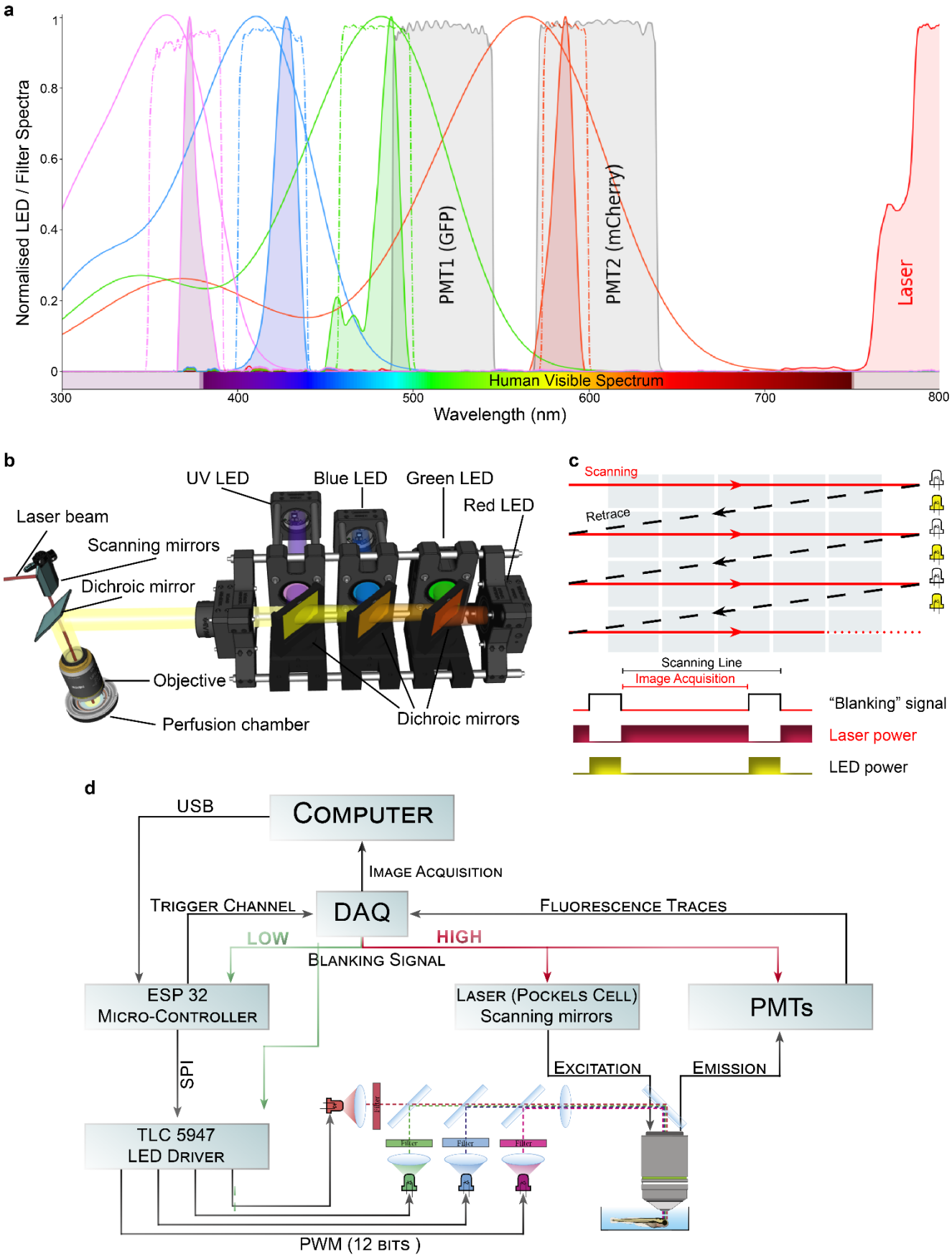

Figure 3.2 | Tetrachromatic stimulator system and spectral requirements. a) Spectral sensitivity curves of the tetrachromatic zebrafish opsins plotted along stimulation LEDs emission spectra and PMT detection bands for GFP and mCherry. In this experimental setup, one can see that spectral

separation is barely efficient between the green LED and PMT1, while the red LED is completely overlapping the second fluorescence channel. **b)** Rendering of the stimulator and the two-photon optical system. **c)** Illustration of the raster scan method described. The “blanking signal” is synchronous with the scanning logic, enabling the LEDs during the scanning mirrors retrace (black) and shutting them off during the acquisition (red), therefore providing temporal separation between stimulation and detection (schematic in (c) inspired from (Euler, Franke, and Baden 2019). **d)** Overview of the setup described for the visual stimulation experiment performed on the tetrachromatic zebrafish.

This new depth resolution was adequate for reaching the desired intensity modulation. Lastly, the TLC5947 possesses a *blanking input* which allowed immediate and simultaneous switching of all LEDs by forcing all constant current outputs to be forced off without the need to priorly be computed by the microcontroller. The *blanking signal* is thus used here as well to precisely switch off the stimulation lights and avoid any light artefact.

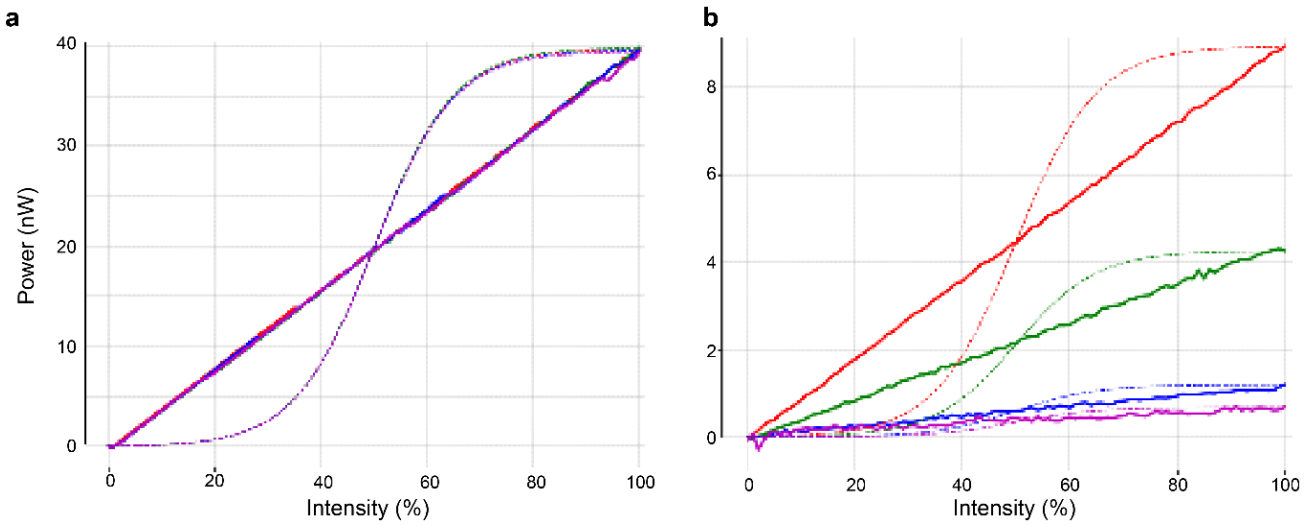

Figure 3.3 | Stimulator LED performances. a) Power recording of the LED systems previously described for zebrafish retina experiments, using the TLC5947 (solid lines) and their expected brightness with a classical current voltage system (dashed lines). Here all LEDs have been set up to the same power (40nW). **e.** Same as **b)** but with LEDs set up at natural statistics intensities. Here the linearity of the LED intensity output remains constant.

The remaining parts of the stimulator were made of off-the-shelf components and mounted on a customed-built printed circuit board (PCB) (Fig 3.4b).

The new stimulator was then coupled to our two-photon system and its performances tested. First, we verified the precise blanking of the LEDs by measuring with an oscilloscope the signal going to an LED positive pole and compared it to the periodic *blanking signal* that forced the LEDs current off (Fig 3.4c). When the *blanking* input was LOW, all constant current outputs were turned off without delay. All constant current outputs were controlled by the TLC5947 grayscale PWM timing controller which was reset during the blanking, thus providing a stable and instantaneous light output when the *blanking* signal went back to HIGH. This precise blanking of the LEDs during the scan retrace granted the generation of artefact-free images, even at high scanning rates (1 kHz in Fig 3.4c). Previously, light artefacts were detected for a handful of pixels for each scanning line which needed to be excluded while pre-processing the data, which in turn resulted in a consistent loss of imaging information. Such effect was the result of suboptimal synchronisation between previous blanking systems and the scanning mirrors which could not efficiently control the stimulation light offset at the end of the scan retrace. This effect was even stronger at higher scanning rate where ~20% of each frame needed to be discarded. Allowing faster scanning imaging without generating any light artefact was not insignificant as it multiplied by 4 the recording resolution: To obtain a 15 Hz frame with a 2 ms scan rate we previously had to use a 32*64 resolution. Now for an identical frame rate but with a scanning speed of 1 ms, a 64*128 pixels resolution can be used. It was then expected to better identify BC terminals with such resolution.

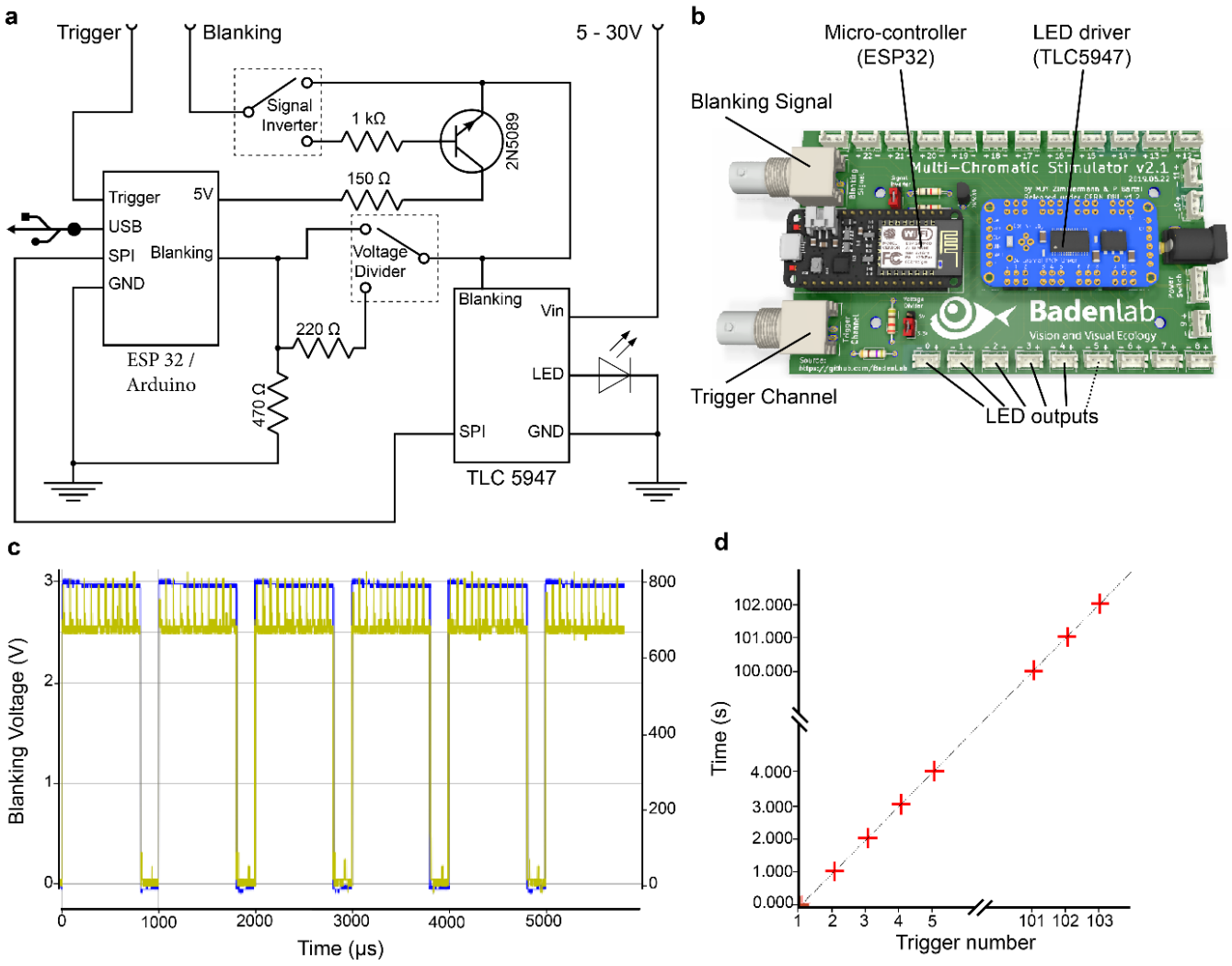

Figure 3.4 | Hardware design and temporal performance: a) Schematics illustrating the circuit that controls the LED output. The blanking input can be inverted by a switch before reaching the *output enable* pin on the LED driver (electronically switching off the LEDs) and sending the signal to the micro-controller. A second switch control the blanking signal voltage as it needs to be adapted depending on the logic of the microcontroller used (3.3V for ESP32, 5V for Arduino). The microcontroller controls the LED driver through an SPI connection and send trigger signal output to an external device. **b)** Rendering of the custom-printed circuit board which accommodate the microcontroller, the LED driver and up to 24 LED channels. **c)** Oscilloscope reading of the blanking signal (blue) efficiently switching off an LED (yellow). The blanking is operated here without noticeable delay. **d)** Trigger timing recorded by the DAQ highlighting its accuracy over time with a precision of 0.1µs. **t(n+1) = t(n) + T**, where "t" is the recorded trigger time and "T" the trigger period.

For analysis purposes, a trigger signal linked to the stimulus sequence was generated by the micro-controller. It sent a 3.3V signal pulse at the beginning of the stimulation, then repeatedly sent a signal every second. The trigger signal was then reconstructed and correlated to the recorded fluorescence traces. To verify the

stimulus timing precision, we plotted trigger signals detected by the DAQ alongside their timing occurrence and obtained a perfect linear correlation with a sum of squares due to errors (SSE) of 0.0 ms which highlighted the high accuracy of the system (Fig 3.4d).

Regarding the accuracy of the light intensity delivered by the stimulator, Fig 3.3 a&b show a perfect linearity of the light brightness with PWM. Thus, the ESP32 had so far answered to all our previous encountered issues and limitations. To test the limit of the micro-controller processor, we used standard C++ programming functions to measure how fast our code was being executed. We obtained a value of 22 µs (not shown here) to complete all calculations, integrate input signals, drive the TLC5947 to synchronously control the LED currents and send a timely-precise trigger signal. This value is way below the timing delay required by our recording system (~400 µs), meaning that this stimulator could be used for even faster scanning systems (resonant scans).

3.5 – An open source design

With the advancement of micro-controllers and LED technologies, and their availability on the global market, researchers can conceive and reproduce experimental designs that fit their specific needs (A. Powell 2012), overcoming their protocol limitation for fraction of the cost a commercial company would quote for (Pearce 2013). When commercial systems become too expensive or do not provide the required performance, open source hardware offers cost-effective solutions that have the potential to go beyond and above commercial technical limitations. The rise of the maker movement and the essentiality of open source hardware in science (Maia Chagas 2018; Pearce 2012; Friesike and Schildhauer 2015) is driving the development of experimental designs that can easily be found on open source repositories (Baden et al. 2015), adapted, upgraded and reproduced by users (A. B. Powell 2015; Bonvoisin et al. 2017).

Following the open source hardware philosophy, we made our stimulator design open source, we shared all data and documentation on freely accessible repositories (https://osf.io/ks8j7/, https://github.com/BadenLab/LED-Zappelin), and we submitted our work to an open access journal promoting open source designs for scientific research. We then further developed our stimulator to be adaptable to any two-photon microscopy setup that requires stimulation light which may overlap with fluorescence detecting bands. This is particularly interesting for visual

neuroscience studies working on different animal models, with therefore different photoreceptor spectral sensitivities, and for those looking for a standardised yet flexible approach. The device is highly flexible, as it allows the simultaneous control of up to 24 LED channels, allowing the use of various chromatic light stimuli. Our two-photon system runs on dual axis galvanometer scanning system with a current maximum scan rate of 1 KHz. However, as seen previously, the ESP32 high processing power allows the stimulator to be coupled with faster systems like galvo-resonant scanners.

The choice of an ESP32 as central processing unit was not only due to its processing power though. Like many popular micro-controller, it is compatible with the Arduino IDE interface, which is open source and intuitive but it is also compatible with, amongst others, MicroPython, a software implementation of Python3, written in C and optimised to run on micro-controllers. Python programming language being currently widely adopted by the neuroscience community, it is hoped that our stimulator could be further updated. Also, the development board used here as micro-controller (Adafruit Huzzah32 – ESP32 Feather) was as well chosen for further potential upgrades. There are many existing libraries for extension projects supported by the backing of companies such as SparkFun™ or Adafruit™, which would make it even easier for other people to extend this project, using their add-on boards on the one we developed.

3.6 – Bipolar cell response to natural statistics stimulation

With the new stimulator implemented on our two-photon microscope setup, it was then possible to stimulate zebrafish retinae with a “natural white noise”. Fundamentally, the previous protocol was performed only with LED light intensities set to the calculated natural statistics (Fig 3.5a). It was expected that BCs will maximally respond to this new set of stimuli and that more chromatic profiles could be determined, notably in the *strike zone* with a non-saturated UV light.

Although, preliminary results tended to show chromatic profile differences between BC responses under equal power and “natural statistics” power, most reverse correlation on these BCs fluorescence traces failed to generate temporo-chromatic kernels (Fig 3.5b). In the *strike zone* however, notable differences could be observed with a UV(Blue) predominance profile under equal intensities condition that substantially gave rise to longer-wavelength profile when the Blue and UV LED were tuned down to match the natural statistics. This is even more clear with the

third example trace below, where a BC terminal previously displaying a UV-monochromatic profile then presented a complex opponency profile which was only reported so far in the dorsal region of the retina.

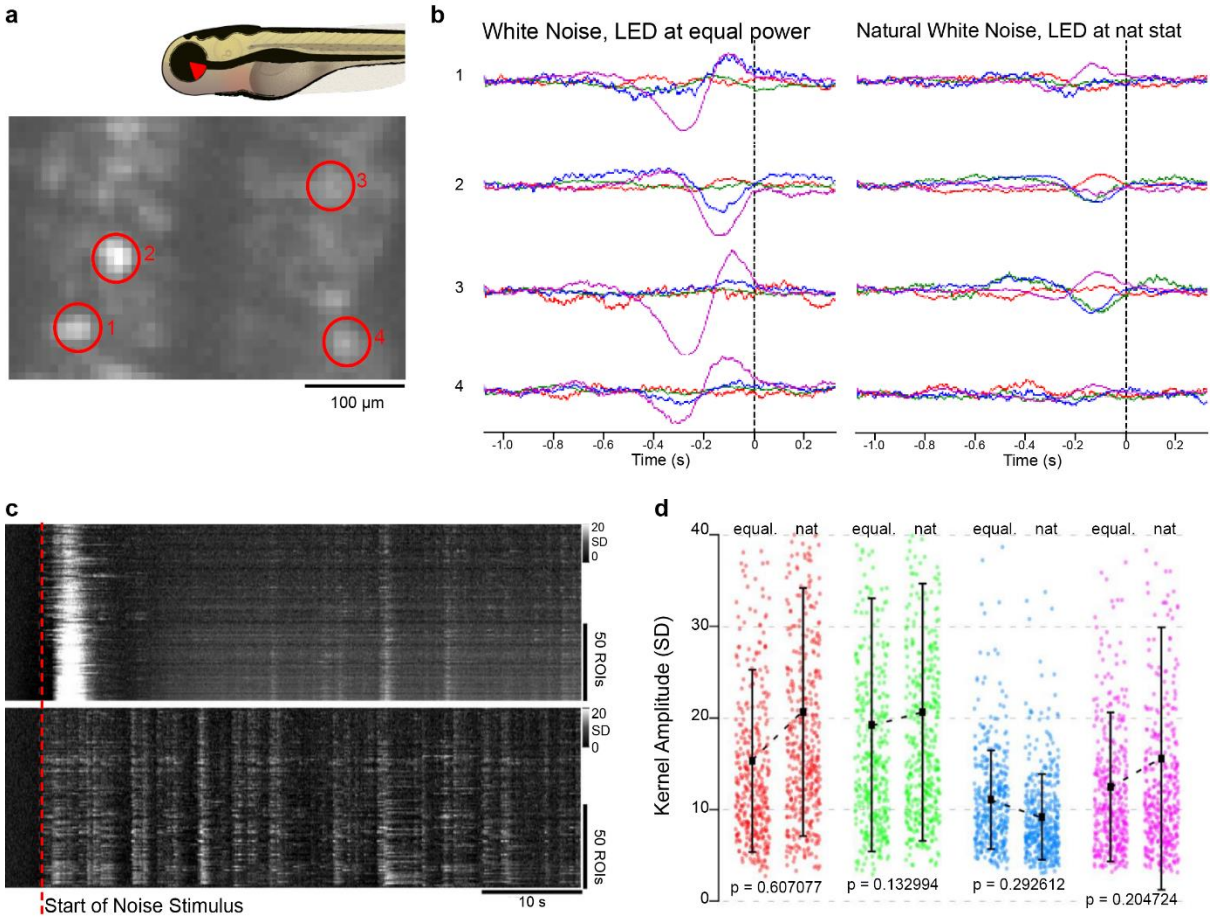

Figure 3.5 | Natural statistics stimulation. a) Two-Photon scan field of *Tg(RibeyeA:SyGCaMP6f)* larval fish IPL in the *strike zone* region with manually selected ROIs. **b)** Temporo-chromatic kernels extracted from these ROIs either stimulated by a white noise sequence with LED intensities equally calibrated or set to natural statistics. **c)** Heatmap of ROIs calcium traces over time. **d)** Mean of distribution of the resulting kernels. Median of equal and nat stat power compared through Wilcoxon-Mann-Whitney test. Figures c) and d) adapted from Zhou et al. 2020. *Statistical tests performed by T. Baden for publication* Zhou et al. 2020.

Overall, UV saturation potentially suppress complex chromatic computation within the *strike zone*, but larger dataset is required from the entire sagittal plan before concluding on the strength and homogeneity of such effect.

Still, the new stimulator and its “nat stat” calibration was used by fellow lab members on different retinal cells. It was used on RGC dendrites and somata from which an important population of UV-sensible ON-sustained neurons could be characterised in the *strike zone*, in adequation with our previous functional BC observation (Zhou et al. 2020). In this work they compared RGCs response to equal power and “nat stat” white noise stimulation (Fig 3.5c). From the same ROIs, a strong initial response could be observed in all cells under equal intensities, marking the specific UV-sensitivity of this region. The cells then displayed a prolonged period of response suppression. In contrast, these ROIs did not show a firm initial response, they did not adapt to the first light stimuli and overall responded more vigorously. However, the mean of the distributions of chromatic kernel amplitudes amongst those two light conditions were indistinguishable (Wilcoxon Rank Sum Test, 2 tailed), underlying the ability of the RGCs, once adapted, to process the chromatic signal in this region despite being saturated by UV (Zhou et al. 2020).

3.7 – Silent substitution protocol

Opsin cross-activation were not considered in previous experiments. Stimulation LEDs were chosen to match the opsin peak absorbance spectra, although each LED activated the remaining opsins with lower intensities due to overlapping spectral sensitivity profiles of the four different opsins. This is particularly clear for shorter wavelength LEDs which activated all opsins at different levels. As we have seen, a clear processing distinction within the retina is made between achromatic light, long-wavelengths vs short-wavelengths, and UV light. And this distinction appeared to follow the chromatic light distribution in natural environments. However, if we had a clear picture on how the system processed these spectral inputs, it was not clear how each opsin participated to this computation. One solution would be to silence the expression of specific cone-type photoreceptors and assess the retina response to chromatic stimulation. This method can be costly to implement and would consume time to generate transgenic lines. It would necessitate the effective silencing of all individual cone types. Additionally, as our model was a larval form, any modification to the retinal development might have resulted in development deviations from the wild-type retinal circuitry. Another approach can be considered though, using our accurate stimulator: Silent substitution.

The concept can be traced back to Ishihara work at the beginning of last century (Ishihara 1906). Silent substitution is a spectral compensation technique which aims to selectively stimulate one type of photoreceptor while preventing the remaining one(s) to respond to the stimulus (Estévez and Spekreijse 1982). It relies on the principle of univariance which states that a photoreceptor can be excited by different combinations of wavelength and intensity and still generates similar light perception (Rushton 1972). As a cone-photoreceptor can yield a similar response to a low-intensity light near its spectra peak wavelength as to a high-intensity one away from it, a multiple cone system can produce a comparable output to two distinct spectra. These spectral pairs are called metamers.

If we consider photoreceptors response as one-dimensional scalars with two possible variables (wavelength and photon flux), then two distinct stimulation lights can be made to produce metamers by adapting their photon flux. Consequently, we could virtually isolate an opsin pigment.

As rods are not fully developed nor functional in the larval zebrafish (Branchek and Bremiller 1984; Bilotta, Saszik, and Sutherland 2001), we needed not concern ourselves with this type of photoreceptor interacting with the chromatic compensating stimulus.

The first task was then to estimate the photon flux each cone was receiving by all stimulation LEDs. To maximise the light modulation along the possible 12 bits PWM grayscales, the LEDs equal power configuration was set here. LEDs were calibrated using an optical energy powermeter (PM100D, ThorLabs, Germany) coupled to a photodiode power sensor (S130VC, ThorLabs, Germany) with a sensitivity ranging from 200 to 1000 nm. All LEDs were set to a 40nW power, which corresponds to an energy flux of $2.48*10^{11}$ $eV.s^{-1}$ ($1J = 6.242*10^{18}$ eV). The energy flux (P_{eFlux}) which determines the rate of energy transfer through a surface (here the cone outer-segment areas) is wavelength dependent and depends on the wavelength-dependent photon energy (Q) described by the Planck-Einstein relation:

$$Q_{(\lambda)} = \frac{c.h}{\lambda}$$

The photon flux Φ (in $photon.s^{-1}$) was next determined by:

$$\Phi_{(LED)} = \frac{PeFlux(LED)}{Q(\lambda)}$$

The photon flux density $Pe_{(\lambda)}$ (in $photon.s^{-1}.\mu^{-2}$) was then determined by:

$$Pe_{(\text{spectral channel})} = \frac{\Phi(\text{LED})}{\text{Sensor area}}$$

Where the sensor area is the photodiode sensor surface which diameter is 9.5 mm.

Spectral channel	Red	Green	Blue	UV
LED peak wavelength (nm)	587	487	427	372
$Q_{(LED)}$ (eV.photon^{-1})	2.11	2.55	2.90	3.33
Φ (photon.s^{-1})	7.45*10^{12}	7.59*10^{-12}	6.44*10^{-12}	4.18*10^{-4}
$Pe_{(LED)}$ (photon.s^{-1}.µm^{-2})	1.05*10^{5}	1.07*10^{5}	9.09*10^{4}	5.90*10^{4}

The photon flux R_{Ph} received by each cone outer segment depended on the efficiency of each cone to absorb a photon. This relationship was determined by:

$$R_{Ph(LED/Cone)} = Pe_{(LED)} . A_{Collect\ (cone)}$$

Where $A_{Collect}$ is the specific light collection area of cone outer-segments, determined itself as follow:

$$A_{Collect\ (cone)} = OSA . \gamma . (1 - 10^{\alpha . OSL})$$

Where OSA is the cone outer-segment area (in µm^2) (Allison et al. 2004), γ the quantum efficiency of the opsin change (Dartnall 1968), α the cone specific absorbance coefficient (in µm^{-1}) (Allison et al. 2004), and OSL the cone outer-segment length (in µm) (Branchek and Bremiller 1984). The term $1 - 10^{\alpha . OSL}$ corresponds to the specific absorption coefficient. It is also known as the Specific Optical Density (SOD) and defines the fraction of light absorbed per infinitesimal unit of photopigment length. It only depends on the absorption properties of the photopigment.

Colour channel	Red	Green	Blue	UV
OSA (µm^2)	2.4	2.4	2.8	2.6
γ	0.67	0.67	0.67	0.67
α (µm^{-1})	0.0073	0.0063	0.007	0.0054
OSL (µm)	10	10	7.6	10
SOD	0.1547	0.1350	0.1153	0.1169
$A_{Collect\ (cone)}$ (µm^2)	0.47	0.41	0.48	0.42

The photon flux R_{Ph} of each LED being absorbed by each cone photoreceptor opsin could now been estimated. Here all LEDs were equally calibrated at the same intensity, R_{Ph} are therefore at the same order of magnitude (Fig 3.6).

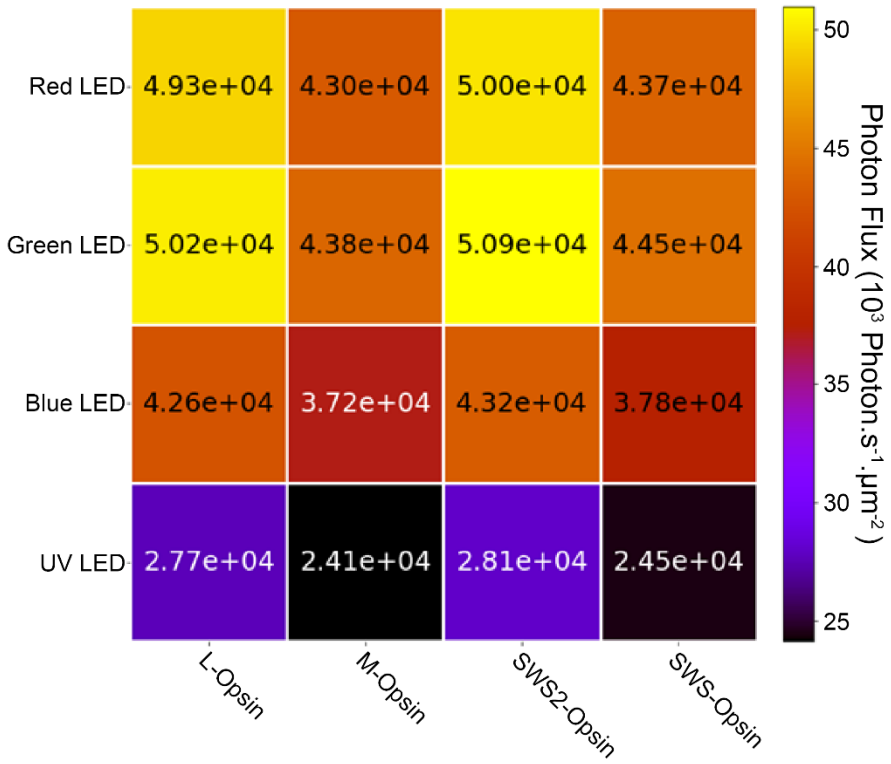

Figure 3.6 | Stimulator photon flux. Table compiling the photon flux of each LED triggering photo-isomerisation on each cone expressed in photon per second.

Lastly, we needed to consider the opsin cross-activation by the tetrachromatic light in order to appreciate the effective activation S_{Act} of each opsin by each LED. This is obtained by measuring the integral of the normalised LED spectra by opsin absorbance spectra, divided by the normalised LED spectra integral (Fig 3.7a):

$$Sact\ (Cone, \lambda) = \frac{\sum(\mathrm{Opsin(cone)} * \mathrm{LED}(\lambda))}{\sum(\mathrm{LED}(\lambda))}$$

LED spectra were obtained by a CCD spectrometer (CCS 200/M, Thorlabs, Germany) ranging from 200 to 1000 nm. Graphical representation of the LED measurements were previously presented in Fig 3.2a. Opsin sensitivity were

established using the Govardovskii template (Victor I. Govardovskii et al. 2000), itself adapted from the popular template described by (T. D. Lamb 1995) which described visual opsin sensitivity template based on one single variable, the opsin peak wavelength λ_{max} (Fig 3.7b). The Govardovskii opsin template for the zebrafish visual system has been verified by the generation of the cone action spectra through electrophysiology experiments (Endeman, Klaassen, and Kamermans 2013). Opsin alpha and beta bands were defined by:

$$S\alpha(x) = \frac{1}{e^{(A*(\alpha-x)} + e^{(B*(\beta-x)} + e^{(C*(\gamma-x)} + D}$$

$$S\beta(\lambda) = A\beta * e^{-\left(\frac{\lambda-\lambda m\beta}{B\beta}\right)^2}$$

Where:

$x = \lambda_{max} / \lambda$

α a variable based on the peak wavelength λ_{max}

A, B, β, C, γ, D constant parameters

Aβ the beta band amplitude (0.26 times the alpha band amplitude)

λmβ the position of the beta band peak (depending on λ_{max})

and Bβ a bandwidth parameter determined by λ_{max}

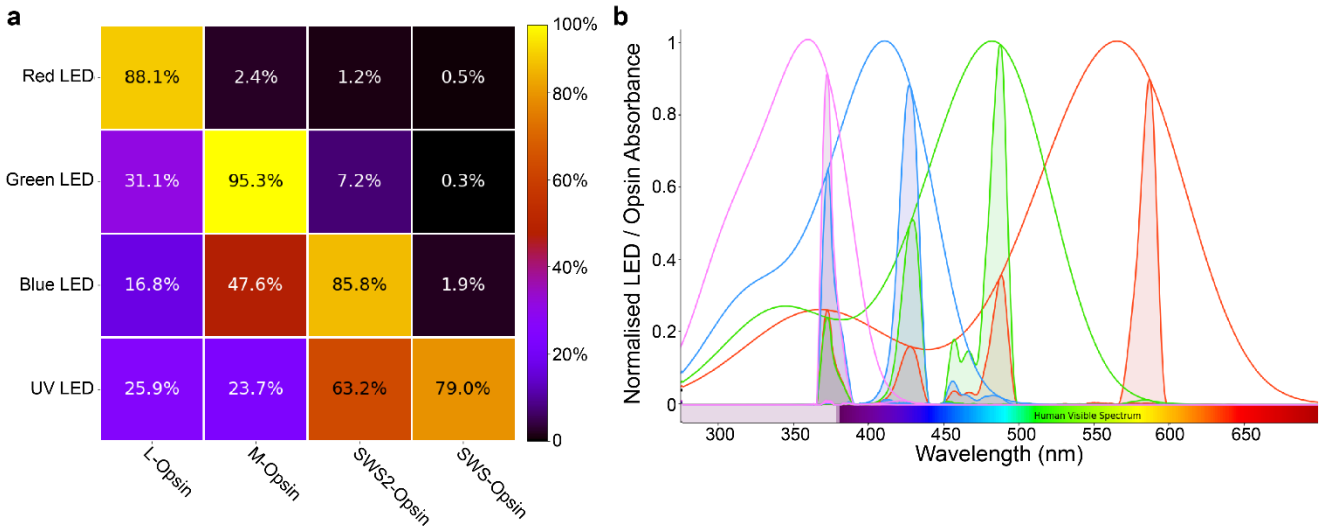

Figure 3.7 | LED relative co-excitation. a) Matrix representing the relative excitation of each LED onto each cone. **b)** Graphical representation of **a)**.

Now the maximum photo-isomerisation rates R_{Iso} (photon.s^{-1}.photoreceptor^{-1}) could be estimated for each combination of LED and cone photoreceptor. These values determined the light intensities necessary to trigger opsin isomerisation to each cone type (Fig 3.8a). From there one could modulate LED intensities to achieve the virtual silencing of one cone opsin of interest

$$Riso(Cone, \lambda) = \sum Rph(Cone, \lambda) * Sact(Cone, \lambda)$$

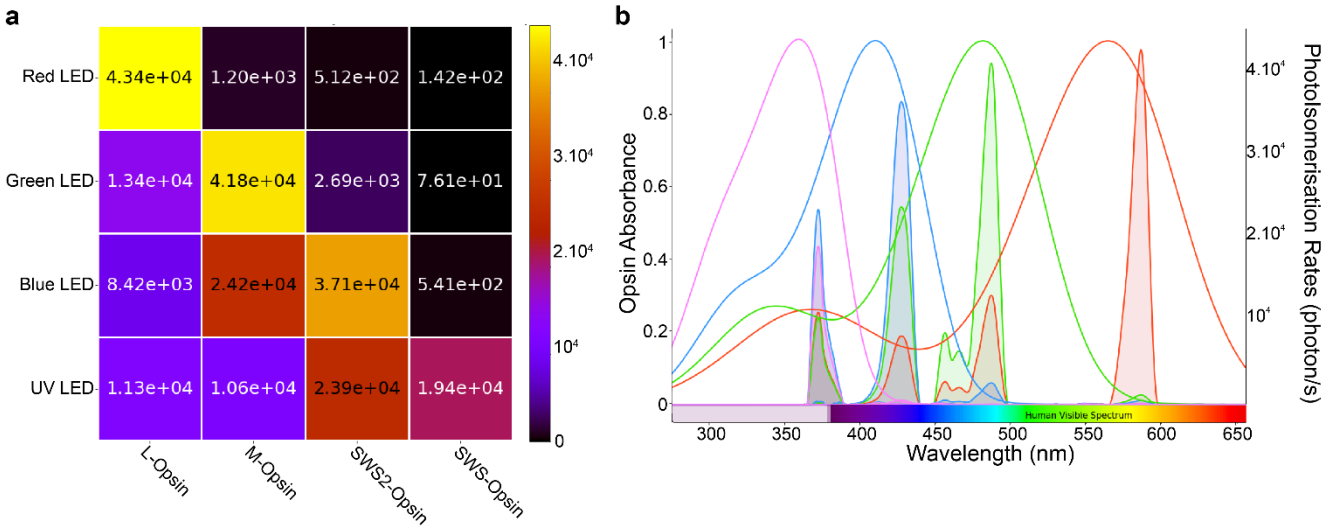

Figure 3.8 | Maximal photo-isomerisation rates. a) Matrix representing the maximal photo-isomerisation rate for each LED on each opsin expressed in photon.s^{-1} **b)** Graphical representation of **a)**.

Now that the photon flux necessary to trigger photo-isomerisation was determined, we could follow up with the silent substitution protocol where one type of photoreceptor is selectively stimulated by presenting a steady excitation to all other photoreceptor types using a counteracting stimulus, henceforth virtually silencing their pigment. First, it was required to write in matrix notation the linear relations between the stimuli r, g, b and uv and the total quantum catch produced in each of the cone pigments $S_{Cone/LED}$. Such equation can be abbreviated as follow:

$$(S) = (M) * (C)$$

Where, S is the effective cone stimulation, M the transform matrix and c the colour mixture columns vector representing the relative LED power. By modulating the

LED lights values (ΔC), one could adequately modified S values in the above system such as:

$$(\Delta S) = (M) * (\Delta C)$$

The M matrix corresponded to the maximal photo-isomerisation rate matrix defined earlier, but with a photon flux density of 1 photon.s^{-1}.μm^{-2}.

$$M = R_{Ph(1\ photon\ \lambda)} * S_{Act}$$

Where $R_{Ph(1\ photon\ \lambda)}$ is the photon flux density for one photon at LED specific wavelength, and S_{Act} the specific opsin activation which corresponds to the relative co-excitation matrix developed earlier.

$$R_{Ph(1\ photon\ \lambda)} = Pe_{(1\ photon\ \lambda)} . A_{Collect\ (cone)}$$

$$S_{Act} = S_{Opsin} * S_{LED}$$

Colour channel	L-Opsin	M-Opsin	S-Opsin	UV-Opsin
1 Photon Flux (photon.$s^{-1}\mu m^{-2}$)	0.469	0.409	0.476	0.416

By noting N, the inverse matrix of M, the LED vector matrix can be expressed as:

$(\Delta C) = (N) * (\Delta S)$

Finally, a normalised silent substitution stimulus could be generated: To model the stimulation counterweights, the opsin of interested is to be stimulated by its corresponding LED with an intensity varying along a sigmoid function over time. For example, to isolate the long wavelength sensitive opsin, the green and UV LED intensities must adopt a scaled inverted sine profiles while the blue LED remains at a constant light level (Fig 3.10a). As this opsin sits on the spectral sensitivity edge, it would not be particularly complicated to stimulate it independently. One could for example have chosen a stimulation LED with a longer emission wavelength, which in this case would have eased the protocol (Fig 3.10b).

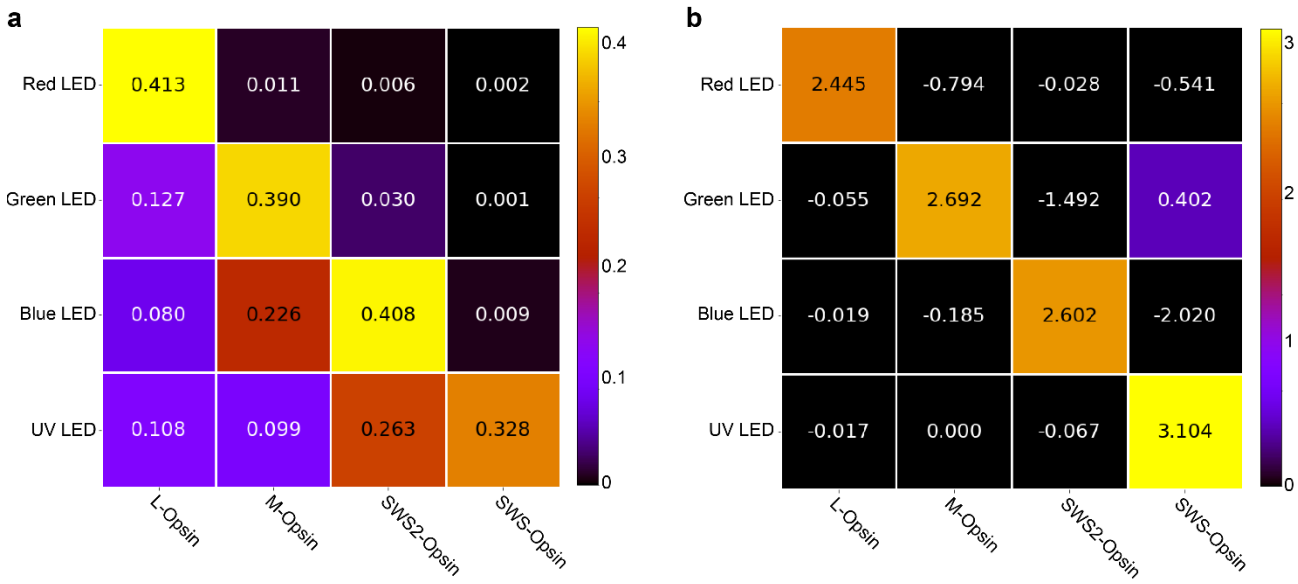

Figure 3.9 | Spectral sensitivity transform matrix. a) M matrix as described in (Estévez and Spekreijse 1982), without unit. **b)** N matrix, invert of M matrix

For the remaining opsins however, the task might prove to be more difficult. The opsin sensitivity curves overlapped to such extent that isolating a cone might only be possible through a very small fluctuation of light. For example, isolating the M opsin (Fig 3.11a) required subtracting the blue LED light from the system when the green LED reached its maximum intensity (Fig 3.11b). This implied that all LEDs must start their stimulation sequence at a non-zero value, therefore reducing the intensity range by which they can be modulated. This issue was even more striking for the blue and UV-opsin (Fig 3.12 & 3.13) due to their close absorbance spectra overlapping and the presence of the red and green opsin beta bands.

It would be noted here that, as we work on animals *in vivo,* these calculations (and the stimulation model resulting from it) did not take into consideration the optical effects of the cornea and lens on the stimulation light reaching the retina, nor the tiny amount of water/agar it has to go through before hitting it.

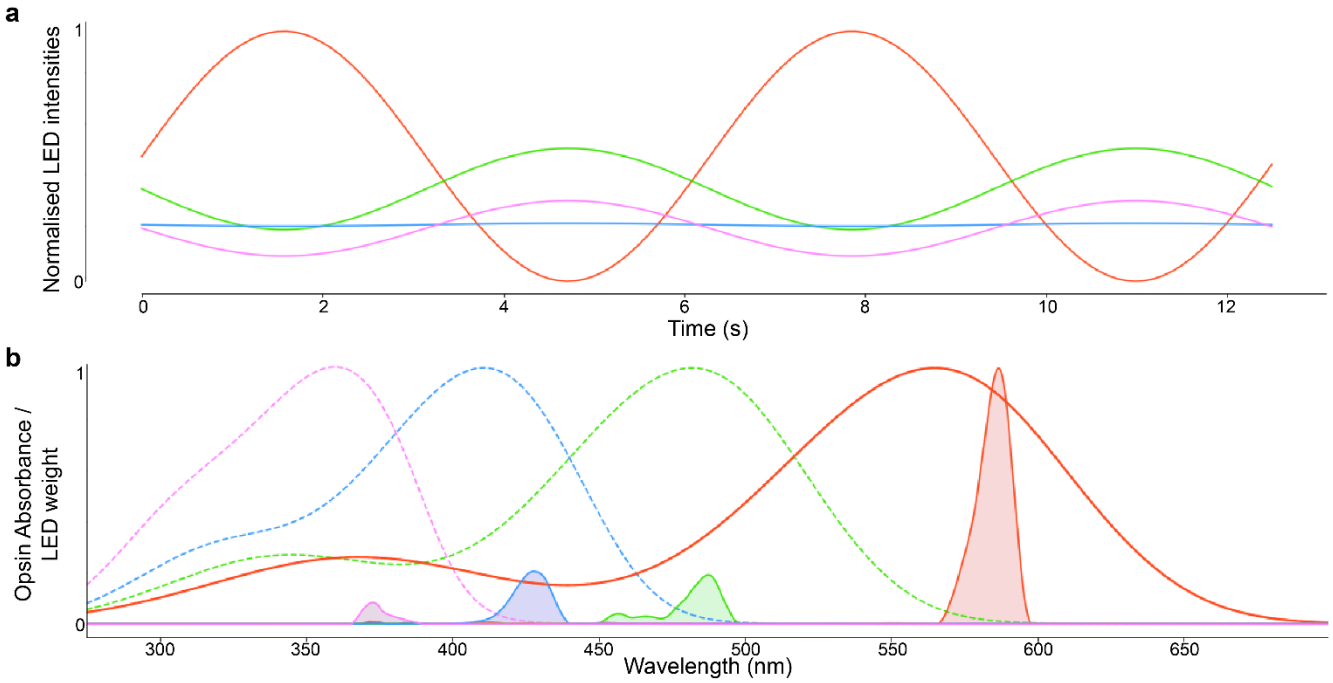

Figure 3.10 | L-Opsin Isolation. a) Representation of normalised LEDs values to be applied to the tetrachromatic system for red-cone isolation**. b)** Graphical representation of LEDs intensity counterweights when the red LED is at its maximum

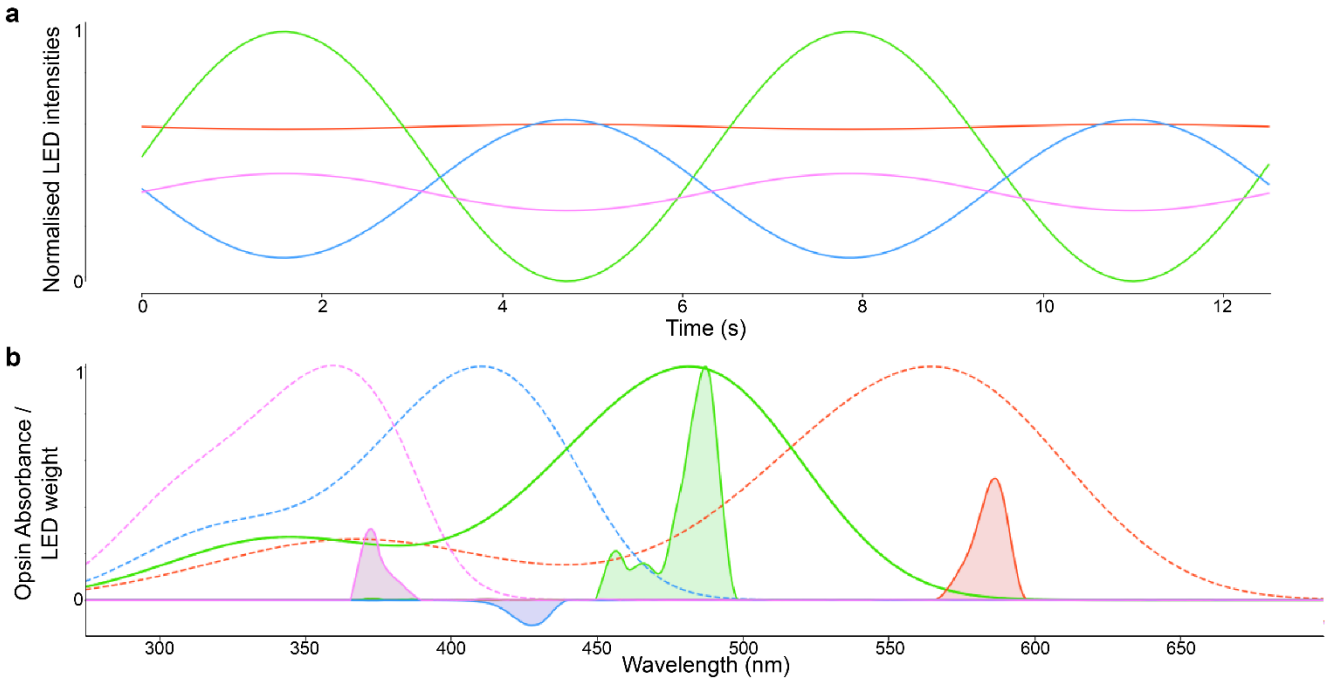

Figure 3.11 | M-Opsin Isolation. identical to Fig 3.10 but for the medium wavelength sensitive opsin and green LED

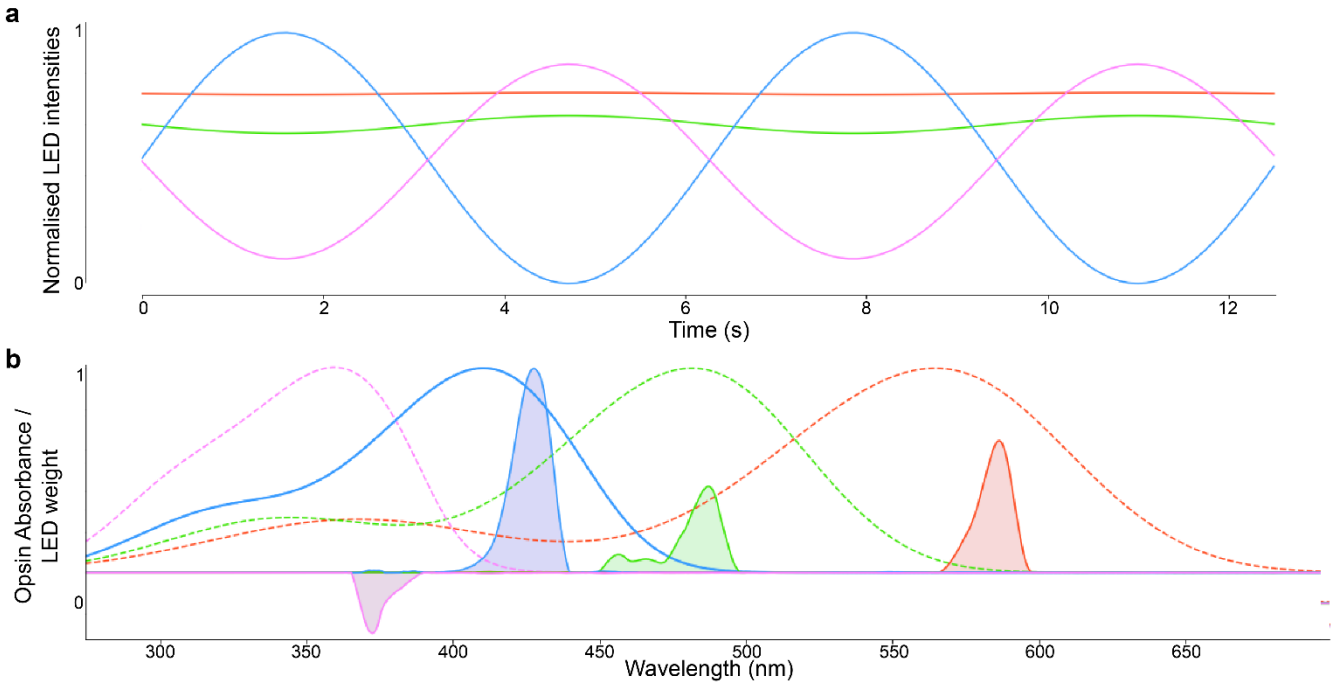

Figure 3.12 | S-Opsin Isolation. identical to Fig 3.10 but for the short wavelength sensitive opsin (SWS2) and blue LED.

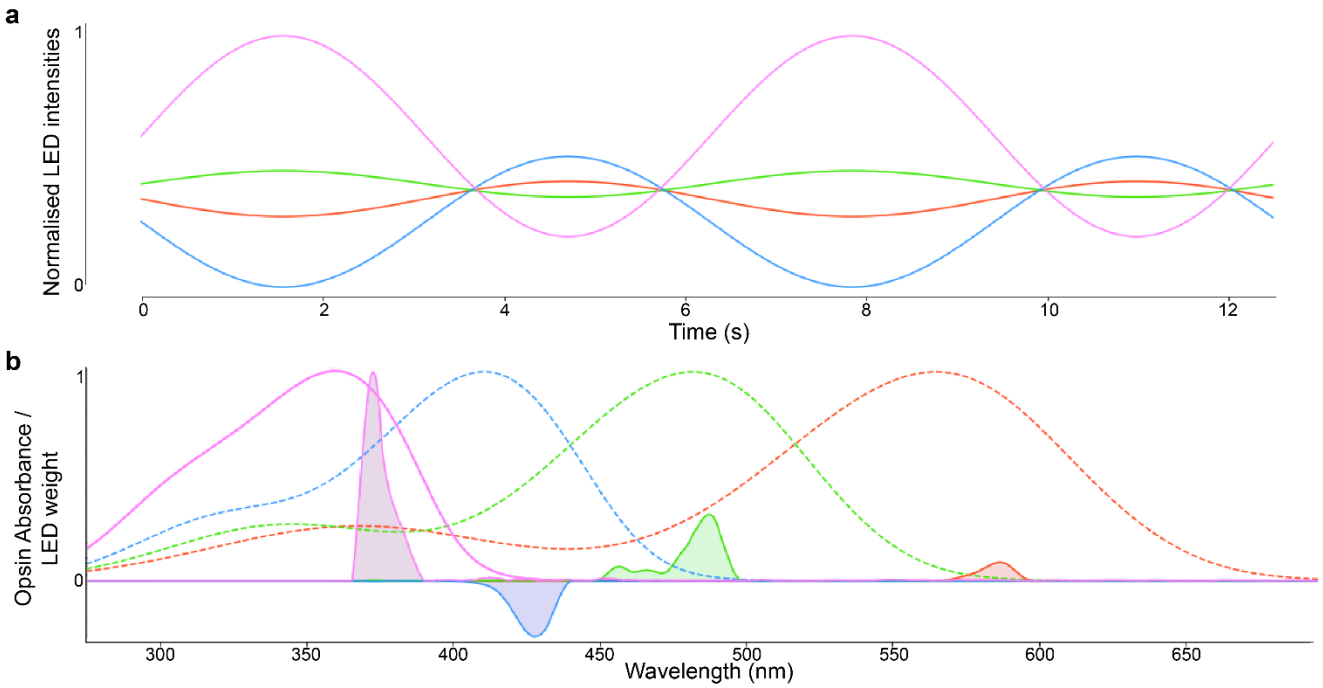

Figure 3.13 | UV-Opsin Isolation. identical to Fig 3.10 but for the UV sensitive opsin (SWS) and UV LED

.

3.8 – Application in other fields of neuroscience

Being open source, our stimulator device can easily be reproduced and adapted to any experimental setup where two-photon imaging necessitates coupling with light stimulation. The last decade has seen an explosion of optogenetics tools and techniques, especially with the continuous development of optogenetics actuators. It then became evident that versatile and easy to use LED-based stimulator devices had to be developed alongside.

As we do not use optogenetics ourselves, we adapted our stimulator in collaboration with the Prieto-Godino lab from the Francis Crick Institute in London, so it can be used on their two-photon system for optogenetics experiments.

Our two-photon system was controlled by the open source, IGOR-based, imaging software “ScanM” (developed by W. Denk, M. Müller and T. Euler) which provided a HIGH digital signal during the *blanking* period which was in turn fed to the stimulator as detailed precedently. In comparison, their system was controlled by the popular MatLab-based software package ScanImage (Pologruto, Sabatini, and Svoboda 2003), which instead provided a LOW signal during the retrace. We therefore incorporated to our custom-built PCB a logical NOT gate that acts as a signal inverter and which can be enabled by a simple 2-pin jumper on the PCB (Fig 3.14a). This further addition contributed to the device versatility.

With the stimulator properly interfaced to this new system, its efficiency was tested to drive optogenetic actuators expressed in the *Drosophila* dorsal organs while recording brain-wide calcium signals under two-photon. The red-shifted channel rhodopsin CsChrimson (Klapoetke et al. 2014) was expressed in olfactory sensory neurons, and the GECI GCaMP6s pan-neuronally expressed (elav-Gal4;UAS-GCaMP6s / LexAOp-CsChrimson;Orco-LexA). Dissected larval heads with intact olfactory sensory organs (dorsal organs) and an exposed central brain (Fig 3.13b) were immobilised in 3% low-melting-point agarose in physiological saline (Prieto-Godino, Diegelmann, and Bate 2012) and placed under the microscope objective. Full field illumination steps of 615nm light were presented, lasting 0.5s with an inter-stimulus interval of either 3 s (Fig 3.13c) or 10 s (Fig 3.13d). We observed, as expected, robust stimulus-evoked activity in the primary olfactory sensory centres of the larval brain, the antennal lobes (AL, red outlines in Fig. 3.13c & d).

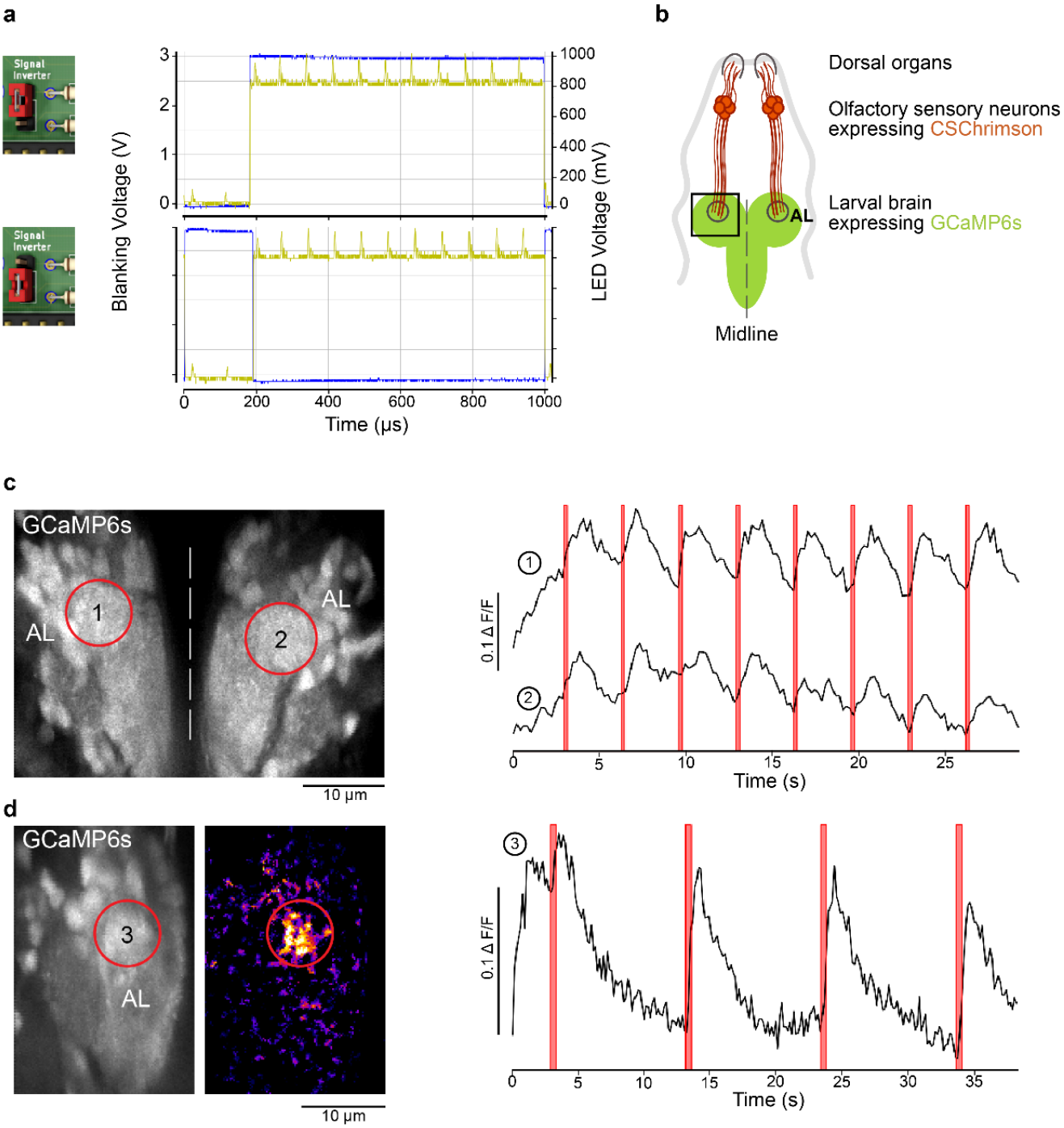

Figure 3.14 | Drosophila optogenetics experiment. **a.** Representation of the two possible stimulator configurations for the blanking signal input, with a *LOW* (top) and a *HIGH* (bottom) blanking signal input for an inverted and original signal input, respectively. As in fig 3.3, oscilloscope readings of the blanking signal (blue) efficiently switching off pulsating LED channel (yellow). **b.** Schematic of a fruit fly first instar larval head expressing the red-shifted channel rhodopsin CsChrimson in olfactory sensory neurons and GCaMP6s in pan-neuronally (image generated by the Prieto lab). **c-d.** Standard deviation projections of 2 photon scan fields of the larval brain with antennal lobes marked by red circles (left) and Ca^{2+} traces in response to red flashes (right). **c.** Stimulation duration = 0.5 s, inter-stimulus interval = 3 s, image dimensions = 256 x 230, scan rate (lines) = 1,081 Hz, frame rate = 4.7 Hz. d. Stimulation duration = 0.5 s, inter-stimulus interval = 10 s, image dimensions = 256 x 170, scan

rate (lines) = 1,077 Hz, frame rate = 6.34 Hz. Middle panel is a heatmap of pixel intensities showing high GCaMP6 fluorescence in the antennal lobe following optogenetic stimulation; obtained by subtracting a pre-stimulus from a during-stimulus image (median filter, kernel size = 2).

3.9 - Conclusion

The development of this chromatic stimulator offered the opportunity to expand the range of possible stimulation protocols for investigating the zebrafish visual system. By designing a custom-built stimulation system, an extensive and more flexible handle on visual stimuli generation was acquired, raising the possibility to explore new innovative experimental questions. Additionally, implementing zebrafish environment natural statistics allowed a deeper investigation on how this model's retinal circuits have evolved to optimally processed chromatic signals.

Still, more data from BC recording across the IPL are needed to estimate if the natural spectrum calibration enhances BC responses if not saturated anymore by UV light. Also, here retinae were stimulated with a binary tetrachromatic white noise (LEDs being sequentially turned on and off to their maximal values). This experimental protocol therefore did not directly assess any potential modulation effect of one spectral/cone channel onto another, nor permit the identification of detailed temporal chromatic contrast sensitivity. Nonetheless this new stimulator and the natural statistics calibration has been already used in a recently published work by fellow lab members (Zhou et al. 2020; Yoshimatsu et al. 2020), demonstrating the usefulness of the device.

The main feature of interest in this stimulator is the possibility to arbitrarily chose the number of light sources and their spectra. This simple feature opens the possibility to adapt this stimulator to any animal model spectral sensitivity. Non-mammalian colour vision research remains a comparatively small niche within the visual neuroscience field. Hopefully, the ease of access to low-cost and customisable stimulation devices such as this one, that can easily be coupled with any existing data collection systems (two-photon, electrophysiology, behavioural assays, etc.), will attract fellow researchers to further investigate this topic.

Furthermore, by making this project open source, by simplifying its conception and by sharing a detailed documentation (cf. Appendix 1), we aimed to incentivise an easy reproduction and use of our system (Maia Chagas 2018), in the desire to create a standardised and versatile chromatic stimulation system to compare data obtained from various labs working on distinct animal visual models, each with their

own spectral sensitivities. Also, the device was conceived to be adaptable to different programming platforms leaving room for improvement by other research teams.

To date, the fidelity as well as time/amplitude precision of stimulator has encountered no hard-experimental limitations for the study of animal vision, and its full range of possibilities may have not been reached just yet. However, it was designed for full field stimulation and does not allow the study of spatial contrasts. Thus, this stimulator while being a major improvement, does not fully comply to our future experimental needs which requires the addition of an extra dimension of space.

Chapter 4

Development of high-resolution stimulators for the study of colour vision across species

Designing open source spatio-chromatic devices with flexible wavelength light input for coupling with two-photon microscopy.

Of the colours with equal perfection, the one showing greater excellence will be the one seen in company of its direct opposite. Direct opposites are: The pale with the red, the black with the white, although neither of the latter two is a colour; blue and yellow as gold, green and red. Every colour is better recognised within its opposite than within its similar, like the dark in the light and the light in the dark. The white that borders with the black makes the black appear darker and the white brighter.

Leonardo da Vinci, De' Colori, Tratarro della Pittura (1503-1513)

In the following chapter I will detail the collaborative work carried out with the University of Tubingen to develop a spatio-chromatic stimulator, which was published as an opensource project in: **An arbitrary-spectrum spatial visual stimulator for vision research.** Franke K, Chagas AM, Zhao Z, Zimmermann MJY, Bartel P, Qiu Y, Szatko K, Baden T, Euler T.

4.1 – Introduction

Visual systems strongly rely on edge detection for object recognition (Hubel and Wiesel 1968), for example based on luminance contrast between two neighbouring objects. However, even if most edges combine luminance and chromatic contrast, independent isoluminant chromatic edges also exist in natural scene statistics (Hansen and Gegenfurtner 2009) which cannot be delineated with an achromatic detector. This, instead, requires a detector that combines spatial and spectral information. This concept then rapidly expands also into the temporal domain, effectively necessitating visual systems to combine information about luminance, spectral contrast, and time. Accordingly, visual systems must be probed with a stimulator that can deliver contrasts across all these dimensions.

To therefore explore BC spatio/temporo-chromatic contrasts, another stimulation system is needed. This will need to integrate all the stimulation criteria previously discussed in addition to offering spatial control that meets the larval zebrafish maximal as defined by receptor spacings.

Beyond exploring BC spatio-chromatic processing in general, this will also allow specifically testing the hypothesis that UV-sensitive BCs in the strike zone are also spatially tuned to support the detection of small UV-bright moving objects.

Here we introduce a fully developed spatial stimulator with high resolution and the capacity to integrate the four colour channels system previously described. However, due to time constraints for the stimulator development and calibration, only preliminary data is presented in the following section.

4.2 – Overcoming hardware limitations

As discussed in the previous chapter, studying the retinal circuits underlying colour vision in an animal model requires precise control over the displayed stimulus characteristics: Flexibility over the spectrum is necessary to adjust the stimulation light to the model's spectral sensitivity. Also, the stimuli's spatial resolution must be below the model's visual acuity and the frame rate higher than its visual flicker rate (Hecht and Verrijp 1933). Furthermore, if coupled with two-photon imaging the stimulation light must be synchronised with the data acquisition system (cf. Chapter 3).

Many options are commercially available to display high resolution images to visual systems with an appreciable frame rate (60 Hz). However, these devices are conceived for human vision (reviewed in (Surridge, Osorio, and Mundy 2003) and too often do not allow any modification of the light source. Even when reverse engineering is possible, these devices, made for trichromats, are built around three display panels (LCD, LCoS, DLP, etc.) which does not allow the addition of a fourth colour channel, thus limiting the experimental possibilities for studying tetrachromatic systems (Fig 4.1). Furthermore, their optics are not conceived for UV light and therefore absorb an important portion of this part of the spectrum while failing to correct any chromatic aberration. Consequently, such devices exclude from the experimentation scope any animal models depending on UV detection for an extended range of visual-guided behaviours.

Currently, there is no commercially available equipment which can be used as a spectrally appropriate spatio-chromatic stimulator for the study of most non-primate visual systems. Accordingly, most research groups individually develop their own visual stimulation devices based on equipment originally conceived and optimised for human vision. They usually adapt these to examine one specific research question for their animal model. The multiplication of locally designed stimulation devices complicates data interpretation transfer from one animal model to another, or indeed between labs.

As with the LED Zappelin' project, we aimed to conceive a relatively low-cost, open source equipment, which can be implemented on any visual system and which can be further upgraded and improved by fellow researchers in the effort to develop a common and standardised stimulator design for vision research. The main goal here, was to develop a highly flexible spatial stimulator which could cover a wide spectral sensitivity range and take up multiple distinct and arbitrary chromatic channels. Ideally the stimulator would take as many channels as the number of spectrally separable photoreceptor types in the studied animal (The popular *Drosophila* for example possesses six main visual opsins (Feuda et al. 2016) (Fig 4.1c)).

Here we developed a spatio-chromatic device built around Digital Light Processing (DLP) LightCrafters (LCr) E4500 MKII, developed by Texas Instrument and manufactured by EKB Technologies Ltd. These DLP projection systems are conceived around a Digital Micromirror Device (DMD), a micro-opto-electro-mechanical system (MOEMS) originally designed by Larry Hornbeck (Hornbeck

1996) (Fig 4.2a). DMDs are composed of arrays of microscopic mirrors, corresponding to individual pixels for the to-be-projected images, which can be rapidly rotated to deflect the incoming light onto a projecting lens, therefore creating a structed image (Fig 4.2b).

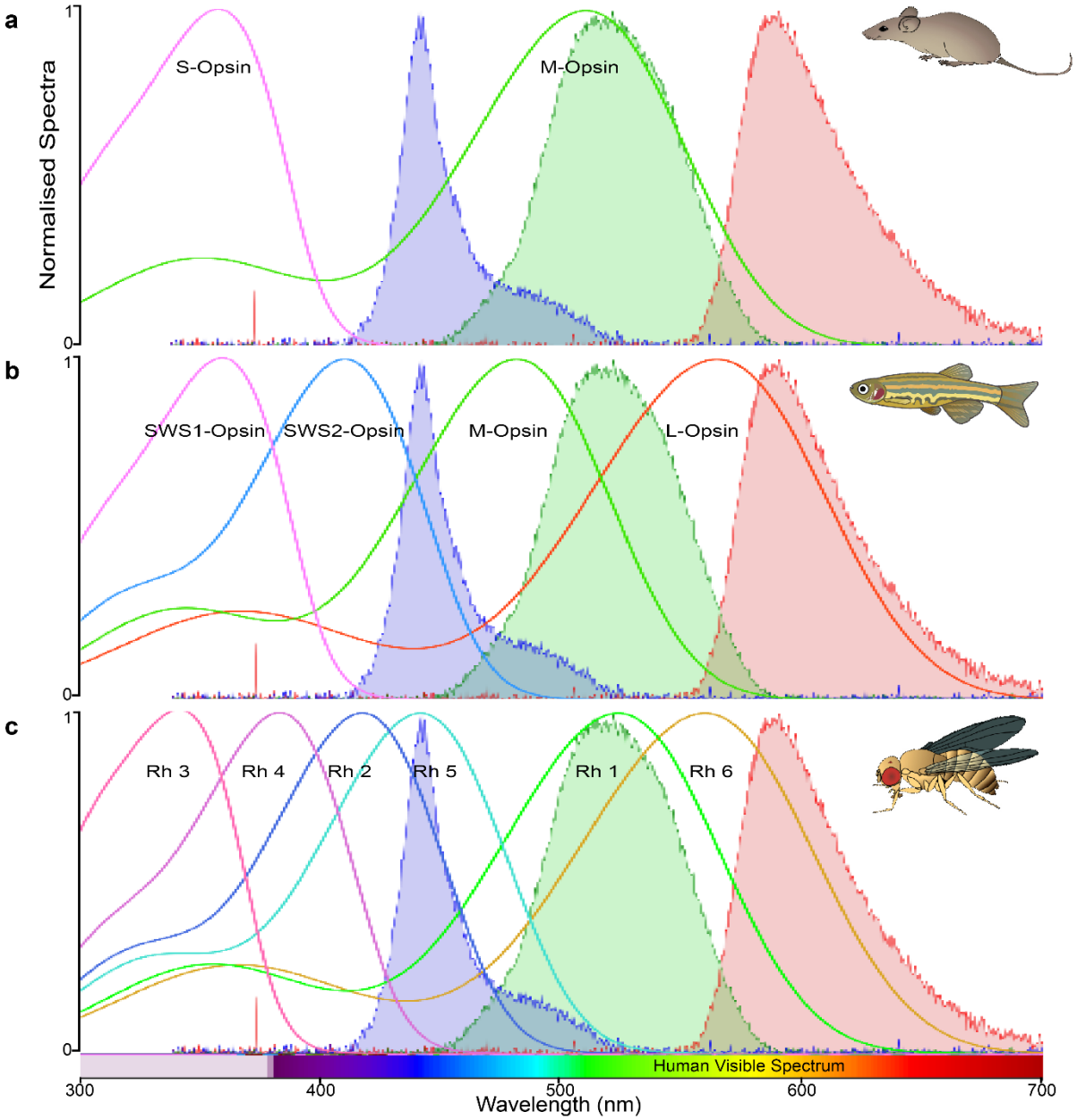

Figure 4.1 | Sensitivity profiles over standard TFT monitor spectra: a) Sensitivity profile of mouse S- (magenta) and M- opsins (green) over TFT LED spectra. **b)** Sensitivity profile of mouse SWS1- (magenta), SWS2- (blue) M- opsins (green) and L-opsin (red) over TFT LED spectra. **c)** Sensitivity profile of drosophila rhodopsins over TFT LED spectra (Rh7 not represented).

To generate colour images, the system displays R/G/B lights sequentially onto the DMD which adopts predefined patterns for each light input for each frame. Grayscales are achieved by rapidly toggling the mirrors along a time ratio defined by a binary PWM while the input light remains constantly on.

As the projection system does not depend on light input modulation, it is then possible to customise the illumination system to adapt it to the desired animal model spectral requirements. However, the DLP system was originally design for trichromat vision and its firmware therefore only modulates three colour channels (RGB), each with an 8-bit resolution. Reverse engineering would allow the integration of a fourth colour channel, nonetheless this option was readily excluded on account that: First, the aim of this work was to produce an open source project which, as detailed in the previous chapter, could be easily replicated by visual neuroscience groups without extensive knowledge on electronics nor programming, and ideally be integrated onto two-photon microscope systems. Secondly, the LCr digital video data run on 24-bit RGB (3*8). The addition of a fourth channel will decrease the grayscale resolution of each channel to only 6-bit (64 values), which can be inadequate considering the precise intensity control required for certain scientific questions.

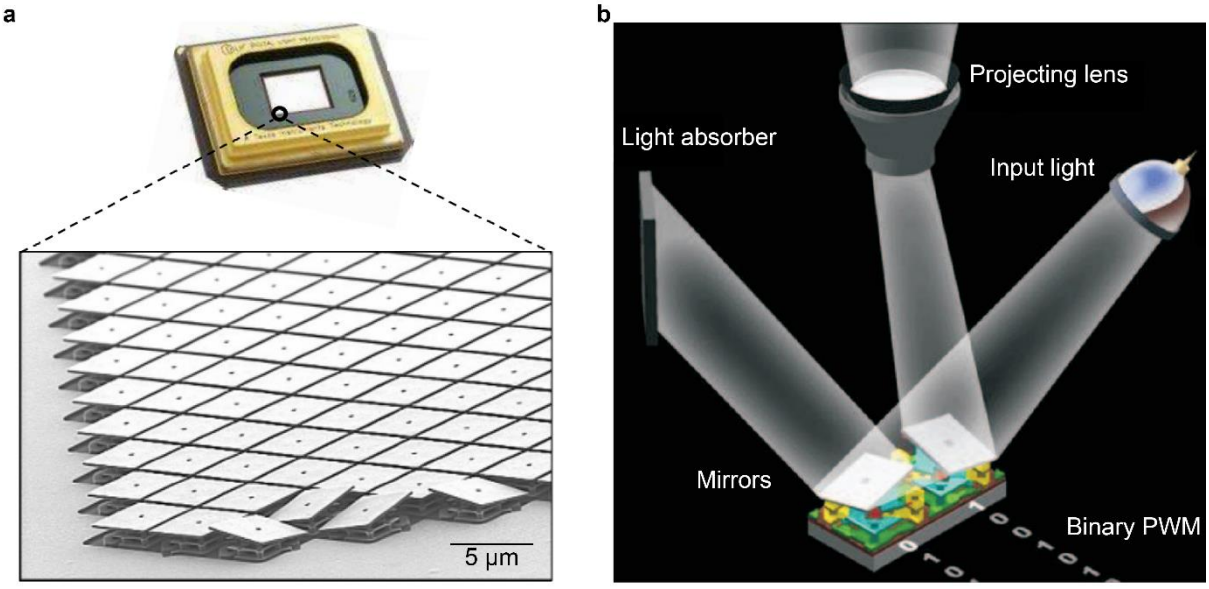

Figure 4.2 | DLP overview: a) Micromirrors arrangement onto the DMD chip. **b)** The DMD pixels oscillate between two stable mirror states, determined by the electrostatics of the pixel during operation. Mirrors orientated in the conventional + (1) position deflect the incoming light onto the projecting lens. Figures adapted from Texas Instruction's application report.

Finally, for most animal models requiring more than three colour channels, the fourth one would most likely be in the very short wavelength range. Optical defects, strong spectral filtering of short-wavelength light in the optics, and chromatic aberration will then emerge with the use of UV light, and optics modification would be necessary within the LCr itself.

To ease the design and retain the commercial advantages of the DLP, the stimulator presented here comprised a pair of LCrs, one for short wavelength and one for long which combines their projection through a dichroic mirror.

One could purchase a regular and short wavelength LCrs with custom optics and LEDs already implemented or decide to build an external illumination unit that will illuminate the DMD chip via a light guide (Tan et al. 2015). Since this spatial stimulator was designed to be coupled with a two-photon microscopy system, the stimulation light requires to be synchronised with the scanning retrace (cf. chapter 3). Two flexible fibre coupled DLP LigthCrafters 4500MKII (Texas Instrument, Dallas, TX) were then purchased as light engines, and two external units combining LED lights through dichroic mirrors before being collimated onto light guides were assembled (Fig 4.3a). The relatively small size of these projectors (10 x 15 x 5 cm) facilitates their integration into existing recording setups. Here, high power LEDs with spectral emission similar to the previous stimulator design were used (Fig 3.2a) so the stimulation spectral composition covered the spectral sensitivities of the larval zebrafish. The two LCr beams were then combined using a long-pass dichroic mirror and projected onto a flat Teflon screen which covered one side of a miniature water-filled aquarium where the larval zebrafish was mounted onto a glass slide under the microscope objective. Teflon was used here for its UV-neutral characteristics.

Each LCr was mounted on a three-axis manipulator to facilitate the alignment of the two images onto the screen and correct any potential chromatic aberration differences between the “short” and “long” wavelength light engines. Here overlapping checkerboards were used to align the two LCs.

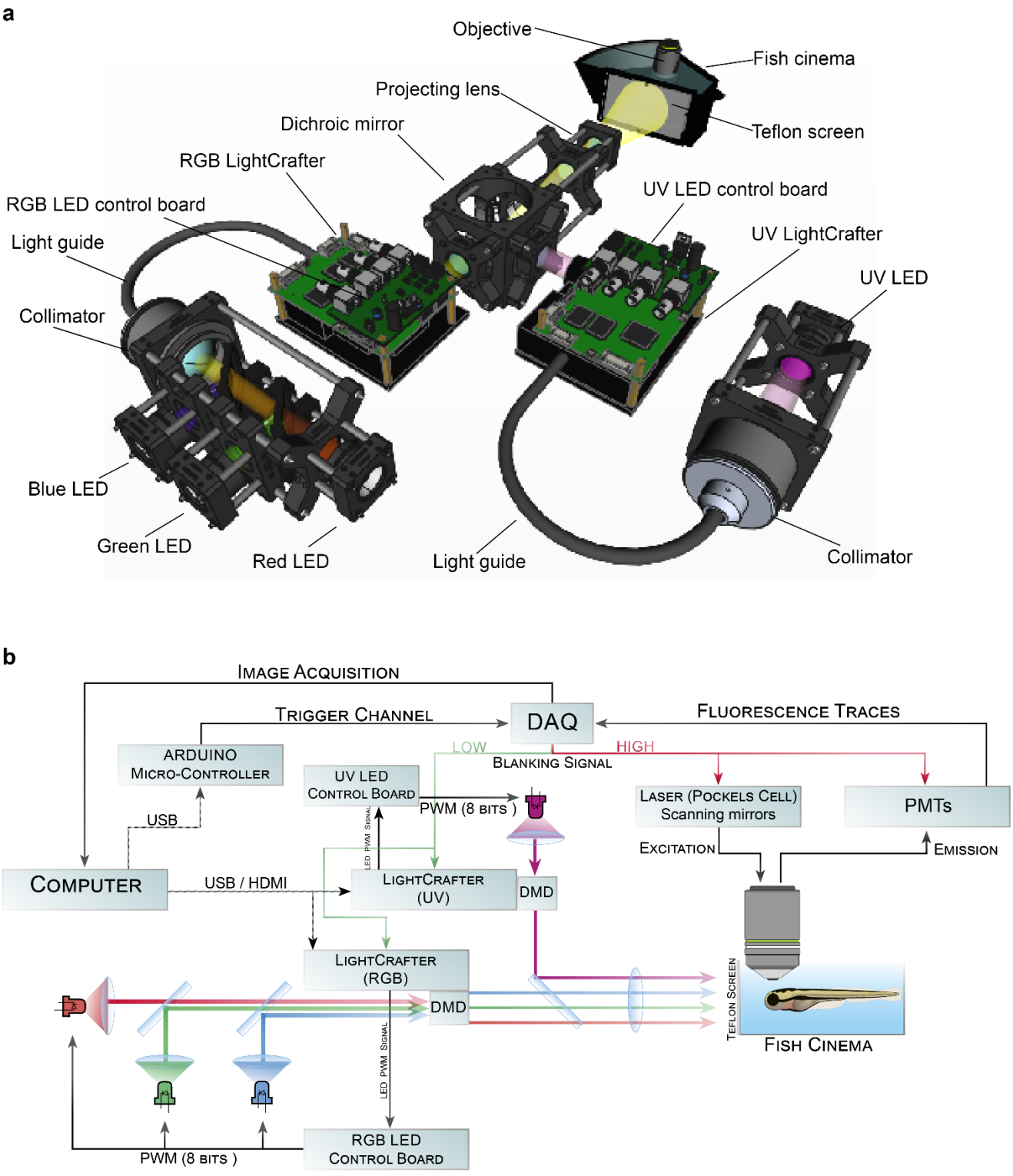

Figure 4.3 | Spatio-chromatic stimulator system: a) Rendering of the spatial stimulator combining an RGB and an UV LightCrafters projecting a tetrachromatic image onto a Teflon screen (UV neutral) positioned in front of the fish fixed in agar under the objective. **b)** Schematics of the described setup.

4.3 – Hardware description

The DLP LightCrafter 4500MKII is a developer version that offers many advantages over its consumer counterpart. Its hardware and electronics circuits are well documented (cf. Appendix 2), thus allowing a customised modulation of LED power. A similar temporal separation approach of light stimulation and fluorescence detection could then also be employed for this stimulator. The use of fibre-coupled LCrs allows further flexibility over the illumination spectra as internal built LEDs and optical filter modification would become a costly and definitive inconvenient. Also, with LEDs being set externally, their synchronisation with any scanning system is facilitated (cf. Chapter 3).

As detailed above, the brightness of an image pixel is encoded by three successive PWM signals which rotate the mirror pixel on the DMD chip towards the projecting lens for the three successive LEDs. While the mirrors resolve the grayscale for a colour channel, the corresponding LED remains constantly on. Therefore, synchronously blanking the LEDs with the two-photon scanning mirrors will not affect the radiometric resolution of the image but will however decrease the overall picture intensity by 20% (the blanking signal duration: the mirror retrace time corresponds to 20% of a scanning line duration, cf. Chapter 3). LEDs power must then be adjusted to compensate for this deficit.

The LCr modulates LED illumination through three digital *control signals* (one for each channel). The *control signal* is here combined with the *blanking signal* originating from the setup DAQ (cf. Chapter 3) onto a logical AND gate. The resulting signal is used to switch the LED power on and off through a combination of P- and N-channel MOSFETs (Fig 4.4, details in Appendix 2). For ease of conception, the *blanking* and *control signals* are integrated on one PCB board which serves as a logic board that can take up to three LED channels and which can be mounted on top of the LCr units, contributing to the system ergonomics (Fig 4.4b left). The LEDs are externally powered on individual PCBs which integrates a variable resistor to adjust each LED to its optimal power. Electronic circuit presented here were designed by fellow lab member A. Maia Chagas.

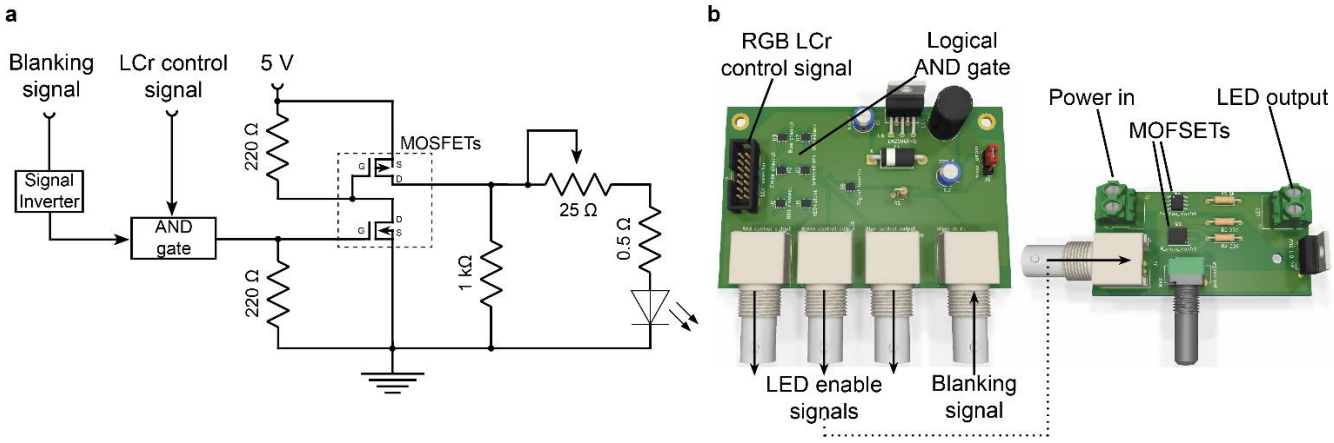

Figure 4.4 | Hardware design: a) Schematics illustrating the circuits controlling the LED light output. **b)** Rendering of the customed LCr add-on and LED power PCBs.

.

The fish cinema onto which the image is projected consists of a watertight 3D-printed model which can accommodate a standard microscope glass slide on which the larval zebrafish is mounted, with one or both eyes orientated towards the screen. The screen is made of a 0.4 mm thick translucid Teflon sheet which, despite absorbing a part of the short wavelength light, does not filter wavelength around the UV spectrum.

As detailed in **2.3**, the larval zebrafish field of view is estimated to 163°, which generates an experimental issue: Currently our setup consists of a conventional diffraction limited two-photon microscope with the laser beam being collimated by the objective. In this setup a 20x water-immersion objective is used with a 2 mm working distance. This relatively short working distance posed a problem: When the microscope is focused on the inner retina, just behind the lens, the objective blocks the upper visual field, rendering it impossible to stimulate the ventral retina (Fig 4.5a). Ongoing setup modification will integrate non-telecentric optics (Janiak et al. 2019) allowing for a larger field of view and – as a side effect in this case - increasing the working distance, thus permitting the examination of the entire larvae field of view. However, in the work presented here, only retinal regions surveying the visual horizon were examined. The 3D-printed larva tank/cinema was therefore set-up to display images in this part of the fish's field of view. The screen distance from the eye was set in accordance with the objective width to avoid any contact with the tank walls.

From the distance between the fish lens and the screen, the projected images can be determined in visual angle values following the formula:

$$V = 2 * \arctan\left(\frac{S}{2D}\right)$$

Where V is the visual angle in degree, D the distance from the screen, and S the size of the object on the screen.

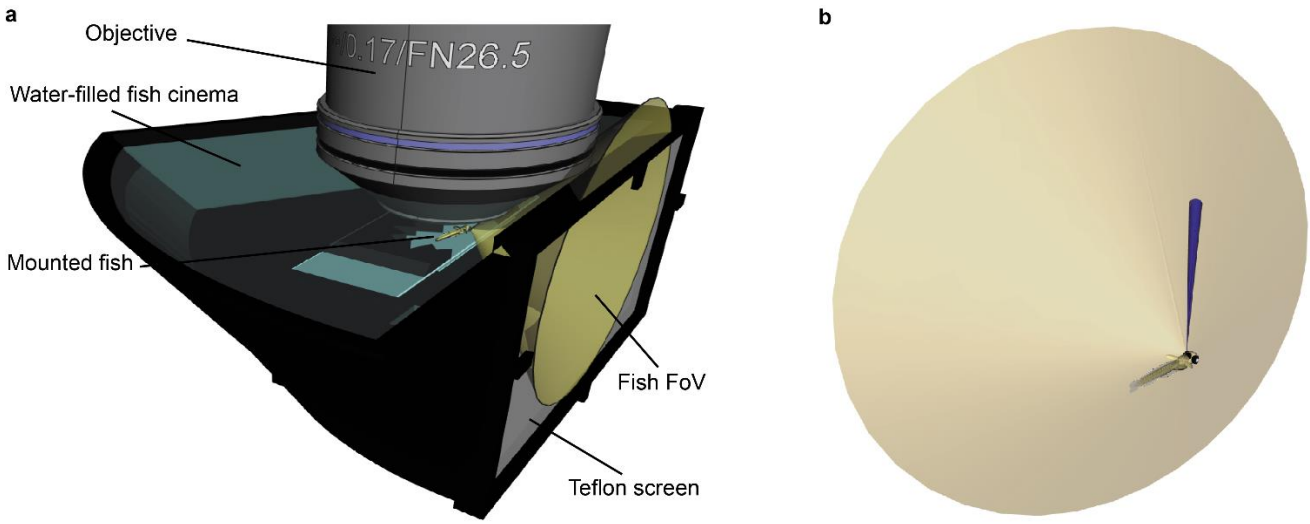

Figure 4.5 | Fish cinema and field of view: a) Rendering of the experimental setup with the larval zebrafish embedded in an agar plate, its body axis orientated parallel to the Teflon screen. **b)** Fish visual field of view (163°, yellow) and visual resolution (3.1°, blue).

For zebrafish larvae aged 5 *dpf*, the visual acuity, using OKR gain was determined to 3.1° (Haug et al. 2010), which for a flat screen positioned at a 26.75 mm distance corresponds to a projected image width of 1.45 mm (Fig 4.5b. blue cone). Although the theorical maximum visual acuity determined by the minimum separable angle between two neighbouring double cones was estimated to 2.09° (Haug et al. 2010), which corresponds to a projected image width of 0.97mm. However PR types are not equally spaced (Fig 1.2 b,c,d) across the retina. Therefore, the spatial resolution for the larval zebrafish is wavelength and position dependent. The higher cone density in the larval retina is located in the *strike zone* and is essentially made by UV cone types: ~3 PR.mm^{-2} (Zimmermann et al. 2018). From this cone spacing, the UV cone-RF diameter was estimated to ~0.76° of visual angle (Yoshimatsu et al. 2020). Still, such resolution undersamples the visual resolution necessary for prey detection which was estimated to be thresholded from 1.8° (Bianco, Kampff, and

Engert 2011; Yoshimatsu et al. 2020). Consequently, to optimally stimulate the fish visual system, the optimal image pixel projected by the stimulator must be below this value.

4.4 – Stimulator calibration

To generate stimuli and control both LCrs in synchrony, the custom written QDSpy software was conceived by Thomas Euler (cf. documentation in appendix 2). This open source visual stimulation software uses the application programming interface (API) OpenGL for stimulus rendering. Stimuli are written in python 3 using the dedicated QDSpy libraries (cf. Appendix 2) for generating objects, setting brightness, colours, and motions. Measurements of LED's intensity curve revealed a non-linear profile (Fig 4.6a). In opposition with the previous stimulator, a linearization of LEDs output could not be performed by modulating the LED current (cf. chapter 3) as LCrs modulate light intensities by varying DMD positions for each pixel and each colour channel. Look-up tables were generated for each colour channel (Fig 4.6b) to be computed by QDSpy for gamma correction on the LCrs output (Fig 4.6c). All calibration guidelines were shared on the open hardware platform in the form of python notebook (cf. Appendix 2).

QDSpy also allows the alignment and overlapping of both LCrs images by presenting RGB output on the first stimulator, and a mirror-inversed UV output on the second one (Fig 4.6d). Here, each colour channel on the second LCr takes a UV input to increase the relative lower power UV LEDs can provide in order to match the RGB LED light levels used on the first LCr, therefore reducing thermal runaway risks on these short-wavelength LEDs (cf. Chapter 3). A simple overlapping checkerboard permits the correction of any image misalignment or chromatic aberration from the stimulator projecting lens between the long (RGB) and short (UV) wavelengths (Fig 4.3) as both LCrs can be adjusted in the three dimensions of space (Fig 4.6d).

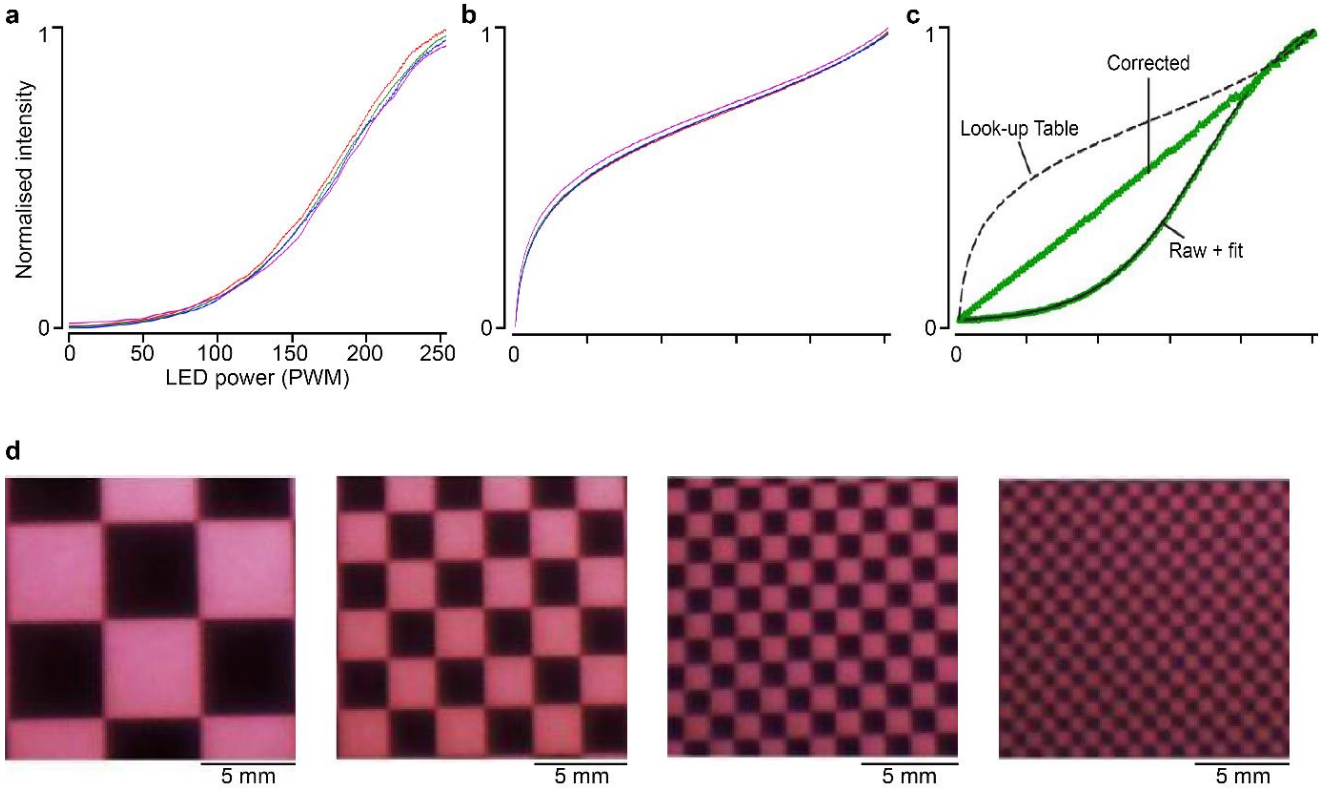

Figure 4.6 | Stimulator calibration: a) Normalised power recordings for all four LEDs displaying a non-linear intensity curve. **b)** Gamma correction calculated for each colour channel. **c)** Non-linearised intensity curve ("raw") with sigmoidal fit (black), look-up table generated from the gamma correction estimation (dotted line) and linearised intensity curve ("corrected") apply to each colour channel. **d)** Checkerboard images displayed on the Teflon screen with varying sizes of dimmed Red LED (dark) from the first LCr and UV LED (pinkish) from the second LCr.

With the current optical system and the Teflon sheet diffusion properties, the maximal resolution achievable is 0.625 mm, which is below the 0.84 mm (1.8° visual angle) required to meet the larval zebrafish maximal visual resolution (Fig 4.6d).

Finally, QDSpy controls the occurrence and duration of *trigger signals* used for stimuli temporal alignment with recorded fluorescence traces. These digital synchronisation signals are generated by an additional Arduino Uno connected to the system DAQ (Fig 4.3b).

To test its performance and reliability, the stimulator was first used to display full field stimuli. BC responses to steps and sine waves of coloured lights were comparable to previous experiments using full field stimulation (Fig 4.7 a,b&c). However, unlike in previous experiments (Chapters 2-3), the larva was here

mounted upright, its retina stimulated from the side while being recording from above. Hence, the experimental limitation detailed in Chapter 2 can be resolved and recording of the inner retina in the frontal plane is now possible in this setup, allowing the investigation of the fish lateral vision. Future experiments will consist of presenting a tetrachromatic white noise to this part of the retina to assess chromatic profiles of BCs surveying the fish horizon.

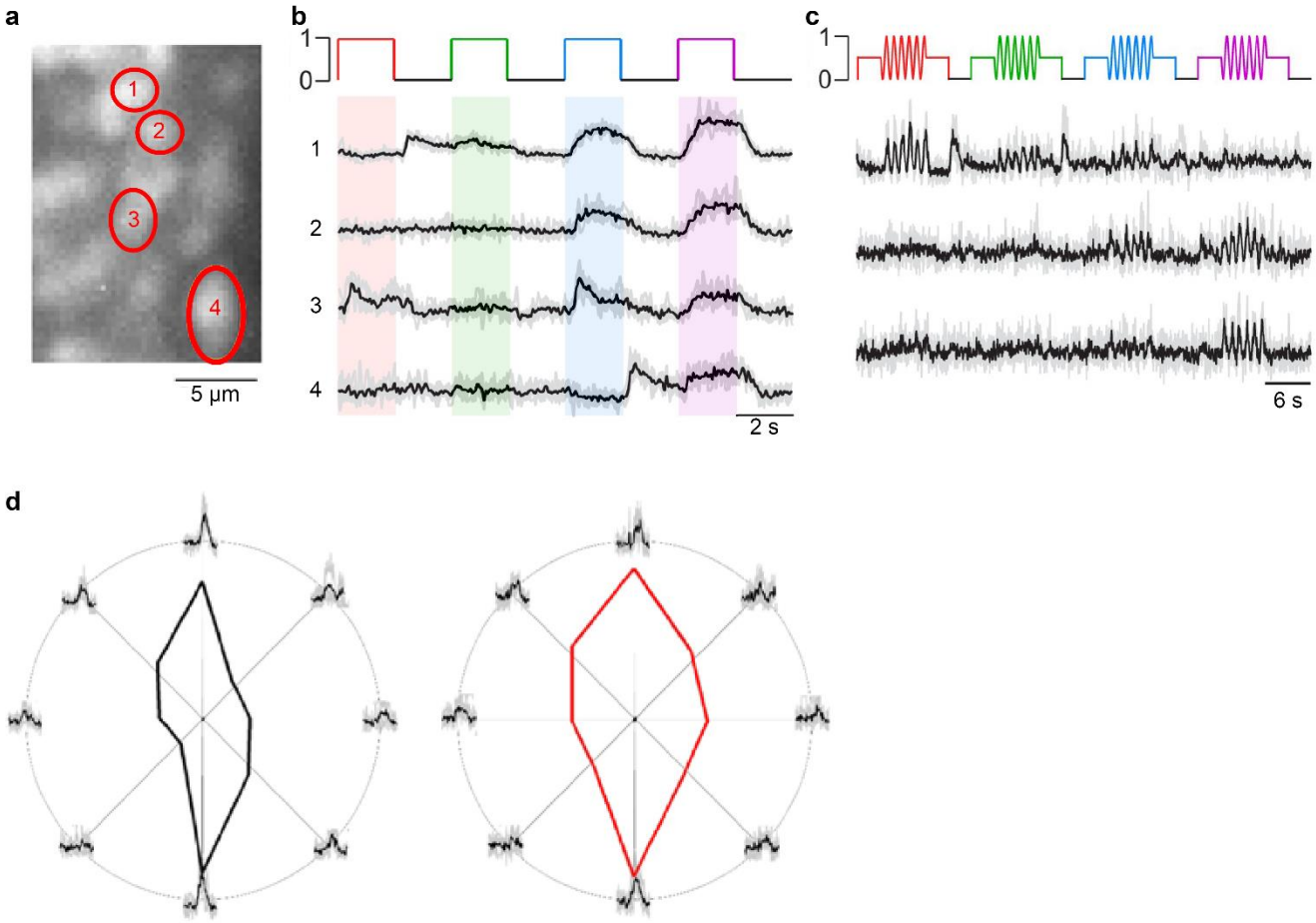

Figure 4.7 | BC response to spatial stimulation a) Two-photon scan field of BCs expressing SyGCamP6f. **b)** Mean Ca^{+} traces in response to red, green, blue and UV full-field flashes. **c)** Mean Ca^{2+} traces in response to full-field sine modulation (at 1 Hz). **d)** Polar plots of ROI orientation-selective response to white (RGBU left) and red (right) moving bars over dark background

Next, the stimulator was used to investigate motion processing by displaying moving bars on the screen. Elongated bars of diverse colours were moved orthogonally to their orientation in eight cardinal directions onto a dark background. BCs with achromatic and chromatic (Red-channel responsive) orientation selectivity

were identified in the nasal region of the retina (Fig 4.7d). Further investigations are required throughout the eye and across retinal neuron classes, nevertheless the spatial stimulator system has demonstrated its ability to generate spatio-chromatic stimuli for the entire desired spectrum and it efficiently drives retinal responses to moving objects.

4.5 – BC spatio-chromatic receptive fields

To determine the spectral and spatial response properties of the zebrafish visual system, a white noise analysis of BC light responses to spatio-chromatic stimulation was conducted (Chichilnisky 2001). Here, uniform and uncorrelated gaussian white noise sequences (one per pixel and colour channel) were used to characterise BC receptive fields (RF). They consisted of 20*30 chequered frames displayed at 10 Hz (Fig 4.8). Similar to the analysis detailed in Chapter 2, ETAs were computed from ROIs Ca^{2+} traces, then through reverse correlation, chromatic kernels were extracted for each pixel and their profiles were finally mapped onto a reconstruction of the stimulation surface.

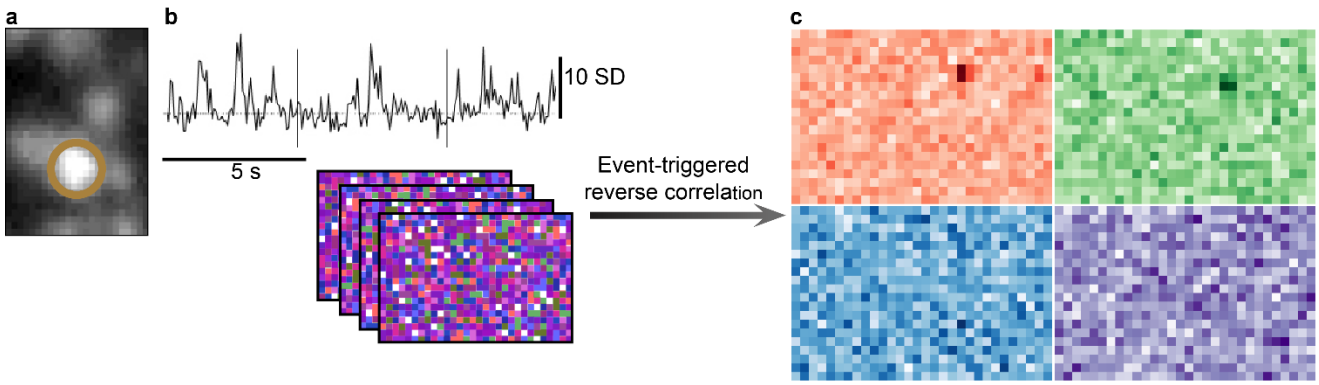

Figure 4.8 | BC responses to spatial tetrachromatic white noise: a) Two-photon scan field of BCs expressing SyGCamP6f. **b)** Mean Ca^{+} traces in response to a gaussian white noise sequence with spatial, temporal and chromatic modulation. **c)** Spatial profile of the ETA for the selected ROI in all colour channels – note the dark pixel clouds in the red and green frames – making this a red-green OFF cell.

In the example shown (Fig 4.9) a spatial white noise with pixel width corresponding to ~5° of visual angle was displayed to the region of the screen surveyed by the medial part of the retina. From this recording, several ROIs exhibited the following

spatio-chromatic profiles (Fig 4.9a). RFs of ~ 12° of visual angle surveying the bottom of the stimulation frame were extracted from the long wavelength channels. As both RF displayed ON- profiles it could be presumed that the observed offset between the RFs corresponds to distinct PR types connection in the outer retina of an ON-, long wavelength sensitive BC. Still, the spatial resolution was not sufficient to clearly identify the RF edges for each colour channel (Fig 4.9b). However, a reduction of the pixel size led to a loss of receptive-field S/N. This was probably due to a combination of light diffusion on the Teflon medium (Fig 4.6d) rendering small objects blurry and the multispectral features each pixel potentially displayed at every frame that overall generates the incapacity for the visual system to resolve sharp chromatic edges between pixels. While in search of a better projection material which possess the same optical properties as Teflon, the white noise stimulation will from there on be displayed sequentially between colour channels with pixel size corresponding to ~2.5° of visual angle. Simply put, each colour channel displayed a hundred patterned frames before moving to the next one. Such stimulation allowed the detection of chromatic edge between illuminated pixels and dark ones while providing no information about chromatic contrast between pixels and therefore could not show any chromatic centre-surround opposition as it expected to find in such visual system (Ruderman, Cronin, and Chiao 1998).

It however yielded some interesting results from the *strike zone* where neighbouring BCs displayed relatively small adjacent UV RFs (~3° of visual angle) of opposite polarities (Fig 4.10a). In comparison, the same stimulation led to the identification of very different spatio-chromatic profiles in the nasal region of the retina where several neighbouring BCs exhibited relatively larger overlapping RF in response to red light stimulation (Fig 4.10b&c).

Systematic recordings across the entire retina are necessary to interpret these preliminary data. However, it can already be observed that BC spatio-chromatic processing functions are not uniformly distributed across the IPL. Moreover, initial tests suggest that UV circuits within the *strike zone* may be particularly small. This goes in line with the density of UV cones observed in this region and the characterisation of this region as a UV-fovea like structure (Yoshimatsu et al. 2020).

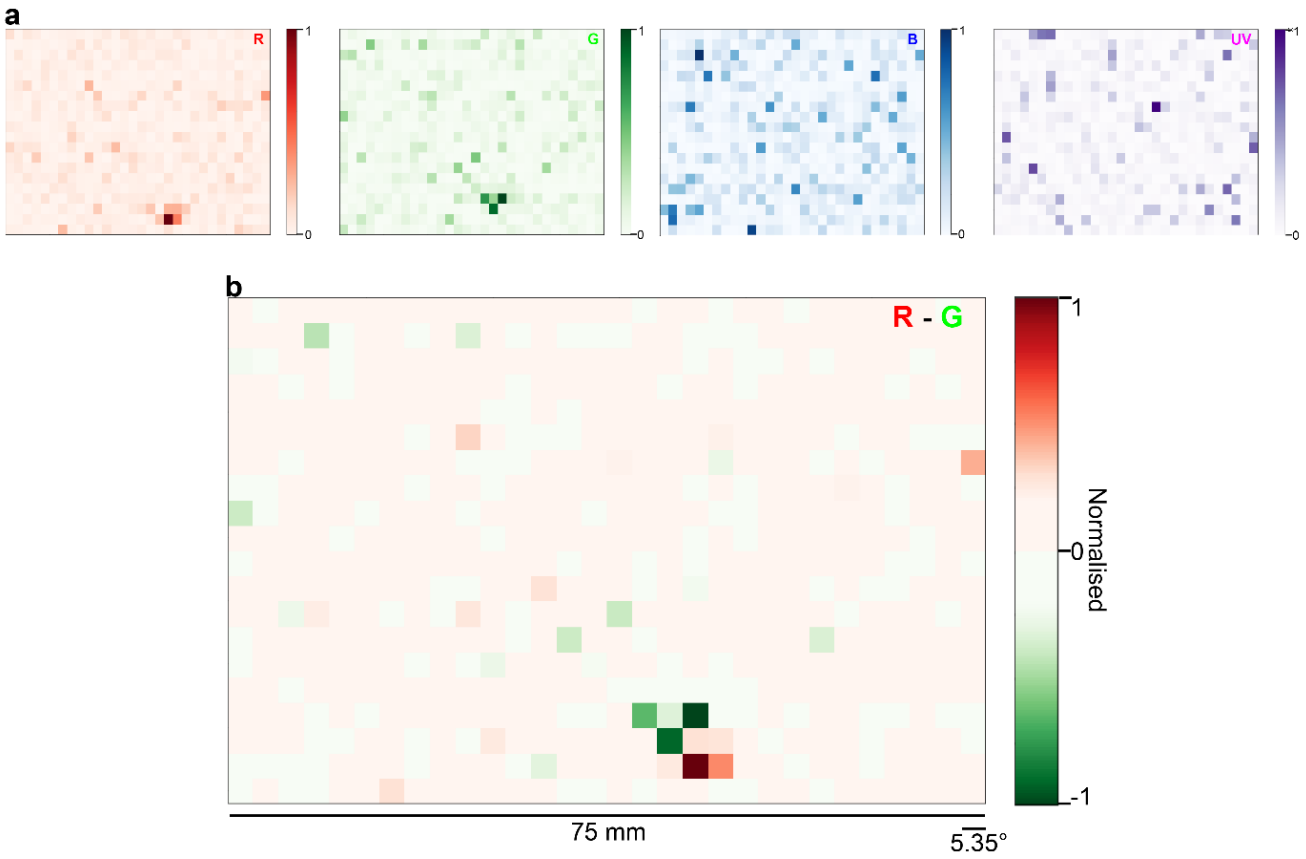

Figure 4.9 | BC chromatic receptive fields: a) Spatial chromatic profiles of a BC from the nasal region. **b)** Superposition of Red and Green spatial profiles. Each pixel corresponds to 5.35° of visual angle.

4.6 – Conclusion

We have presented an open hardware spatial stimulator that can be adapted to any recording system and incorporate up to six distinct spectral channels to fit any animal model's sensitivity spectrum. For a moderate cost (cf. Appendix 2), this high-resolution visual system can easily be replicated in other research centres studying colour vision. The development of this stimulator resulted from a collaboration with the university of Tubingen with the aim to "start a community effort of sharing and further developing a common stimulator design for vision science" (Franke, Maia Chagas, et al. 2019).

Further work is needed to fully appreciate the distribution of chromatic BC RFs and link them with the previously characterised BC chromatic profiles. However, the spatial stimulator demonstrated its ability to display complex spectral moving stimuli with an appreciable temporal resolution without generating any light artefact.

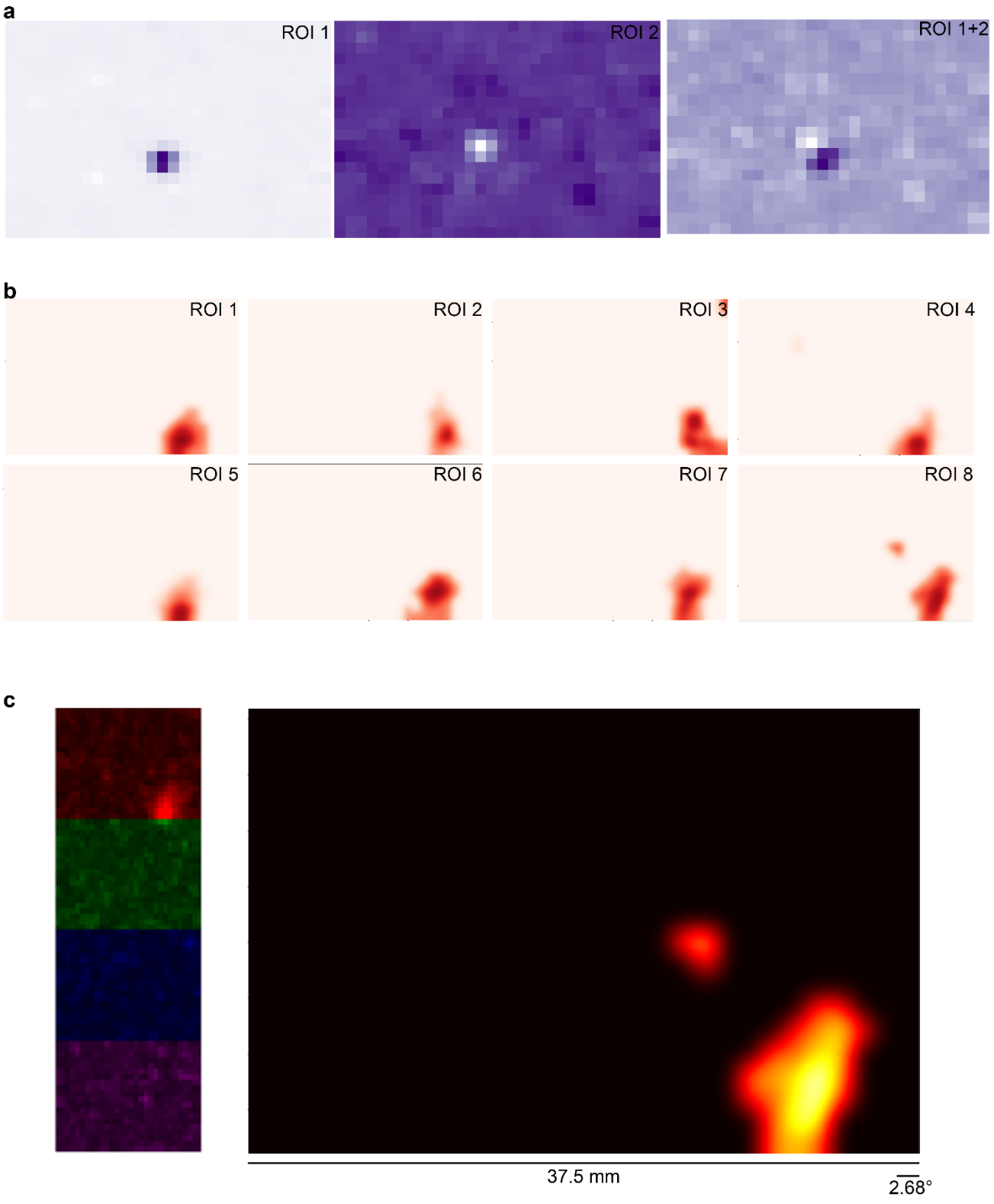

Figure 4.10 | Chromatic receptive fields: a) Spatial profiles of two neighbouring BCs from the *strike zone* displaying opposite polarities **b)** Spatial profiles of eight neighbouring BCs from the nasal retina displaying only Red responses to sequential chromatic white noise (shown as smoothed). **c)** Overlapping colour channel max projection (left) and red channel interpolation (right) of the above BC profiles.

Experimental improvements are still required for high spatial resolution displays, but these only concern the external projection surface and not the stimulation system itself. Indeed, the stimulator resolution remains more than suitable for *ex vivo* experiments where the light is directly projected onto the back of the explanted retina. Nonetheless, the LCr allows relatively large image projections with sufficient resolution for the potential identification of large RF covering a significant portion of the visual field. Simpler versions of this system were also developed for retinal systems which do not require more than three stimulation colour channels, resulting in a less expensive and less complicated stimulator system (i.e. dichroic mouse retina, cf. Appendix 2).

Still, this stimulation system in its current state, represents an important step forward for the exploration of zebrafish chromatic visual processing. Ongoing projects aim to understand how the chromatic signal is spatially processed throughout the entire fish visual pathway. It will also complement our current understanding on chromatic computation in the outer (Yoshimatsu et al. 2020) and inner retina (Zimmermann et al. 2018), and in the RGC layer (Zhou et al. 2020), as well as providing possibilities to assess brain structures' functional organisation. The stimulation system could for example be used to present moving chromatic objects, like UV-bright paramecia hypothesised essential for the fish visual system to detect. Such stimulation would display UV spots of ~2-3° visual angle in different regions of the field of view against different chromatic background with various intensity levels to represent different lighting conditions. Such protocol would highlight visual pathways dedicated to the detection of potential prey (Semmelhack et al. 2014; Antinucci, Folgueira, and Bianco 2019).

Furthermore, QDSpy allows the manipulation of multiple objects from which complex stimulation can be designed from Gabor patches, to motion noise with directional modulation, or even noise modulation over an object for the identification of inhibitory RF portions along the object silhouette (Neri 2015).

Finally, the versatility of this system allows its integration in microscope and external setups thus allowing consistency between behavioural assays and cellular recordings. If the *strike zone,* dedicated to UV detection, allows the fish to distinguish non UV-reflective objects moving against UV-scattering water (Losey et al. 1999), then this system predicts an efficient way to detect predators in the larva's frontal field of view. One could then assess the larval differential escape responses from dark looming stimuli against diverse chromatic backgrounds, and further link

them to tectal responses with the aim to identify specialised UV-related visual circuits.

Chapter 5

General discussion

(T)he retina has always [been] shown to be generous with me ... the retina [is] the oldest and most tenacious of my laboratory loves.

Santiago Ramon y Cajal, Recuerdos de mi vida (1923)

Vision is the primary sense through which the developing zebrafish constructs a representation of the outside world. This is reflected by the proportion of neurons dedicated to the retinal tissue, which for both eyes roughly cumulate ~80,000 neurons while the brain accounts for ~78,000 in a *7 dpf* larva (Hill et al. 2003). The study detailed in chapter 2 was the first to comprehensively detail how a tetrachromatic animal model processes the chromatic information in the inner retina. Currently, most research on colour vision is conducted on dichromatic or de-novo trichromatic mammals. Most non-primate mammals rely on the "ancestral blue-green" opposition system to extract chromatic information from their surrounding environment. Primates from the old world developed an extra colour opponent system following an evolutionary recent gene duplication that led to the occurrence of a new photopigment (Mollon 1989). This "new" trichromacy, which is unusual in many aspects, is well studied, however, not much is known about "older" chromatic computation performed in more colour-specialised retina (i.e. fish, reptiles, amphibians, birds) (Baden and Osorio 2019).

For capturing all chromatic functions within the zebrafish inner retina, the entire class of BC neurons was surveyed *in vivo,* revealing an unprecedented degree of regional visual specialisation in the zebrafish eye. Overall, 25 BC chromatic profiles were characterised along with their specific distribution across the retina and their stratification patterns across the IPL. Furthermore, the retinal distribution of these chromatic profiles was compared to the asymmetrical distribution of spectral statistics from natural scene images that were collected from the animal natural habitat. It then appeared that the IPL organisation, both structurally and functionally, acknowledges the zebrafish visual ecology in several aspects. The various chromatic and colour opponent circuits, predominantly found in the dorsal and nasal region of the retina, surveyed the parts of the visual field from which most chromatic information originated (respectively the lower visual field and the horizon). These regions were systematically organised into neat anatomical stratified layers. Hence suggesting a high degree of structural organisation with the ACs and RGCs dendrites for deconstructing the chromatic signal in these regions. However, the perhaps most interesting part of the retina remained the *strike zone,* an entire retinal region dedicated to the detection of UV-On signals, seemingly at the expense of most other visual functions, a feature that has not yet been reported in other animal model retinae.

Throughout this study, BC functional types could not be reliably related to the pre-established 17 morphological types. Consequently, no data could be obtained from

the distribution of morphological type within the IPL. Further studies will be necessary to determine if anatomical types of BC could be related to specific chromatic functions and if such correlation could be regionally dependent, as to this day, no information regarding the distribution of BC morphology is available in the literature. Also, chromatic profiles were established based on the light responses detected from synaptic terminals and could not be linked to multiple terminal BCs (Fig 1.3). It could be hypothesised that chromatic profiles forming distinct bands within the same region of the IPL (Fig 2.5 insets) could belong to the same BC stratifying at different IPL depth. These features could therefore help to characterise the expected anisotropic distribution of BC morphological types by relating their stratification patterns to functional types' stratification patterns. Following this reasoning, il could be hypothesised that the *strike zone* which only exhibited ON-multi-stratified functional profiles (Fig 2.5a) may be constituted of BCs with multiple axonal terminations spanning across the IPL sublaminae (Fig 1.3a). If such feature could be investigated, it would increase the level of neuronal specialisation observed in this retinal region. It will be further noted that a broad variety of UV computation were identified in this part of the eye (Fig 2.5 UV clusters). A regionalised chromatic specialisation of this magnitude has not yet been observed in other animal models and its local configuration does not follow the conventional parallel retinal organisation detailed in other vertebrate retinae.

Nevertheless, our understanding of the larval zebrafish's inner retinal organisation remains limited by our understanding of what constitutes a defined cellular type. We have seen that the traditional BC categorisation, relying on morphological features and glutamate-elicited currents following "white" light occurrence (Connaughton 2011), could not account for all functional profiles detailed in this work. Also, axonal stratification and dendritic connection patterns are way too diverse to assign functional type to specific connection patterns (Li et al. 2012), especially since it was demonstrated in this piece that genetically defined BC types (identified here with the *xfz43* molecular marker) with similar PR connection pattern exhibited diverse chromatic profiles across the retina (Fig 2.8). More surprising, these defined BC types exhibited UV responses in the ventral retina while they were demonstrated to make no selective connection with UV cones (D'orazi and Yoshimatsu 2016). As the larval zebrafish inner retina appeared non-uniform and highly anisotropically organised, one must consider the influence of regionally specific lateral inhibition from the ACs which may contribute to the generation of the observed BC functional types. Further investigations are then required to fully

apprehend how the inner retina organised itself and how BCs and ACs shape the chromatic signals within the IPL.

Zebrafish possess four distinct cone types. Its retina could, theoretically, perform any of 80 possible chromatic computations. Only about half were identified within the IPL, however they were not equally represented (Fig 2.9). Short versus long wavelength computations (similar to the human blue-yellow system) were instead predominantly found as predicted by models extracting chromatic features from natural scenes (Ruderman, Cronin, and Chiao 1998). Interestingly these computations matched the distribution of specific chromatic contrasts in natural scenes (Zimmermann et al. 2018). It will be noted that the chromatic computations mentioned above originate from recording scans taken only from the eye's sagittal plane. Consequently, a substantial portion of the eye has not yet been investigated. However, if the retinal organisation follows chromatic natural statistic from the environment, it would therefore be expected to observe chromatic profiles similar to the nasal region (region which surveyed the horizon) expand across the entire frontal plane until they reach the borders of the *strike zone*.

Ultimately, these findings indicated the need for experimental improvement over visual stimulation. Consequently, an important part of this thesis was dedicated to the development of open source visual stimulators and experimental protocols.

The constant development of imaging tools, genetically encoded biosensors and the democratisation of electronics along with the constant growing of the hacker and open source hardware communities, allow overcoming research questions that were previously limited for academic institutions due to lack of finances, equipment or skills. Any scientist can make their own tools for a fraction of the cost of a commercially scientific equipment (if available) (Baden et al. 2015). The democratisation of fast prototyping tools (3D printers, CNC, etc.) allows the reproduction and modification of mechanical parts (i.e. optical elements). Open source platforms allows the sharing of design blueprints, source codes and documentation under legally binding open source licenses (Morin, Urban, and Sliz 2012). Overall, the constant advancement of the open source philosophy within academia empowers scientists from similar research fields to exchange experimental techniques and equipment as they would do for scientific knowledge thought their publications. The philosophy behind open source hardware allows users to reproduce, adapt and improve on one's design, in turn enhancing

experimental reproducibility. Freely sharing experimental design and documentation is nowadays an essential criteria for good scientific practice (Maia Chagas 2018).

In this piece, I detailed two innovative stimulation systems conceived for the exploration of chromatic processing in any animal model. As previously detailed, studying colour vision requires fine control over the visual stimulation temporal, spatial and spectral characteristics, and this task can become increasingly complicated depending on the animal model's retina investigated. These new devices will permit the generation of complex chromatic and spatio-chromatic stimuli, greatly extending the range of possible experimental protocols.

Despite these new experimental opportunities, the work carried out for the development of such devices did not find the time to bring sufficient results for the course of this thesis. It has however already produced encouraging results within our lab and in collaborative institutions.

It is my hope that the visual systems described here will find users within the vision neuroscience community and encourage the creation of new research projects that may have been revised due to experimental limitations. With the open visual stimulator, we aimed to "start a community effort" for the development of a common, stimulation tools that would increase reproducibility between labs and enhances visual strategies comparison between animal models.

Science, like open source practices, are collective, collaborative, and corrective. The work carried out during this thesis aims to inscribe itself into this trend.

In regard to the results detailed in this thesis, the logical next step to complete our work would be to develop a behavioural setup assessing zebrafish larvae responses to tetrachromatic stimuli. Many behavioural studies already described a large panel of behaviours from the larval zebrafish in response to moving stimuli (rotating drums, drifting bar, elusive bright spot, dark looming stimuli, etc.) (Schlieper 1927; Schaerer and Neumeyer 1996; Förster et al. 2020). But very few considered implementing these behavioural tests in the full spectral dimension (Krauss and Neumeyer 2003). As previously commented in chapter 4, most experiments rely on commercially available screens, designed for human vision. Therefore, what these studies name "blue" corresponds to "our" blue and equally activates the zebrafish blue and green opsins (Fig. 4.1b). Furthermore, a "white"

colour generated by such screen is white to us as it excites our three cone PRs in a balanced fashion to produce a white metamer (c.f.1.1, Maxwell's experiment). But it will result in a non-white colour for any other animal model. Additionally, when a regular screen is used, the UV cones will not be stimulated and as UV is our primary chromatic interest for this species, a different approach had to be found. One recent study however, ingeniously described a multispectral spatial display made out of 8 by 12 pixel, each containing 5 small custom-chosen LEDs, developed to test colour detection in clown fish (Powell et al. 2021).

In our specific case, we would require a behavioural setup centred around a small dish where free swimming zebrafish larvae, either alone or shoaling would be placed and from which body position, tail movement and eye orientation could be tracked and recorded. Ideally, the dish would be placed in a dome structure on which we could control the spectral content in any azimuthal direction and any vertical elevation. As the time of writing, such stimulating device is still in its developmental stage and no preliminary data could therefore be included in the current thesis. We can however present here our current prototype:

A 3D-printed dome containing 24 * 4 LEDs of the same wavelength as in all previous (and future) experiments (minus the optical filtering) are positioned in eight cardinal directions and three ascending elevation (0, 30 and 60°) and can be controlled individually using an extended LED Zappelin' system as described in chapter 3 (Fig 5.1a). A custom projector system similar to the one described in chapter 4 will also be placed below the dish to investigate various optomotor reflexes by eliciting moving bars and rotating slices with different chromatic combinations in the fish lower visual field of view. This projector system also aims to display small moving objects and looming stimuli of various luminance and chromatic contrasts. The entire system being completed by a conventional 3D-printed rotating drum used in combination with the LEDs positioned at 0° elevation (Fig 5.1b).

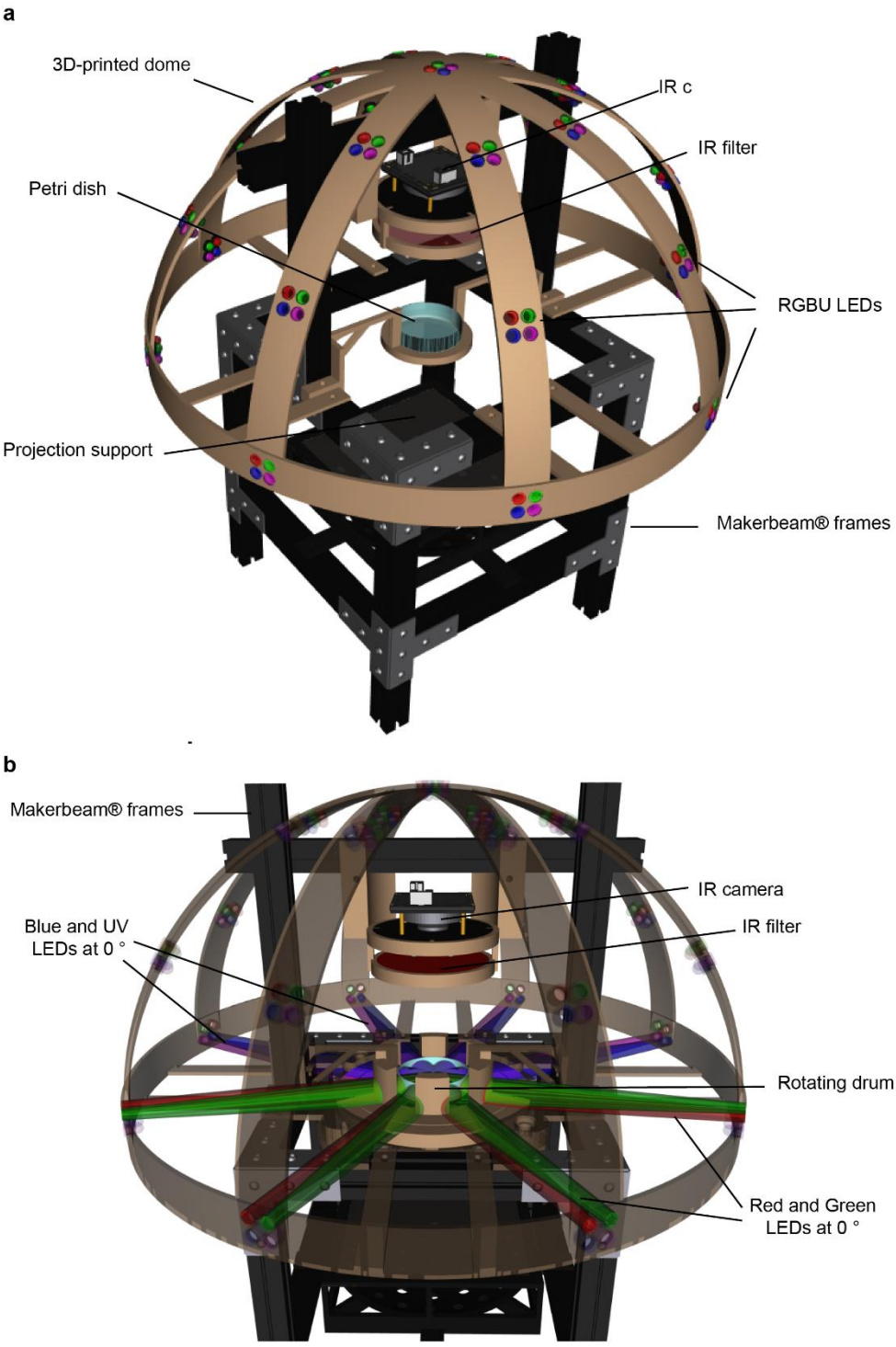

Figure 5.1 | Zebrafish thunderdome: A spatio-chromatic behavioural setup: Working behavioural prototype based on technologies developed in previous chapters. The project documentation and upgrades can be found at https://github.com/BadenLab/Thunderdome **a)** Simplified **r**endering of the system displaying all 96 stimulation LEDs. **b)** Rendering view of the rotating drum experiment with red and green LEDs positioned at 0° illuminating one side of the dish while the other side is illuminated by blue and UV LEDs.

The Arduino code which controls the LEDs is identical to the one described in chapter 3, with the addition of a motor controller script for the rotating drum. The code however is not be played through the Arduino IDE but through Bonsai, an open source event-based framework for processing and controlling data (Lopes et al. 2015). The logic behind this choice is that Bonsai allows the simultaneous control over a wide range of microcontrollers along with video acquisition, screen display (for the projectors) and live tracking. A further advantage for using Bonsai, is that it possesses a developed plugin to integrate DeepLabCut, a “deep learning markerless pose estimation of user-defined body parts” (Mathis et al. 2018; Nath et al. 2019). Therefore, once the neuronal network is trained to recognise the fish body position and eyes orientation, markers can be placed automatically on the live camera feedback, leaving the opportunity in the future to generate algorithms that may adapt the stimulation depending on the zebrafish position and reactions (e.g., moving a bright UV spot away from the fish field of view when its eyes converge in early preying behaviour in order to elicit a tracking / pursuit response).

Moreover, as we described in chapter 2, zebrafish larva retinae use the UV light reflected by zooplankton to localise and hunt them. A typical experiment would then consist in assessing fish hunting performances under various spatio-chromatic illuminations when swimming with zooplankton of different chromatic reflectance (UV bright for paramecia and rotifers, less UV reflective for cyclops and daphnia). Then, determining the importance of each colour channel by selectively inactivate cone PRs, like described in (Yoshimatsu et al. 2020).

As such behavioural experiments would reflect how colour vision contributes to specific behaviours, numerous experimental protocols could be imagined and performed with this ongoing project that will complement the work carried on by collaborators working in the colour processing at every stage of the zebrafish visual pathway. In the end, we might get closer to our goal: understanding what the eye tells the brain when valuable chromatic signals are detected from the fish environment.

Methods and Materials

6.1 - Animals and tissue preparation

All procedures were performed in accordance with the UK Animals (Scientific Procedures) act 1986 and approved by the animal welfare committee of the University of Sussex. For all experiments, 5-9 days post fertilisation (*dpf*) zebrafish (*Danio rerio*) larvae of either sex were used. Animals were housed under a standard 14:10 day/night rhythm and fed three times a day. Animals were grown in 200 µM 1-phenyl-2-thiourea (Sigma) from 1 *dpf* to prevent melanogenesis (Johnny Karlsson, Von Hofsten, and Olsson 2001). Owing to the exploratory nature of this study, no randomisation nor blinding was used.

The following transgenic lines were used: *Tg(-1.8ctbp2:SyGCaMP6)*, *Tg(xfz43:Gal4;UAS:ntr-mCherry;-1.8ctbp2:SyGCaMP6*) (Zhao, Ellingsen, and Fjose 2009). For 2-photon *in-vivo* imaging, zebrafish larvae were immobilised in 2% low melting point agarose (Fisher Scientific, Cat: BP1360-100), placed on the side on a glass coverslip and submersed in fish water. Animals' eye movements were further prevented by injection of α-bungarotoxin (1 nl of 2 mg/ml; Tocris, Cat: 2133) into the ocular muscles behind the eye. For immunohistochemistry, larvae were culled by tricaine overdose (800 mg/l) at 6-8 *dpf*. Whole larvae were fixed in 4% paraformaldehyde for 25 min before being washed in phosphate-buffered saline.

6.2 - Two-photon imaging

We used a MOM-type two-photon microscope (designed by W. Denk, MPI, Martinsried; purchased through Sutter Instruments/Science Products). Design and procedures were described previously (Euler et al. 2009). In brief, the system was equipped with a mode-locked Ti:Sapphire laser (Chameleon Vision-S, Coherent) tuned to 927 nm, two fluorescence detection channels for GCaMP6f (F48x573, AHF/Chroma) and mCherry (F39x628, AHF/Chroma), and a water immersion objective (W Plan-Apochromat 20x/1,0 DIC M27, Zeiss). For imaging mCherry, a 960 nm excitation was used.

Image acquisition, was performed through the custom-written software ScanM (developed by M. Mueller, MPI, Martinsried and T. Euler, CIN, Tuebingen) running under IGOR pro 6.3 for Windows (Wavemetrics), taking either: 64 x 32 pixel image sequences captured at 15.625 frames per second (64 Hz: 32 lines at 2ms line duration) for activity scans compiled in chapter 2, 128 x 64 pixel image sequences captured at 15.625 frames per second (64 Hz: 64 lines at 1ms line duration) for activity scans after the new stimulator implementation described in chapter 3 or 512 x 512 pixel images for high-resolution morphology scans.

6.3 - Pre-processing and receptive field mapping.

Regions of interest (ROIs), corresponding to individual presynaptic terminals of BCs were defined semi-automatically by CellLab, a custom software developed on IGOR PRO 6 (D. Velychko, CIN, cf. (Baden et al. 2016)). Next, the Ca^{2+} traces for each ROI were extracted and de-trended by high-pass filtering above ~0.1 Hz and followed by z-normalisation based on the time interval 1-6 seconds at the beginning of recordings using custom-written routines under IGOR Pro. A stimulus time marker embedded in the recording data served to align the Ca^{2+} traces relative to the visual stimulus with a temporal precision of 2 ms (1 ms since the new stimulator implementation).

Linear receptive fields of each ROI were then mapped by computing the Ca^{2+} transient-triggered-average. To this end, the time-derivative of each trace was resampled to match the stimulus-alignment rate of 500 Hz (or 1 KHz) and thresholding above 0.7 standard deviations relative to the baseline noise was used to the times t_i at which Calcium transients occurred. Ca^{2+} transient-triggered

average stimulus was then computed, weighting each sample by the steepness of the transient:

$$\boldsymbol{F}(l,\tau) = \frac{1}{M}\sum_{i=1}^{M} \dot{\boldsymbol{c}}(t_i)\boldsymbol{S}(o, t_i + \tau)$$

Where, $\boldsymbol{S}(l,t)$ is the stimulus ("LED" and "time"), τ the time lag (ranging from approx. -1,000 to 350 ms) and *M* the number of Ca^{2+} events.

Receptor fields are shown in z-scores for each LED, normalised to the first 50 ms of the time-lag. To select ROIs with a non-random temporal kernel, all four colour kernels were concatenated to a single vector (X by 1) and the standard deviation across this vector was computed. All ROIs with a standard deviation of at least 2 were selected. The precise choice of this quality criterion does not have a major effect on the results (Fig. 2.2b).

6.4 - Feature extraction and clustering.

For each ROI, the receptive kernels for all colours were concatenated, forming one 2,496-dimensional vector (4 times 649) per ROI. This vector was then denoised by using the reconstruction obtained from projecting it on the first 40 PCA components, capturing ~90% of the variance. A feature extraction and clustering pipeline described previously (Baden et al. 2016) was then used. We computed three PCA features on each colour channel individually, yielding a total of 12 features. They captured between 70 and 83% of the variance per channel. By fitting a Gaussian Mixture Model on the data, the Bayesian Information Criterion (BIC) for the number of mixture components was optimised. The covariance matrix of each cluster was chosen to be diagonal and a regularisation term of 10^{-6} was added to the diagonal. Spherical covariance matrices or the same covariance matrix for each cluster yielded higher BIC scores. Full covariance matrices yielded somewhat lower BIC scores with an optimum at a cluster number below 10. In this case, functionally heterogenous clusters were grouped together. This analysis was performed in Python 3.5 using scikit-learn implementations.

6.5 - Grouping of clusters into response groups.

Each cluster was allocated into one of four response groups (n=25) or discarded (n=1). For each cluster mean and each channel, the peak to peak amplitude in z-scores relative to each channels baseline was first calculated, defined as the first 50 ms of each kernel. If the mean difference of the mode of all amplitudes between the UV and all other channels exceeded 35, that cluster was classified as UV(B) monochromatic (Fig 2.5 $C_{6\text{-}14}$). Similarly, a single cluster with mean mode amplitude below 2 was discarded (Fig 2.5 C_x). Next, we calculated the correlation between all pairs of channels as well as the variance between amplitudes, with the mean between amplitudes normalised to 1. If the mean correlation between all pairs exceeded 0.8 (i.e. similar waveforms) and the variance of amplitudes was below 0.09 (i.e. similar amplitudes), that cluster was classified as achromatic (Fig 2.5 $C_{1\text{-}5}$). Finally, to distinguish remaining chromatic (Fig 2.5 $C_{15\text{-}20}$) and colour opponent clusters (Fig 2.5 $C_{21\text{-}25}$), we also computed the mean of the mode of all correlations. If the mean of correlation equalled the mean of the mode of correlations (i.e. all kernels had the same polarity), that cluster was classified as chromatic. All remaining clusters were classified as colour opponent. Following this automatic pre-sorting, we manually reallocated three clusters that were misclassified due to low amplitudes of individual kernels: C_{17} and C_{20} were moved from colour opponent to chromatic as the very low amplitudes of the R-channel led to these clusters' erroneous classification, and C_9 was moved from the chromatic to the UV(B) monochromatic group as this cluster effectively only responded to UV-stimulation but the overall low-amplitudes led its misclassification. Finally, we also moved C_{21} from the chromatic to the opponent group. Here, the pronounced time-course difference between UV(B) and RG that leads to a clear opponency in the early kernel period was not picked up by our automatic sorting rules.

6.6 - Histograms against eye position.

All histograms against eye position were smoothed using a circular 60° binomial (Gaussian) filter along the x-dimension and IPL depth histograms were in addition smoothed by a 5%-width Gaussian filter across the y-dimension. Moreover, all 2D histograms of both eye position and IPL depth (Fig 2.2,4,6,7,8) were weakly warped to horizontally align the peaks of the major anatomical IPL layers across eye position (Fig 2.6a, top row). Specifically, the IPL was compressed from the top by

5% at the outwards horizon and by 5% from the bottom of the IPL at the forward horizon, where the IPL is thickest (Fig 2.3d).

6.7 - Immunohistochemistry

For the IPL structural analysis, whole fixed larvae (8 *dpf*) were incubated in permeabilisation/blocking buffer (PBS with 0.5% Triton-X 100 and 5% normal donkey serum) for at least 10 min followed by 3-5 days incubation at 4°C with primary antibodies (chicken anti-GFP (AbCam, 13970, 1:500), goat anti-ChAT (Chemicon, AB144P, 1:50), rabbit anti-PKCα (Sigma, P4334, 1:100)). Samples were rinsed three times in phosphate buffered saline with 0.5% Trion-X 100 and incubated for another day with secondary antibodies and Hoechst 33342 (1:5000) for nucleus staining in permeabilisation/blocking buffer. Finally, samples were washed in PBS with 0.5% Triton-X 100 and mounted in a mounting media, VectaShield (Vector, H-1000), for fluorescent imaging. Secondary antibodies used were as follows: Donkey anti-chicken IgG CF488A conjugate (Sigma, 1:500), Donkey anti-rabbit IgG CF568 conjugate (Sigma, 1:500), Donkey anti-goat IgG DyLight650 conjugate (BETHYL, 1:200).

Confocal images were taken on Leica TCS SP8 using objectives 63x (HC PL APO oil CS2, Leica), 20x (HC PL APO Dry CS2, Leica), 60x (UPLSAPO oil, Olympus) or 20x (UPLSAPO oil, Olympus) at xy: 0.1-0.07 µm/pixel, and z-step: 0.25-0.3 µm for high-resolution images and 0.7-0.5 µm/pixel, and z-step: 2 µm for low magnification images. Images were median-filtered, contrast and brightness were adjusted in Fiji (NIH).

The IPL edges on whole eye, high definition images were semi-automatically assigned using a custom script written under IGOR Pro 6.3. IPL thickness and signals from the three fluorescence channels were then extracted, linearly computed and average across eye samples.

6.8 – Light stimulation

Before and after the implementation of the new stimulator reviewed in chapter 3, the light source apparatus remained the same. It consists of a custom-built optical cage (ThorLabs) collecting four LED light source and focusing them on the same plane. Four LEDs with narrow spectral width (~ 20 nm) and small beam angle (> 15°) were

used: “Red”: 588 nm, B5B-434-TY, 13.5cd, 20 mA; “Green”: 477 nm, RLS-5B475-S; 3-4 cd, 20mA; “Blue”: 415 nm, VL415-5-15; 10-16 mW, 20 mA; “UV”: 365 nm, LED365-06Z; 5.5 mW, 20 mA (Roithner, Germany). LEDs were filtered (“Red”: FF01–586(20), “Green”: ET480/40x, “Blue”: ET420/40m and “UV”: FF01-370/36) and combined using dichroic mirrors (“Red/Green”: H560LPXR, “Yellow/Blue”: T450/pxr, “White/UV”: T400LP) (all AHF/Chroma) (Fig 6.1). The resulting light was then combined with the laser beam using an infrared beam splitter before passing through the objective (Fig 3.2b).

The final spectra matched the spectral sensitivity of zebrafish R-, G-, B-, and UV-opsins, respectively, while avoiding the two detection bands (Fig 3.2a). LEDs were synchronised with the microscope’s scan retrace at 500 Hz (or 1kHz for the new stimulator). For the older stimulator version, LED intensities were calibrated (in photons per second per cone) such that each LED would stimulate its respective zebrafish cone-type with an equal number of photons (~10^5 photons per cone per s). Assuming an effective absorption coefficient of ~0.1, this translates to ~10^4 photoisomerisations per cone per s (R*), corresponding to a low photopic regime. Here, there was no attempt to compensate for cross-activation of other cones, and relative LED-versus-opsin cross sections are listed in Fig 3.7a. Owing to two-photon excitation of photopigments, an additional, steady illumination of ~10^4 R* was present during the recordings (for detailed discussion, see (Baden et al. 2013; Euler et al. 2009)).

For all experiments, animals were kept at a constant intensity level for at least 5 seconds after the laser scanning started and before light stimuli were presented.

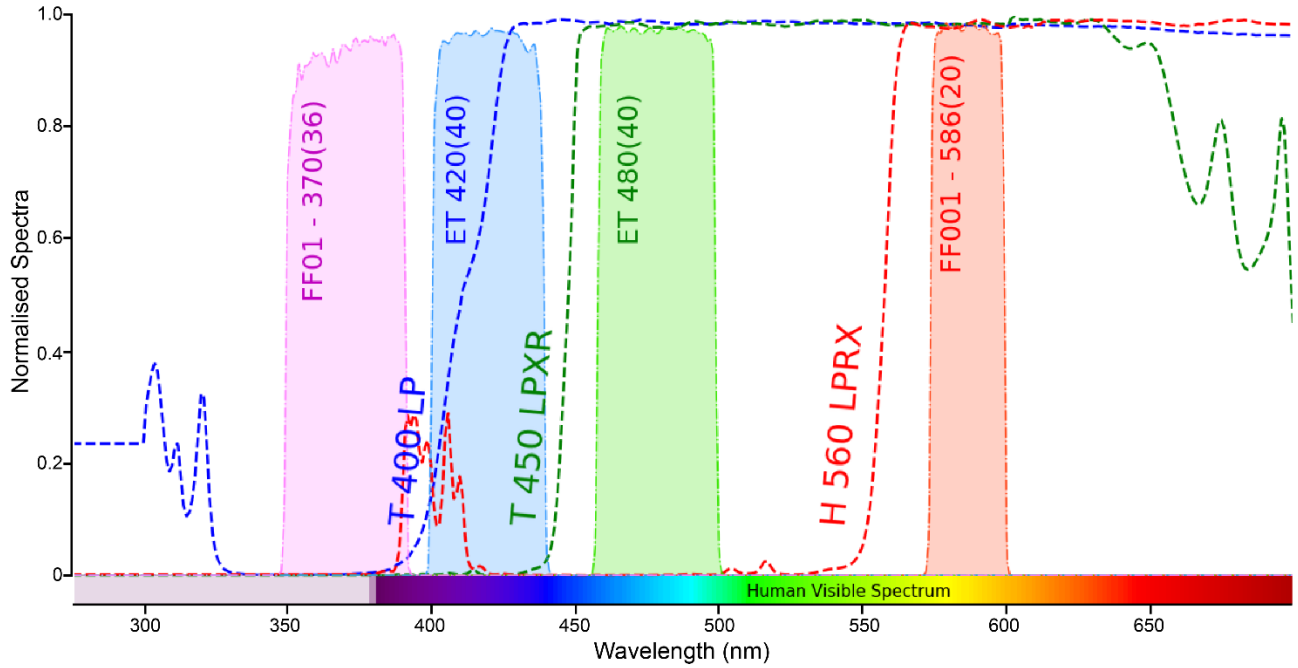

Figure 6.1 | Stimulator configuration a) Normalised transmission and reflectance spectra of optical components used in the full-field stimulator.

References

(211)

Allison, W. Ted, Linda K. Barthel, Kristina M. Skebo, Masaki Takechi, Shoji Kawamura, and Pamela A. Raymond. 2010. “Ontogeny of Cone Photoreceptor Mosaics in Zebrafish.” *Journal of Comparative Neurology*. https://doi.org/10.1002/cne.22447.

Allison, W. Ted, Theodore J. Haimberger, Craig W. Hawryshyn, and Shelby E. Temple. 2004. “Visual Pigment Composition in Zebrafish: Evidence for a Rhodopsin-Porphyropsin Interchange System.” *Visual Neuroscience*. https://doi.org/10.1017/S0952523804216145.

Ammermüller, Josef, and Helga Kolb. 1995. “The Organization of the Turtle Inner Retina. I. ON- and OFF-center Pathways.” *Journal of Comparative Neurology*. https://doi.org/10.1002/cne.903580102.

Antinucci, Paride, Mónica Folgueira, and Isaac H. Bianco. 2019. “Pretectal Neurons Control Hunting Behaviour.” *ELife*. https://doi.org/10.7554/eLife.48114.

Antinucci, Paride, and Robert Hindges. 2016. “A Crystal-Clear Zebrafish for in Vivo Imaging.” *Scientific Reports*. https://doi.org/10.1038/srep29490.

Attneave, Fred. 1954. “Some Informational Aspects of Visual Perception.” *Psychological Review*. https://doi.org/10.1037/h0054663.

Avitan, Lilach, Zac Pujic, Jan Mölter, Michael McCullough, Shuyu Zhu, Biao Sun, Ann Elin Myhre, and Geoffrey J. Goodhill. 2020. “Behavioral Signatures of a Developing Neural Code.” *Current Biology*. https://doi.org/10.1016/j.cub.2020.06.040.

Baden, T., and D. Osorio. 2019. “The Retinal Basis of Vertebrate Color Vision.” *Annual Review of Vision Science*. https://doi.org/10.1146/annurev-vision-091718-014926.

Baden, Tom. 2020. “Vertebrate Vision: Lessons from Non-Model Species.” *Seminars in Cell and Developmental Biology*. https://doi.org/10.1016/j.semcdb.2020.05.028.

———. 2021. “Circuit Mechanisms for Colour Vision in Zebrafish.” *Current Biology*. https://doi.org/10.1016/j.cub.2021.04.053.

Baden, Tom, Philipp Berens, Katrin Franke, Miroslav Román Rosón, Matthias Bethge, and Thomas Euler. 2016. “The Functional Diversity of Retinal Ganglion Cells in the Mouse.” *Nature* 529 (7586): 345–50. https://doi.org/10.1038/nature16468.

Baden, Tom, Andre Maia Chagas, Greg Gage, Timothy Marzullo, Lucia L. Prieto-Godino, and Thomas Euler. 2015. “Open Labware: 3-D Printing Your Own Lab Equipment.” *PLoS Biology* 13 (3). https://doi.org/10.1371/journal.pbio.1002086.

Baden, Tom, Thomas Euler, and Philipp Berens. 2020. “Understanding the Retinal Basis of Vision across Species.” *Nature Reviews Neuroscience*. https://doi.org/10.1038/s41583-019-0242-1.

Baden, Tom, Timm Schubert, L. Le Chang, Tao Wei, Mariana Zaichuk, Bernd Wissinger, Thomas Euler, et al. 2013. “A Tale of Two Retinal Domains: Near-Optimal Sampling of Achromatic Contrasts in Natural Scenes through Asymmetric Photoreceptor Distribution.” *Neuron* 80 (5): 1206–17. https://doi.org/10.1016/j.neuron.2013.09.030.

Barlow, H. B. 1953. “Summation and Inhibition in the Frog’s Retina.” *The Journal of Physiology*. https://doi.org/10.1113/jphysiol.1953.sp004829.

———. 2013. “Possible Principles Underlying the Transformations of Sensory Messages.” In *Sensory Communication*. https://doi.org/10.7551/mitpress/9780262518420.003.0013.

Bartel, Philipp, Filip K. Janiak, Daniel Osorio, and Tom Baden. 2021. “Colourfulness as a Possible Measure of Object Proximity in the Larval Zebrafish Brain.” *Current Biology*. https://doi.org/10.1016/j.cub.2021.01.030.

Behrens, Christian, Timm Schubert, Silke Haverkamp, Thomas Euler, and Philipp Berens. 2016. “Connectivity Map of Bipolar Cells and Photoreceptors in the Mouse Retina.” *ELife* 5 (NOVEMBER2016). https://doi.org/10.7554/eLife.20041.

Bianco, Isaac H., Adam R. Kampff, and Florian Engert. 2011. “Prey Capture Behavior Evoked by Simple Visual Stimuli in Larval Zebrafish.” *Frontiers in Systems Neuroscience* 5. https://doi.org/10.3389/fnsys.2011.00101.

Biehlmaier, Oliver, Stephan C.F. Neuhauss, and Konrad Kohler. 2003. “Synaptic Plasticity and Functionality at the Cone Terminal of the Developing Zebrafish Retina.” *Journal of*

Neurobiology. https://doi.org/10.1002/neu.10243.

Bilotta, Joseph, Shannon Saszik, and Sarah E. Sutherland. 2001. “Rod Contributions to the Electroretinogram of the Dark-Adapted Developing Zebrafish.” *Developmental Dynamics* 222 (4): 564–70. https://doi.org/10.1002/dvdy.1188.

Bleckert, Adam, Gregory W. Schwartz, Maxwell H. Turner, Fred Rieke, and Rachel O.L. Wong. 2014. “Visual Space Is Represented by Nonmatching Topographies of Distinct Mouse Retinal Ganglion Cell Types.” *Current Biology*. https://doi.org/10.1016/j.cub.2013.12.020.

Bonvoisin, Jérémy, Robert Mies, Jean-François Boujut, and Rainer Stark. 2017. “What Is the ‘Source’ of Open Source Hardware?” *Journal of Open Hardware* 1 (1). https://doi.org/10.5334/joh.7.

Bowmaker, J. K., and Y. W. Kunz. 1987. “Ultraviolet Receptors, Tetrachromatic Colour Vision and Retinal Mosaics in the Brown Trout (Salmo Trutta): Age-Dependent Changes.” *Vision Research*. https://doi.org/10.1016/0042-6989(87)90124-6.

Branchek, Theresa, and Ruth Bremiller. 1984. “The Development of Photoreceptors in the Zebrafish, Brachydanio Rerio. I. Structure.” *Journal of Comparative Neurology*. https://doi.org/10.1002/cne.902240109.

Breuninger, Tobias, Christian Puller, Silke Haverkamp, and Thomas Euler. 2011. “Chromatic Bipolar Cell Pathways in the Mouse Retina.” *Journal of Neuroscience*. https://doi.org/10.1523/JNEUROSCI.0616-11.2011.

Browman, H. I., I. Novales-Flamarique, and C. W. Hawryshyn. 1994. “Ultraviolet Photoreception Contributes to Prey Search Behaviour in Two Species of Zooplanktivorous Fishes.” *Journal of Experimental Biology*.

Carleton, Karen L., Daniel Escobar-Camacho, Sara M. Stieb, Fabio Cortesi, and N. Justin Marshall. 2020. “Seeing the Rainbow: Mechanisms Underlying Spectral Sensitivity in Teleost Fishes.” *Journal of Experimental Biology*. https://doi.org/10.1242/jeb.193334.

Chang, Le, Tobias Breuninger, and Thomas Euler. 2013. “Chromatic Coding from Cone-Type Unselective Circuits in the Mouse Retina.” *Neuron*. https://doi.org/10.1016/j.neuron.2012.12.012.

Chichilnisky, E. J. 2001. “A Simple White Noise Analysis of Neuronal Light Responses.” *Network: Computation in Neural Systems*. https://doi.org/10.1088/0954-898X/12/2/306.

Collin, Shaun P., Wayne L. Davies, Nathan S. Hart, and David M. Hunt. 2009. “The

Evolution of Early Vertebrate Photoreceptors." *Philosophical Transactions of the Royal Society B: Biological Sciences*. https://doi.org/10.1098/rstb.2009.0099.

Collin, Shaun P., and Justin N. Marshall. 2003. *Sensory Processing in Aquatic Environments*. *Sensory Processing in Aquatic Environments*. https://doi.org/10.1007/b97656.

Collin, Shaun P., and Julia Shand. 2008. "Retinal Sampling and the Visual Field in Fishes." In *Sensory Processing in Aquatic Environments*. https://doi.org/10.1007/978-0-387-22628-6_8.

Connaughton, V. P., D. Graham, and R. Nelson. 2004. "Identification and Morphological Classification of Horizontal, Bipolar, and Amacrine Cells within the Zebrafish Retina." *Journal of Comparative Neurology* 477 (4): 371–85. https://doi.org/10.1002/cne.20261.

Connaughton, V. P., and R. Nelson. 2000. "Axonal Stratification Patterns and Glutamate-Gated Conductance Mechanisms in Zebrafish Retinal Bipolar Cells." *Journal of Physiology* 524 (1): 135–46. https://doi.org/10.1111/j.1469-7793.2000.t01-1-00135.x.

Connaughton, V P. 2011. "Bipolar Cells in the Zebrafish Retina." *Visual Neuroscience* 28 (1): 77–93. https://doi.org/10.1017/S0952523810000295.

Connaughton, Victoria P., and Ralph Nelson. 2010. "Spectral Responses in Zebrafish Horizontal Cells Include a Tetraphasic Response and a Novel UV-Dominated Triphasic Response." *Journal of Neurophysiology*. https://doi.org/10.1152/jn.00644.2009.

Cronin, T. W. 2008. "Visual Ecology." In *The Senses: A Comprehensive Reference*. https://doi.org/10.1016/B978-012370880-9.00337-6.

Cronin, Thomas W., and Michael J. Bok. 2016. "Photoreception and Vision in the Ultraviolet." *Journal of Experimental Biology*. https://doi.org/10.1242/jeb.128769.

Crook, Joanna D., Michael B. Manookin, Orin S. Packer, and Dennis M. Dacey. 2011. "Horizontal Cell Feedback without Cone Type-Selective Inhibition Mediates 'Red-Green' Color Opponency in Midget Ganglion Cells of the Primate Retina." *Journal of Neuroscience*. https://doi.org/10.1523/JNEUROSCI.4385-10.2011.

Cummings, Molly E., and John A. Endler. 2018. "25 Years of Sensory Drive: The Evidence and Its Watery Bias." *Current Zoology*. https://doi.org/10.1093/cz/zoy043.

D'orazi, Florence D., and Takeshi Yoshimatsu. 2016. "Development of Synaptic Input Patterns on Dendrites of Retinal Neurons." In *Dendrites: Development and Disease*, 489–522. https://doi.org/10.1007/978-4-431-56050-0_19.

Dartnall, H. J.A. 1968. “The Photosensitivities of Visual Pigments in the Presence of Hydroxylamine.” *Vision Research*. https://doi.org/10.1016/0042-6989(68)90104-1.

Davies, Wayne I L, Lei Zheng, Steven Hughes, T. Katherine Tamai, Michael Turton, Stephanie Halford, Russell G. Foster, David Whitmore, and Mark W. Hankins. 2011. “Functional Diversity of Melanopsins and Their Global Expression in the Teleost Retina.” *Cellular and Molecular Life Sciences* 68 (24): 4115–32. https://doi.org/10.1007/s00018-011-0785-4.

Dehmelt, Florian A., Adam Von Daranyi, Claire Leyden, and Aristides B. Arrenberg. 2018. “Evoking and Tracking Zebrafish Eye Movement in Multiple Larvae with ZebEyeTrack.” *Nature Protocols*. https://doi.org/10.1038/s41596-018-0002-0.

Dehmelt, Florian A, Rebecca Meier, Julian Hinz, Takeshi Yoshimatsu, Clara A Simacek, Kun Wang, Tom Baden, and Aristides B Arrenberg. 2019. “Spherical Arena Reveals Optokinetic Response Tuning to Stimulus Location, Size and Frequency across Entire Visual Field of Larval Zebrafish.” *BioRxiv*, January, 754408. https://doi.org/10.1101/754408.

Denk, Winfried, and Karel Svoboda. 1997. “Photon Upmanship: Why Multiphoton Imaging Is More than a Gimmick.” *Neuron*. https://doi.org/10.1016/S0896-6273(00)81237-4.

DeVries, Steven H., and Eric A. Schwartz. 1999. “Kainate Receptors Mediate Synaptic Transmission between Cones and ‘Off’ Bipolar Cells in a Mammalian Retina.” *Nature*. https://doi.org/10.1038/16462.

Dowling, J. E. 2009. “Retina: An Overview.” In *Encyclopedia of Neuroscience*. https://doi.org/10.1016/B978-008045046-9.00924-4.

Dreosti, Elena, Benjamin Odermatt, Mario M Dorostkar, and Leon Lagnado. 2009. “A Genetically Encoded Reporter of Synaptic Activity in Vivo.” *Nature Methods* 6 (12): 883–89. https://doi.org/10.1038/nmeth.1399.

Easter, Stephen S., and Gregory N. Nicola. 1996. “The Development of Vision in the Zebrafish (Danio Rerio).” *Developmental Biology*. https://doi.org/10.1006/dbio.1996.0335.

———. 1997. “The Development of Eye Movements in the Zebrafish (Danio Rerio).” *Developmental Psychobiology*. https://doi.org/10.1002/(SICI)1098-2302(199712)31:4<267::AID-DEV4>3.0.CO;2-P.

Endeman, Duco, Lauw J. Klaassen, and Maarten Kamermans. 2013. “Action Spectra of

Zebrafish Cone Photoreceptors." *PLoS ONE*. https://doi.org/10.1371/journal.pone.0068540.

Endler, J. A. 1992a. "Sensory Drive. Does Sensory Drive Biology Bias or Constrain the Direction of Evolution?" *The American Naturalist*.

———. 1992b. "Signals, Signal Conditions, and the Direction of Evolution." *American Naturalist*. https://doi.org/10.1086/285308.

Engström, Kjell. 1960. "Cone Types and Cone Arrangement in the Retina of Some Cyprinids." *Acta Zoologica*. https://doi.org/10.1111/j.1463-6395.1960.tb00481.x.

Estévez, O., and H. Spekreijse. 1982. "The 'Silent Substitution' Method in Visual Research." *Vision Research*. https://doi.org/10.1016/0042-6989(82)90104-3.

Euler, Thomas, Katrin Franke, and Tom Baden. 2019. "Studying a Light Sensor with Light: Multiphoton Imaging in the Retina." In *Neuromethods*. https://doi.org/10.1007/978-1-4939-9702-2_10.

Euler, Thomas, Susanne E. Hausselt, David J. Margolis, Tobias Breuninger, Xavier Castell, Peter B. Detwiler, and Winfried Denk. 2009. "Eyecup Scope-Optical Recordings of Light Stimulus-Evoked Fluorescence Signals in the Retina." *Pflugers Archiv European Journal of Physiology* 457 (6): 1393–1414. https://doi.org/10.1007/s00424-008-0603-5.

Euler, Thomas, Silke Haverkamp, Timm Schubert, and Tom Baden. 2014a. "Retinal Bipolar Cells: Elementary Building Blocks of Vision." *Nature Reviews Neuroscience* 15 (8): 507–19. https://doi.org/10.1038/nrn3783.

———. 2014b. "Retinal Bipolar Cells: Elementary Building Blocks of Vision." *Nature Reviews Neuroscience* 15 (8): 507–19. https://doi.org/10.1038/nrn3783.

Feuda, Roberto, Ferdinand Marlétaz, Michael A. Bentley, and Peter W.H. Holland. 2016. "Conservation, Duplication, and Divergence of Five Opsin Genes in Insect Evolution." *Genome Biology and Evolution*. https://doi.org/10.1093/gbe/evw015.

Flamarique, Iñigo Novales. 2013. "Opsin Switch Reveals Function of the Ultraviolet Cone in Fish Foraging." *Proceedings of the Royal Society B: Biological Sciences*. https://doi.org/10.1098/rspb.2012.2490.

Förster, Dominique, Thomas O. Helmbrecht, Duncan S. Mearns, Linda Jordan, Nouwar Mokayes, and Herwig Baier. 2020. "Retinotectal Circuitry of Larval Zebrafish Is Adapted to Detection and Pursuit of Prey." *ELife*. https://doi.org/10.7554/eLife.58596.

Franke, Katrin, Philipp Berens, Timm Schubert, Matthias Bethge, Thomas Euler, and Tom

Baden. 2016. “Balanced Excitation and Inhibition Decorrelates Visual Feature Representation in the Mammalian Inner Retina.” *BioRxiv*. https://doi.org/10.1101/040642.

———. 2017. “Inhibition Decorrelates Visual Feature Representations in the Inner Retina.” *Nature*. https://doi.org/10.1038/nature21394.

Franke, Katrin, André Maia Chagas, Zhijian Zhao, Maxime J Y Zimmermann, Yongrong Qiu, Klaudia Szatko, Tom Baden, and Thomas Euler. 2019. “An Arbitrary-Spectrum Spatial Visual Stimulator for Vision Research.” *BioRxiv*, January, 649566. https://doi.org/10.1101/649566.

Franke, Katrin, André Maia Chagas, Zhijian Zhao, Maxime JY Zimmermann, Philipp Bartel, Yongrong Qiu, Klaudia P Szatko, Tom Baden, and Thomas Euler. 2019. “An Arbitrary-Spectrum Spatial Visual Stimulator for Vision Research.” *ELife* 8 (September). https://doi.org/10.7554/eLife.48779.

Friesike, Sascha, and Thomas Schildhauer. 2015. “Open Science: Many Good Resolutions, Very Few Incentives, Yet.” In *Incentives and Performance*, 277–89. Cham: Springer International Publishing. https://doi.org/10.1007/978-3-319-09785-5_17.

Ghosh, Krishna K., Sascha Bujan, Silke Haverkamp, Andreas Feigenspan, and Heinz Wässle. 2004. “Types of Bipolar Cells in the Mouse Retina.” *Journal of Comparative Neurology*. https://doi.org/10.1002/cne.10985.

Govardovskii, V. I., A. L. Byzov, L. V. Zueva, N. A. Pousczuk, and E. A. Baburina. 1991. “Spectral Characteristics of Photoreceptors and Horizontal Cells in the Retina of the Siberian Sturgeon Acipenser Baeri Brandt.” *Vision Research*. https://doi.org/10.1016/0042-6989(91)90162-X.

Govardovskii, Victor I., Nanna Fyhrquist, Tom Reuter, Dmitry G. Kuzmin, and Kristian Donner. 2000. “In Search of the Visual Pigment Template.” *Visual Neuroscience*. https://doi.org/10.1017/S0952523800174036.

Greferath, Ursula, Ulrike Grünert, and Heinz Wässle. 1990. “Rod Bipolar Cells in the Mammalian Retina Show Protein Kinase C-like Immunoreactivity.” *Journal of Comparative Neurology*. https://doi.org/10.1002/cne.903010308.

Hansen, Thorsten, and Karl R. Gegenfurtner. 2009. “Independence of Color and Luminance Edges in Natural Scenes.” *Visual Neuroscience*. https://doi.org/10.1017/S0952523808080796.

Hartline, H. K. 1938. “THE RESPONSE OF SINGLE OPTIC NERVE FIBERS OF THE VERTEBRATE EYE TO ILLUMINATION OF THE RETINA.” *American Journal of Physiology-Legacy Content*. https://doi.org/10.1152/ajplegacy.1938.121.2.400.

Haug, Marion F., Manuela Berger, Matthias Gesemann, and Stephan C.F. Neuhauss. 2019. “Differential Expression of PKCα and -β in the Zebrafish Retina.” *Histochemistry and Cell Biology*. https://doi.org/10.1007/s00418-018-1764-8.

Haug, Marion F., Oliver Biehlmaier, Kaspar P. Mueller, and Stephan C.F. Neuhauss. 2010. “Visual Acuity in Larval Zebrafish: Behavior and Histology.” *Frontiers in Zoology*. https://doi.org/10.1186/1742-9994-7-8.

Haverkamp, S., D. Inta, H. Monyer, and H. Wässle. 2009. “Expression Analysis of Green Fluorescent Protein in Retinal Neurons of Four Transgenic Mouse Lines.” *Neuroscience*. https://doi.org/10.1016/j.neuroscience.2009.01.081.

Haverkamp, Silke, and Heinz Wässle. 2000. “Immunocytochemical Analysis of the Mouse Retina.” *Journal of Comparative Neurology*. https://doi.org/10.1002/1096-9861(20000814)424:1<1::AID-CNE1>3.0.CO;2-V.

Haverkamp, Silke, Heinz Wässle, Jens Duebel, Thomas Kuner, George J. Augustine, Guoping Feng, and Thomas Euler. 2005. “The Primordial, Blue-Cone Color System of the Mouse Retina.” *Journal of Neuroscience*. https://doi.org/10.1523/JNEUROSCI.1117-05.2005.

Hecht, Seug, and Cornelis D. Verrijp. 1933. “Intermittent Stimulation by Light III. the Relation between Intensity and Critical Fusion Frequency for Different Retinal Locations.” *Journal of General Physiology*. https://doi.org/10.1085/jgp.17.2.251.

Heidelberger, Ruth, Wallace B. Thoreson, and Paul Witkovsky. 2005. “Synaptic Transmission at Retinal Ribbon Synapses.” *Progress in Retinal and Eye Research*. NIH Public Access. https://doi.org/10.1016/j.preteyeres.2005.04.002.

Helmchen, Fritjof, and Winfried Denk. 2005. “Deep Tissue Two-Photon Microscopy.” *Nature Methods*. https://doi.org/10.1038/nmeth818.

Helmholtz, Hermann von. 1866. *Treatise on Physiological Optics*. *Book*.

Helmstaedter, Moritz, Kevin L. Briggman, Srinivas C. Turaga, Viren Jain, H. Sebastian Seung, and Winfried Denk. 2013. “Connectomic Reconstruction of the Inner Plexiform Layer in the Mouse Retina.” *Nature*. https://doi.org/10.1038/nature12346.

Hill, Adrian, C. Vyvyan Howard, Uwe Strahle, and Andrew Cossins. 2003.

"Neurodevelopmental Defects in Zebrafish (Danio Rerio) at Environmetally Relevant Dioxin (TCDD) Concentrations." *Toxicological Sciences*. https://doi.org/10.1093/toxsci/kfg241.

Hohman, Becky. 2007. "The LED Light Source: A Major Advance in Fluorescence Microscopy." *American Biotechnology Laboratory*. https://doi.org/10.2345/0899-8205(2007)41[461:LLSMAI]2.0.CO;2.

Hornbeck, LJ. 1996. USOO5583688A, issued December 21, 1996.

Hubel, D. H., and T. N. Wiesel. 1968. "Receptive Fields and Functional Architecture of Monkey Striate Cortex." *The Journal of Physiology*. https://doi.org/10.1113/jphysiol.1968.sp008455.

Hurvich, Leo M., and Dorothea Jameson. 1960. "Perceived Color, Induction Effects, and Opponent-Response Mechanisms." *Journal of General Physiology*. https://doi.org/10.1085/jgp.43.6.63.

Icha, Jaroslav, Michael Weber, Jennifer C. Waters, and Caren Norden. 2017. "Phototoxicity in Live Fluorescence Microscopy, and How to Avoid It." *BioEssays*. https://doi.org/10.1002/bies.201700003.

Ishihara, Makoto. 1906. "Versuch Einer Deutung Der Photoelektrischen Schwankungen Am Froschauge." *Pflüger, Archiv Für Die Gesammte Physiologie Des Menschen Und Der Thiere*. https://doi.org/10.1007/BF01677147.

Jacobs, G. H. 1993. "The Distribution and Nature of Colour Vision among the Mammals." *Biological Reviews of the Cambridge Philosophical Society*. https://doi.org/10.1111/j.1469-185X.1993.tb00738.x.

Janiak, Filip, Phillip Bartel, Michael Bale, Takeshi Yoshimatsu, Mingyi Zhou, Lucia L. Prieto-Godino, Thomas Euler, et al. 2018. "An Ultra-Low-Cost Module for Large Field-of-View 3D Random Access 2-Photon Microscopy." *F1000Research*. https://doi.org/10.7490/F1000RESEARCH.1116332.1.

Johnston, Jamie, Federico Esposti, and Leon Lagnado. 2012. "Color Vision: Retinal Blues." *Current Biology*. https://doi.org/10.1016/j.cub.2012.07.022.

Jordan, Rebecca, David Howe, Francis Juanes, Jay Stauffer, and Ellis Loew. 2004. "Ultraviolet Radiation Enhances Zooplanktivory Rate in Ultraviolet Sensitive Cichlids." *African Journal of Ecology*. https://doi.org/10.1111/j.1365-2028.2004.00494.x.

Kalueff, Allan V., Michael Gebhardt, Adam Michael Stewart, Jonathan M. Cachat, Mallorie

Brimmer, Jonathan S. Chawla, Cassandra Craddock, et al. 2013. “Towards a Comprehensive Catalog of Zebrafish Behavior 1.0 and Beyond.” *Zebrafish* 10 (1): 70–86. https://doi.org/10.1089/zeb.2012.0861.

Kameyama, Koichiro, Mercedes Jiménez, Jacqueline Muller, Yasuo Ishida, and Vincent J. Hearing. 1989. “Regulation of Mammalian Melanogenesis by Tyrosinase Inhibition.” *Differentiation*. https://doi.org/10.1111/j.1432-0436.1989.tb00604.x.

Karlsson, J, J von Hofsten, and P E Olsson. 2001. “Generating Transparent Zebrafish: A Refined Method to Improve Detection of Gene Expression during Embryonic Development.” *Mar Biotechnol (NY)* 3 (6): 522–27. https://doi.org/10.1007/s1012601-0053-4.

Karlsson, Johnny, Jonas Von Hofsten, and Per Erik Olsson. 2001. “Generating Transparent Zebrafish: A Refined Method to Improve Detection of Gene Expression during Embryonic Development.” *Marine Biotechnology*. https://doi.org/10.1007/s1012601-0053-4.

Kelsh, Robert N., Michael Brand, Yun Jin Jiang, Carl Philipp Heisenberg, Shuo Lin, Pascal Haffter, Jörg Odenthal, et al. 1996. “Zebrafish Pigmentation Mutations and the Processes of Neural Crest Development.” *Development*.

Kimmel, Charles B., William W. Ballard, Seth R. Kimmel, Bonnie Ullmann, and Thomas F. Schilling. 1995. “Stages of Embryonic Development of the Zebrafish.” *Developmental Dynamics*. https://doi.org/10.1002/aja.1002030302.

Klaassen, Lauw J., Wim De Graaff, Jorrit B. Van Asselt, Jan Klooster, and Maarten Kamermans. 2016. “Specific Connectivity between Photoreceptors and Horizontal Cells in the Zebrafish Retina.” *Journal of Neurophysiology*. https://doi.org/10.1152/jn.00449.2016.

Klapoetke, Nathan C., Yasunobu Murata, Sung Soo Kim, Stefan R. Pulver, Amanda Birdsey-Benson, Yong Ku Cho, Tania K. Morimoto, et al. 2014. “Independent Optical Excitation of Distinct Neural Populations.” *Nature Methods*. https://doi.org/10.1038/nmeth.2836.

Kolb, Helga, Ralph Nelson, and Andrew Mariani. 1981. “Amacrine Cells, Bipolar Cells and Ganglion Cells of the Cat Retina: A Golgi Study.” *Vision Research*. https://doi.org/10.1016/0042-6989(81)90013-4.

Korenberg, Michael J., and Ken Ichi Naka. 1988. “White-Noise Analysis in Visual Neuroscience.” *Visual Neuroscience*. https://doi.org/10.1017/S0952523800001942.

Krauss, Andrea, and Christa Neumeyer. 2003. “Wavelength Dependence of the Optomotor Response in Zebrafish (Danio Rerio).” *Vision Research*. https://doi.org/10.1016/S0042-6989(03)00090-7.

KUFFLER, S. W. 1953. “Discharge Patterns and Functional Organization of Mammalian Retina.” *Journal of Neurophysiology*. https://doi.org/10.1152/jn.1953.16.1.37.

Lagnado, Leon, and Frank Schmitz. 2015. “Q.” *Annual Review of Vision Science*. https://doi.org/10.1146/annurev-vision-082114-035709.

Lamb, T. D. 1995. “Photoreceptor Spectral Sensitivities: Common Shape in the Long-Wavelength Region.” *Vision Research*. https://doi.org/10.1016/0042-6989(95)00114-F.

Lamb, Trevor D., Shaun P. Collin, and Edward N. Pugh. 2007. “Evolution of the Vertebrate Eye: Opsins, Photoreceptors, Retina and Eye Cup.” *Nature Reviews Neuroscience*. https://doi.org/10.1038/nrn2283.

Land, Michael F., and Dan-Eric Nilsson. 2013. *Animal Eyes*. *Animal Eyes*. https://doi.org/10.1093/acprof:oso/9780199581139.001.0001.

Lee, Barry B., Paul R. Martin, and Ulrike Grünert. 2010. “Retinal Connectivity and Primate Vision.” *Progress in Retinal and Eye Research*. https://doi.org/10.1016/j.preteyeres.2010.08.004.

Lee, Barry B. 2008. “The Evolution of Concepts of Color Vision.” *Neurociencias*.

Lewis, Alex, and Zhaoping Li. 2006. “Are Cone Sensitivities Determined by Natural Color Statistics?” *Journal of Vision*. https://doi.org/10.1167/6.3.8.

Li, Yong N., Jonathan I. Matsui, and John E. Dowling. 2009. “Specificity of the Horizontal Cell-Photoreceptor Connections in the Zebrafish (Danio Rerio) Retina.” *Journal of Comparative Neurology*. https://doi.org/10.1002/cne.22135.

Li, Yong N., Taro Tsujimura, Shoji Kawamura, and John E. Dowling. 2012. “Bipolar Cell-Photoreceptor Connectivity in the Zebrafish (Danio Rerio) Retina.” *Journal of Comparative Neurology* 520 (16): 3786–3802. https://doi.org/10.1002/cne.23168.

Loew, E. R., W. N. McFarland, E. L. Mills, and D. Hunter. 1993. “ A Chromatic Action Spectrum for Planktonic Predation by Juvenile Yellow Perch, Perca Flavescens .” *Canadian Journal of Zoology*. https://doi.org/10.1139/z93-053.

Loew, Ellis R., and William N. McFarland. 1990. “The Underwater Visual Environment.” In *The Visual System of Fish*. https://doi.org/10.1007/978-94-009-0411-8_1.

Lopes, Gonçalo, Niccolò Bonacchi, João Frazão, Joana P. Neto, Bassam V. Atallah, Sofia Soares, Luís Moreira, et al. 2015. “Bonsai: An Event-Based Framework for Processing and Controlling Data Streams.” *Frontiers in Neuroinformatics*. https://doi.org/10.3389/fninf.2015.00007.

Losey, G. S., T. W. Cronin, T. H. Goldsmith, D. Hyde, N. J. Marshall, and W. N. McFarland. 1999. “The UV Visual World of Fishes: A Review.” *Journal of Fish Biology*. https://doi.org/10.1006/jfbi.1998.0919.

Luehrmann, Martin, Fabio Cortesi, Karen L. Cheney, Fanny de Busserolles, and N. Justin Marshall. 2020. “Microhabitat Partitioning Correlates with Opsin Gene Expression in Coral Reef Cardinalfishes (Apogonidae).” *Functional Ecology*. https://doi.org/10.1111/1365-2435.13529.

Lythgoe, J. N. 1979. *The Ecology of Vision*. Clarendon Press.

Ma, Li Bo, and S. Wu. 2011. “Efficient Coding of Natural Images.” *Sheng Li Xue Bao : [Acta Physiologica Sinica]*.

MacLeod, Robert B., Ewald Hering, Leo M. Hurvich, and Dorothea Jamieson. 1967. “Outlines of a Theory of the Light Sense.” *The American Journal of Psychology*. https://doi.org/10.2307/1420566.

Maia Chagas, André. 2018. “Haves and Have Nots Must Find a Better Way: The Case for Open Scientific Hardware.” *PLoS Biology*. https://doi.org/10.1371/journal.pbio.3000014.

“Marine Optics By N.G. Jerlov Amsterdem: Elsevier Scientific Publishing Company, 1976. Xii,231 Pp. (Elsevier Oceanography Series, 14.) Price Dfl.77.00／$29.75.” 1978. *Journal of the Marine Biological Association of the United Kingdom*. https://doi.org/10.1017/s0025315400028277.

Marr, D., and E. Hildreth. 1980. “Theory of Edge Detection.” *Proceedings of the Royal Society of London - Biological Sciences*. https://doi.org/10.1098/rspb.1980.0020.

Masland, R. H. 2001. “The Fundamental Plan of the Retina.” *Nature Neuroscience*. https://doi.org/10.1038/nn0901-877.

Masland, Richard H. 2012a. “The Neuronal Organization of the Retina.” *Neuron*. https://doi.org/10.1016/j.neuron.2012.10.002.

———. 2012b. “The Neuronal Organization of the Retina.” *Neuron*. https://doi.org/10.1016/j.neuron.2012.10.002.

———. 2012c. “The Retina: An Approachable Part of the Brain. By John E. Dowling. Xviii + 355 Pp. Cambridge, MA: Harvard University Press (Belknap). 2012. $95.50 (Cloth).” *American Journal of Human Biology*. https://doi.org/10.1002/ajhb.22305.

Massey, Stephen C., and Dianna A. Redburn. 1987. “Transmitter Circuits in the Vertebrate Retina.” *Progress in Neurobiology*. https://doi.org/10.1016/0301-0082(87)90005-0.

Mathis, Alexander, Pranav Mamidanna, Kevin M. Cury, Taiga Abe, Venkatesh N. Murthy, Mackenzie Weygandt Mathis, and Matthias Bethge. 2018. “DeepLabCut: Markerless Pose Estimation of User-Defined Body Parts with Deep Learning.” *Nature Neuroscience*. https://doi.org/10.1038/s41593-018-0209-y.

Maxwell, James Clerk. 1857. “XVIII.— Experiments on Colour, as Perceived by the Eye, with Remarks on Colour-Blindness.” *Transactions of the Royal Society of Edinburgh*. https://doi.org/10.1017/S0080456800032117.

———. 1860. “On the Theory of Compound Colours with Reference to Mixtures of Blue and Yellow Light.” In *The Scientific Papers of James Clerk Maxwell*, 243–45. https://doi.org/10.1017/cbo9780511698095.016.

Mayer, Melanie J., and John E. Dowling. 1988. “The Retina: An Approachable Part of the Brain.” *The American Journal of Psychology*. https://doi.org/10.2307/1423238.

Mollon, J. D. 1989. “‘Tho’ She Kneel’d in That Place Where They Grew...’. The Uses and Origins of Primate Colour Vision.” *Journal of Experimental Biology*.

Morin, Andrew, Jennifer Urban, and Piotr Sliz. 2012. “A Quick Guide to Software Licensing for the Scientist-Programmer.” *PLoS Computational Biology*. https://doi.org/10.1371/journal.pcbi.1002598.

Moritoh, Satoru, Yusuke Komatsu, Tetsuo Yamamori, and Amane Koizumi. 2013. “Diversity of Retinal Ganglion Cells Identified by Transient GFP Transfection in Organotypic Tissue Culture of Adult Marmoset Monkey Retina.” *PLoS ONE*. https://doi.org/10.1371/journal.pone.0054667.

Munz, F.W., and W.N. McFarland. 1977. “Evolutionary Adaptations of Fishes to the Photic Environment.” In . https://doi.org/10.1007/978-3-642-66468-7_4.

Nath, Tanmay, Alexander Mathis, An Chi Chen, Amir Patel, Matthias Bethge, and Mackenzie Weygandt Mathis. 2019. “Using DeepLabCut for 3D Markerless Pose Estimation across Species and Behaviors.” *Nature Protocols*. https://doi.org/10.1038/s41596-019-0176-0.

Nava, Saúl S., Stephen An, and Tyler Hamil. 2011. “Visual Detection of UV Cues by Adult

Zebrafish (Danio Rerio).” *Journal of Vision*. https://doi.org/10.1167/11.6.2.

Neri, Peter. 2015. “The Elementary Operations of Human Vision Are Not Reducible to Template-Matching.” *PLoS Computational Biology*. https://doi.org/10.1371/journal.pcbi.1004499.

Nevala, N. E., and T. Baden. 2019. “A Low-Cost Hyperspectral Scanner for Natural Imaging and the Study of Animal Colour Vision above and under Water.” *Scientific Reports*. https://doi.org/10.1038/s41598-019-47220-6.

Nevin, Linda M., Michael R. Taylor, and Herwig Baier. 2008. “Hardwiring of Fine Synaptic Layers in the Zebrafish Visual Pathway.” *Neural Development* 3 (1). https://doi.org/10.1186/1749-8104-3-36.

Nilsson, Dan E., and Jochen Smolka. 2021. “Quantifying Biologically Essential Aspects of Environmental Light.” *Journal of the Royal Society Interface*. https://doi.org/10.1098/rsif.2021.0184.

Novales Flamarique, Iñigo. 2016. “Diminished Foraging Performance of a Mutant Zebrafish with Reduced Population of Ultraviolet Cones.” *Proceedings of the Royal Society B: Biological Sciences* 283 (1826): 20160058. https://doi.org/10.1098/rspb.2016.0058.

Olshausen, B. A., and D. J. Field. 1996. “Natural Image Statistics and Efficient Coding.” *Network: Computation in Neural Systems*. https://doi.org/10.1088/0954-898X_7_2_014.

Osorio, D., and M. Vorobyev. 2008. “A Review of the Evolution of Animal Colour Vision and Visual Communication Signals.” *Vision Research* 48 (20): 2042–51. https://doi.org/10.1016/j.visres.2008.06.018.

Patterson, Bradley W., Aliza O. Abraham, Malcolm A. MacIver, and David L. McLean. 2013. “Visually Guided Gradation of Prey Capture Movements in Larval Zebrafish.” *Journal of Experimental Biology*. https://doi.org/10.1242/jeb.087742.

Pearce, Joshua M. 2012. “Building Research Equipment with Free, Open-Source Hardware.” *Science*. https://doi.org/10.1126/science.1228183.

———. 2013. *Open-Source Lab: How to Build Your Own Hardware and Reduce Research Costs*. *Open-Source Lab: How to Build Your Own Hardware and Reduce Research Costs*. https://doi.org/10.1016/C2012-0-07249-3.

Pologruto, Thomas A., Bernardo L. Sabatini, and Karel Svoboda. 2003. “ScanImage: Flexible Software for Operating Laser Scanning Microscopes.” *BioMedical Engineering Online*. https://doi.org/10.1186/1475-925X-2-13.

Portugues, Ruben, and Florian Engert. 2009. “The Neural Basis of Visual Behaviors in the Larval Zebrafish.” *Current Opinion in Neurobiology*. https://doi.org/10.1016/j.conb.2009.10.007.

Powell, Alison. 2012. “Democratizing Production through Open Source Knowledge: From Open Software to Open Hardware.” *Media, Culture & Society* 34 (6): 691–708. https://doi.org/10.1177/0163443712449497.

Powell, Alison B. 2015. “Open Culture and Innovation: Integrating Knowledge across Boundaries.” *Media, Culture & Society* 37 (3): 376–93. https://doi.org/10.1177/0163443714567169.

Powell, Samuel B., Laurie J. Mitchell, Amelia M. Phelan, Fabio Cortesi, Justin Marshall, and Karen L. Cheney. 2021. “A Five-Channel LED Display to Investigate UV Perception.” *Methods in Ecology and Evolution*. https://doi.org/10.1111/2041-210X.13555.

Prieto-Godino, Lucia L., Soeren Diegelmann, and Michael Bate. 2012. “Embryonic Origin of Olfactory Circuitry in Drosophila: Contact and Activity-Mediated Interactions Pattern Connectivity in the Antennal Lobe.” *PLoS Biology*. https://doi.org/10.1371/journal.pbio.1001400.

Puller, C., E. Ivanova, T. Euler, S. Haverkamp, and T. Schubert. 2013. “OFF Bipolar Cells Express Distinct Types of Dendritic Glutamate Receptors in the Mouse Retina.” *Neuroscience*. https://doi.org/10.1016/j.neuroscience.2013.03.054.

Purves, Dale, George J. Augustine, David Fitzpatrik, William C. Hall, Anthony-Samuel Lamantia, James O. Mcnamara, and S. Mark Willians. 2004. *Purves Neuroscience*. *Neuroscience. 3nd Edition.*

Radonjić, Ana, Nicolas P Cottaris, and David H Brainard. 2015. “Color Constancy in a Naturalistic Goal-Directed Task.” *Journal of Vision* 15 (13): 3.1-3.21. https://doi.org/10.1167/15.13.3.doi.

Rajan, Kanaka, and William Bialek. 2013. “Maximally Informative ‘Stimulus Energies’ in the Analysis of Neural Responses to Natural Signals.” *PLoS ONE*. https://doi.org/10.1371/journal.pone.0071959.

Ramón y Cajal, Santiago. 1892. “La Rétine Des Vertébrés.” *La Cellule*.

Renninger, Sabine L., Helia B. Schonthaler, Stephan C.F. Neuhauss, and Ralf Dahm. 2011. “Investigating the Genetics of Visual Processing, Function and Behaviour in Zebrafish.” *Neurogenetics*. https://doi.org/10.1007/s10048-011-0273-x.

Robinson, Judith, Ellen A. Schmitt, Ferenc I. Hárosi, Richard J. Reece, and John E. Dowling. 1993. “Zebrafish Ultraviolet Visual Pigment: Absorption Spectrum, Sequence, and Localization.” *Proceedings of the National Academy of Sciences of the United States of America*. https://doi.org/10.1073/pnas.90.13.6009.

Ruderman, Daniel L., Thomas W. Cronin, and Chuan-Chin Chiao. 1998. “Statistics of Cone Responses to Natural Images: Implications for Visual Coding.” *Journal of the Optical Society of America A*. https://doi.org/10.1364/josaa.15.002036.

Rushton, W. A.H. 1972. “Review Lecture. Pigments and Signals in Colour Vision.” *The Journal of Physiology*. https://doi.org/10.1113/jphysiol.1972.sp009719.

Sabbah, Shai, John A. Gemmer, Ananya Bhatia-Lin, Gabrielle Manoff, Gabriel Castro, Jesse K. Siegel, Nathan Jeffery, and David M. Berson. 2017. “A Retinal Code for Motion along the Gravitational and Body Axes.” *Nature*. https://doi.org/10.1038/nature22818.

Sakai, H. M. 1992. “White-Noise Analysis in Neurophysiology.” *Physiological Reviews*. https://doi.org/10.1152/physrev.1992.72.2.491.

Sánchez-González, Rosario, Ángel Porteros, Adrián Santos-Ledo, Juan Lara, Almudena Velasco, José Aijón, and Rosario Arévalo. 2009. “Developmental Expression Patterns of Acetylcholinesterase and Choline Acetyltransferase in Zebrafish Retina.” *European Journal of Anatomy*.

Schaerer, Stephanie, and Christa Neumeyer. 1996. “Motion Detection in Goldfish Investigated with the Optomotor Response Is ‘Color Blind.’” *Vision Research*. https://doi.org/10.1016/S0042-6989(96)00149-6.

Schlieper, Carl. 1927. “Farbensinn Der Tiere Und Optomotorische Reaktionen.” *Zeitschrift Für Vergleichende Physiologie*. https://doi.org/10.1007/BF00710443.

Schmitt, Ellen A., and John E. Dowling. 1994. “Early-eye Morphogenesis in the Zebrafish, Brachydanio Rerio.” *Journal of Comparative Neurology*. https://doi.org/10.1002/cne.903440404.

———. 1999. “Early Retinal Development in the Zebrafish, Danio Rerio: Light and Electron Microscopic Analyses.” *Journal of Comparative Neurology*. https://doi.org/10.1002/(SICI)1096-9861(19990222)404:4<515::AID-CNE8>3.0.CO;2-A.

Schmitz, Frank. 2009. “The Making of Synaptic Ribbons: How They Are Built and What They Do.” *Neuroscientist*. https://doi.org/10.1177/1073858409340253.

Schmitz, Frank, Andreas Königstorfer, and Thomas C. Südhof. 2000. “RIBEYE, a

Component of Synaptic Ribbons: A Protein's Journey through Evolution Provides Insight into Synaptic Ribbon Function." *Neuron*. https://doi.org/10.1016/S0896-6273(00)00159-8.

Semmelhack, Julia L., Joseph C. Donovan, Tod R. Thiele, Enrico Kuehn, Eva Laurell, and Herwig Baier. 2014. "A Dedicated Visual Pathway for Prey Detection in Larval Zebrafish." *ELife*. https://doi.org/10.7554/eLife.04878.

Sharpee, Tatyana, Nicole C. Rust, and William Bialek. 2003. "Maximally Informative Dimensions: Analyzing Neural Responses to Natural Signals." In *Advances in Neural Information Processing Systems*.

———. 2004. "Analyzing Neural Responses to Natural Signals: Maximally Informative Dimensions." *Neural Computation*. https://doi.org/10.1162/089976604322742010.

Sherry, David M., and Stephen Yazulla. 1993. "Goldfish Bipolar Cells and Axon Terminal Patterns: A Golgi Study." *Journal of Comparative Neurology*. https://doi.org/10.1002/cne.903290204.

Shimbo, Kiyoshi, Jun Ichi Toyoda, Hiroaki Kondo, and Toru Kujiraoka. 2000. "Color-Opponent Responses of Small and Giant Bipolar Cells in the Carp Retina." *Visual Neuroscience*. https://doi.org/10.1017/S0952523800174103.

Simoncelli, E. P., and B. A. Olshausen. 2001. "Natural Image Statistics and Neural Representation." *Annual Review of Neuroscience*. https://doi.org/10.1146/annurev.neuro.24.1.1193.

Stell, William K. 1967. "The Structure and Relationships of Horizontal Cells and Photoreceptor-bipolar Synaptic Complexes in Goldfish Retina." *American Journal of Anatomy* 121 (2): 401–23. https://doi.org/10.1002/aja.1001210213.

Stone, S., P. Witkovsky, and M. Schutte. 1990. "A Chromatic Horizontal Cell in the Xenopus Retina: Intracellular Staining and Synaptic Pharmacology." *Journal of Neurophysiology*. https://doi.org/10.1152/jn.1990.64.6.1683.

Surridge, Alison K., Daniel Osorio, and Nicholas I. Mundy. 2003. "Evolution and Selection of Trichromatic Vision in Primates." *Trends in Ecology and Evolution*. https://doi.org/10.1016/S0169-5347(03)00012-0.

Svaetichin, Gunnar, and Edward F. MacNichol. 1958. "RETINAL MECHANISMS FOR CHROMATIC AND ACHROMATIC VISION." *Annals of the New York Academy of Sciences*. https://doi.org/10.1111/j.1749-6632.1958.tb39560.x.

Szatko, Klaudia P., Maria M. Korympidou, Yanli Ran, Philipp Berens, Deniz Dalkara, Timm Schubert, Thomas Euler, and Katrin Franke. 2020. “Neural Circuits in the Mouse Retina Support Color Vision in the Upper Visual Field.” *Nature Communications*. https://doi.org/10.1038/s41467-020-17113-8.

Tan, Zhongchao, Wenzhi Sun, Tsai Wen Chen, Douglas Kim, and Na Ji. 2015. “Neuronal Representation of Ultraviolet Visual Stimuli in Mouse Primary Visual Cortex.” *Scientific Reports*. https://doi.org/10.1038/srep12597.

Toyoda, Jun-Ichi -I, Takehiko Saito, and Hiroaki Kondo. 1978. “Three Types of Horizontal Cells in the Stingray Retina: Their Morphology and Physiology.” *Journal of Comparative Neurology*. https://doi.org/10.1002/cne.901790308.

Trivedi, Chintan A., and Johann H. Bollmann. 2013. “Visually Driven Chaining of Elementary Swim Patterns into a Goal-Directed Motor Sequence: A Virtual Reality Study of Zebrafish Prey Capture.” *Frontiers in Neural Circuits*. https://doi.org/10.3389/fncir.2013.00086.

Twig, Gilad, Hanna Levy, and Ido Perlman. 2003. “Color Opponency in Horizontal Cells of the Vertebrate Retina.” *Progress in Retinal and Eye Research*. https://doi.org/10.1016/S1350-9462(02)00045-9.

Walls, G. L. 1982. “PsycNET_Export.” *The Vertebrate Eye and Its Adaptive Radiation*. https://doi.org/10.5962/bhl.title.7369.

Warrant, Eric, Sönke Johnsen, and Dan-Eric Nilsson. 2020. “Light and Visual Environments.” In *Reference Module in Neuroscience and Biobehavioral Psychology*. Elsevier. https://doi.org/10.1016/B978-0-12-805408-6.00002-6.

Warwick, Rebekah A., Nathali Kaushansky, Nimrod Sarid, Amir Golan, and Michal Rivlin-Etzion. 2018. “Inhomogeneous Encoding of the Visual Field in the Mouse Retina.” *Current Biology*. https://doi.org/10.1016/j.cub.2018.01.016.

Wässle, Heinz. 2004. “Parallel Processing in the Mammalian Retina.” *Nature Reviews Neuroscience*. https://doi.org/10.1038/nrn1497.

Wässle, Heinz, Christian Puller, Frank Müller, and Silke Haverkamp. 2009. “Cone Contacts, Mosaics, and Territories of Bipolar Cells in the Mouse Retina.” *Journal of Neuroscience*. https://doi.org/10.1523/JNEUROSCI.4442-08.2009.

Werblin, F. S., and J. E. Dowling. 1969. “Organization of the Retina of the Mudpuppy, Necturus Maculosus. II. Intracellular Recording.” *Journal of Neurophysiology*.

https://doi.org/10.1152/jn.1969.32.3.339.

Witzel, Christoph, and Karl Gegenfurtner. 2015. “Chromatic Contrast Sensitivity.” In *Encyclopedia of Color Science and Technology*. https://doi.org/10.1007/978-3-642-27851-8_17-1.

Wong, Kwoon Y., Alan R. Adolph, and John E. Dowling. 2005. “Retinal Bipolar Cell Input Mechanisms in Giant Danio. I. Electroretinographic Analysis.” *Journal of Neurophysiology*. https://doi.org/10.1152/jn.00259.2004.

Wu, Samuel M., Fan Gao, and Bruce R. Maple. 2000. “Functional Architecture of Synapses in the Inner Retina: Segregation of Visual Signals by Stratification of Bipolar Cell Axon Terminals.” *Journal of Neuroscience*. https://doi.org/10.1523/jneurosci.20-12-04462.2000.

Xin, Daiyan, and Stewart A. Bloomfield. 1999. “Dark- and Light-Induced Changes in Coupling between Horizontal Cells in Mammalian Retina.” *Journal of Comparative Neurology*. https://doi.org/10.1002/(SICI)1096-9861(19990301)405:1<75::AID-CNE6>3.0.CO;2-D.

Yoshimatsu, Takeshi, Cornelius Schröder, Noora E. Nevala, Philipp Berens, and Tom Baden. 2020. “Fovea-like Photoreceptor Specializations Underlie Single UV Cone Driven Prey-Capture Behavior in Zebrafish.” *Neuron*. https://doi.org/10.1016/j.neuron.2020.04.021.

Young, Heather M., and David I. Vaney. 1991. “Rod-signal Interneurons in the Rabbit Retina: 1. Rod Bipolar Cells.” *Journal of Comparative Neurology*. https://doi.org/10.1002/cne.903100202.

Young, Thomas. 1802. “On the Theory of Light and Colours.” *Phil. Trans. R. Soc. Lond.* https://doi.org/10.1098/rstl.1802.0004.

Zhang, Ai Jun, and Samuel M. Wu. 2009. “Receptive Fields of Retinal Bipolar Cells Are Mediated by Heterogeneous Synaptic Circuitry.” *Journal of Neuroscience*. https://doi.org/10.1523/JNEUROSCI.4984-08.2009.

Zhao, Xiao Feng, Staale Ellingsen, and Anders Fjose. 2009. “Labelling and Targeted Ablation of Specific Bipolar Cell Types in the Zebrafish Retina.” *BMC Neuroscience* 10: 107. https://doi.org/10.1186/1471-2202-10-107.

Zhaoping, Li, and Li Zhaoping. 2014. “The Efficient Coding Principle.” In *Understanding Vision*. https://doi.org/10.1093/acprof:oso/9780199564668.003.0003.

Zhou, Mingyi, John Bear, Paul A. Roberts, Filip K. Janiak, Julie Semmelhack, Takeshi Yoshimatsu, and Tom Baden. 2020. “Zebrafish Retinal Ganglion Cells Asymmetrically Encode Spectral and Temporal Information across Visual Space.” *Current Biology*. https://doi.org/10.1016/j.cub.2020.05.055.

Zimmerman, Roger P., Edward H. Polley, and Richard L. Fortney. 1988. “Cell Birthdays and Rate of Differentiation of Ganglion and Horizontal Cells of the Developing Cat’s Retina.” *Journal of Comparative Neurology*. https://doi.org/10.1002/cne.902740108.

Zimmermann, M. J.Y., A. Maia Chagas, P. Bartel, S. Pop, L. L. Prieto-Godino, and T. Baden. 2020. “LED Zappelin’: An Open Source LED Controller for Arbitrary Spectrum Visual Stimulation and Optogenetics during 2-Photon Imaging.” *HardwareX*. https://doi.org/10.1016/j.ohx.2020.e00127.

Zimmermann, Maxime J.Y., Noora E. Nevala, Takeshi Yoshimatsu, Daniel Osorio, Dan Eric Nilsson, Philipp Berens, and Tom Baden. 2018. “Zebrafish Differentially Process Color across Visual Space to Match Natural Scenes.” *Current Biology*. https://doi.org/10.1016/j.cub.2018.04.075.

Appendix 1

Material and instruction manuals for the LED Zappelin' stimulator

As described in chapter 3, published as **LED Zappelin': An open source LED controller for arbitrary spectrum visual stimulation and optogenetics during 2-photon imaging.** Zimmermann MJY, Chagas AM, Bartel P, Pop S, Prieto Godino LL, Baden T. and documented on https://github.com/BadenLab/LED-Zappelin

In this appendix will be presented detailed instructions for the reproduction and operation of this stimulator. All electronics blueprints, PCB gerbers, 3D-design SCAD files, etc. can be found on the online repository where they are regularly updated.

7.1 – Bill of materials

The stimulator consists of an ESP32 micro-controller (Adafruit ESP32 feather, built around the ESP32 system on a chip, Espressif), an LED driver (Adafruit TLC5947, built around the TLC5947 chip, Texas instruments), and common off-the shelf electronics components. Designed around a custom-built printed circuit board (PCB), the stimulator assembly is intuitive and does not require previous electronics nor soldering experience. The total cost for electronic parts is currently below $100.

Description	Component	Number	Unit price	Total	Source of materials
PCBs	Stimulator + Potentiometer PCBs	1 of each	~$10	~$20	JLCPCB
Microcontroller	Adafruit Huzzah32 – ESP32 Feather	1	$19.95	$19.95	Adafruit
LED Driver	Adafruit TLC5947	1	$14.95	$14.95	Adafruit
BNC coaxial Connectors	Right angle BNC jacks	2	$2.5	$5	RS-components
2-way JST connector	2-way JST female connector housing	nLED	$0.5	nLED x $0.5	RS-components
2-way JST PCB header	2-way JST male connector PCB header	nLED	$0.25	nLED x $0.25	RS-components
3-way JST connector	3-way JST female connector housing	1	$0.5	$0.5	RS-components
3-way JST PCB header	3-way JST male connector PCB header	1	$0.5	$0.5	RS-components
Trimmer potentiometer	Multi-turn 10 kΩ through hole trimmer potentiometer	nLED	$1.15	nLED x $1.15	RS-components
Voltage Divider	220 Ω through hole resistor	1	$0.15	$0.15	RS-components
Voltage Divider	470 Ω through hole resistor	1	$0.15	$0.15	RS-components
Signal Inverter	150 Ω through hole resistor	1	$0.15	$0.15	RS-components
Signal Inverter	1 k Ω through hole resistor	1	$0.13	$0.13	RS-components
Power plug	2.1 mm right angle DC socket	1	$1.3	$1.3	RS-components
PCB sockets	2.54 mm pitch 16-way 1 row straight PCB socket	6	$3.8	$22.8	RS-components
Rocker LED switch	3-pin LED Rocker ON/OFF SPST switch	1	$5	$5	RS-components

Total cost for 4 stimulation LEDs and 4 proxy LEDs stimulator	$105.78

Table 7.1 | Stimulator electronics component BoM

LEDs are arranged in an optical cage system and positioned at an equal distance form the projection plane in order to share the same focus plane. Their lights are filtered and combined through filters and dichroic mirrors. To increase the design flexibility and reduce the overall cost, 3D printed parts are used to hold and orientate optical components (Fig 7.4). The total cost for the optical components necessary for the construction of the tetrachromatic stimulator described in Chapter 3 is around $3500.

Description	Component	Number	Unit price	Total	Source of materials
Red LED	B5B-434-TY	1	~$5	~$5	Roithner
Green LED	RLS-5B475-S	1	~$5	~$5	Roithner
Blue LED	VL415-5-15	1	~$5	~$5	Roithner
UV LED	XSL-365-5E	1	~$5	~$5	Roithner
Red LED filter	FF01-586/20 BrightLine HC	1	$394	$394	AHF
Green LED filter	ET 480/40	1	$403	$403	AHF
Blue LED filter	ET 420/40	1	$406	$406	AHF
UV LED filter	FF01-370/36 BrightLine HC	1	$394	$394	AHF
U/RGB Beamsplitter	T 400 LP	1	$263	$263	AHF
B/RG Beamsplitter	T 450I LPXR	1	$332	$332	AHF
G/R Beamsplitter	T 560 LPXR	1	$263	$263	AHF
50mm lens achromatic doublet	ACA254-050-A	1	$524	$524	ThorLabs
Cage System Right-Angle Adapter	LCP30	3	$44	$132	ThorLabs
Cage Plate Adapter	LCP02/M	2	$42	$84	ThorLabs
Cage Plate	CP02T/M	4	$23	$92	ThorLabs

Assembly Rod	ER8	4	$12	$46	ThorLabs
Assembly Rod	ER6	4	$9	$33	ThorLabs
Assembly Rod	ER4	4	$7	$27	ThorLabs
Assembly Rod	ER2	4	$6	$24	ThorLabs
Assembly Rod	ER1	4	$5	$20	ThorLabs
Mounting post	P10	1	$75	$75	ThorLabs
Base adapter	PB4	1	$14	$14	ThorLabs
Post clamp	PH100/M	1	$10	$10	
Cage clamp	CH1560/M	1	$92	$92	ThorLabs
Total cost for 4 stimulation LEDs				$3,648	

Table 7.2| Stimulator optical component BoM

7.2 – Build instructions

Two PCBs are required for the stimulator construction, one that holds all electronics components necessary for the stimulator functions, a second dedicated to LED channels that incorporates 10 kΩ multi-turn trimmer potentiometer for fine tuning the forward voltage each LED is receiving. The later board comes in different version to fit the user need for LED channel numbers. Also to further ease the reproduction of this stimulation system, the project was uploaded on the ready-to-order electronic design platform for open hardware projects: https://kitspace.org/, a PCB repository where all boards and components for them can be selected from local retailers and put in a “shopping cart” whit one click.

7.2.1 – Soldering the custom-designed PCB

Two options are available for either the Arduino Nano (inner rows, no external line-synch option) or the ESP32 (outer rows, full stimulator for 2-photon coupling). There is no need to solder more Japan Solderless Terminal (JST) pins beyond the number of LEDs required. On the right side of the board, the power plug and the £-way JST header must be soldered into their respective sockets.

The stimulator PCB also incorporates a signal inverter for inverting the *blanking signal* polarity (cf. Chapter 3) which can be enabled by a jumper (Fig 3.4). It is implemented by a logical NOT gate consisting of an NPN transistor (2N5089) collecting a constant 5V signal from the microcontroller, after passing a pull-down resistor of 150 Ω, which is connected to the *blanking* channel and emitting to the ground when the base receive a 5V signal from the setup *blanking signal* and its

associated 1 kΩ resistor. The overall effect will invert the *blanking signal* allowing the use of the device on any setup. When the jumper is placed on the upper position, LEDs are switched off when the *blanking signal* is LOW. ScanM users would instead need to place the jumper on the lower position (through the signal inverter) to turn off the LEDs when the *blanking signal* I HIGH.

A second jumper selects a voltage divider, allowing the use of a 5V or 3.3V power supply for the two possible microcontrollers respectively Arduino Nano and ESP32 which possesses two distinct current logic. IMPORTANT: Do not send 5 V signals to the ESP32. Since most TTL devices use on data acquisition systems deliver 5V pulses, a 220 Ω and a 470 Ω resistors were selected to bring an expected 5 V signal to a 3.3 V input. Depending on the voltage range of the *blanking signal*, these resistors may need to be adjusted according to Ohm's law: V1 + V2 = I*(R1+R2).

PCBs were designed on KiCad 5.0.0 (release build)

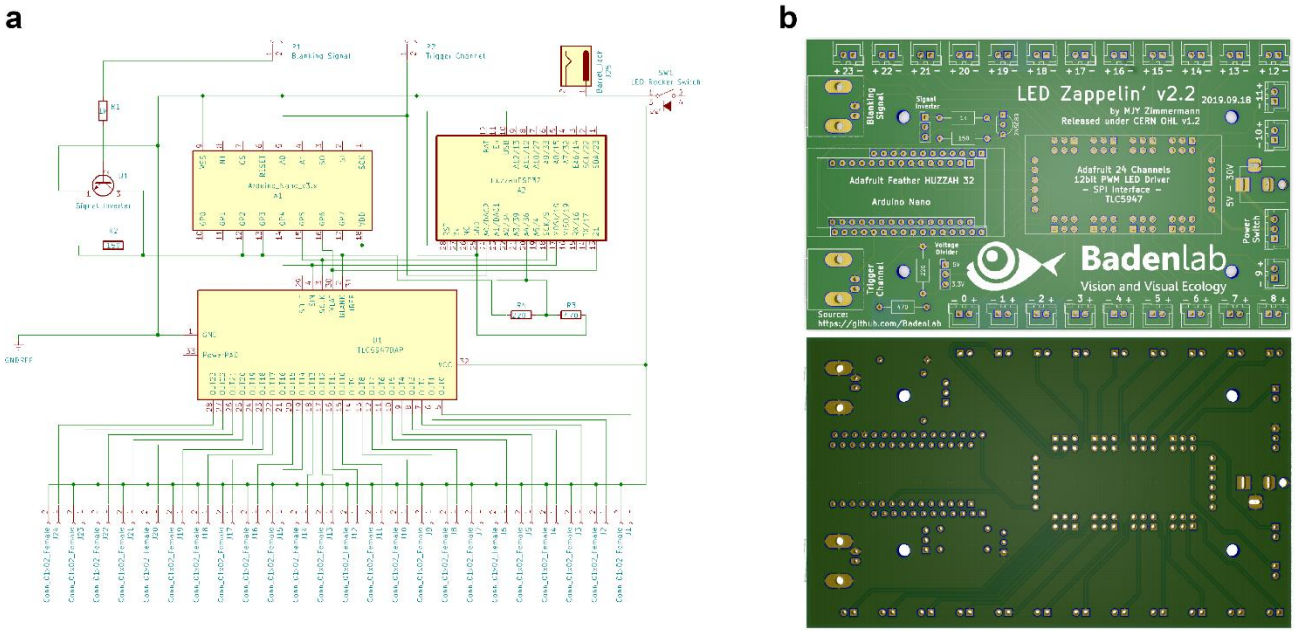

Figure 7.1 | Stimulator PCB. a) Schematic capture rendering for the stimulator PCB. **b)** Rendering of the PCB as generated from gerber files which can be found at: https://kitspace.org/boards/github.com/badenlab/led-zappelin/pcb/stimulator/

The Adafruit TLC5947 LED driver is configured by default to a current output level of 15 mA per channel, which is safe for nearly any standard LED. However, it is

possible to operate at different currents by replacing the on-board resistor with a new through hole resistor. The driver can deliver up to 30 mA per channel (described in detail on the manufacturer's datasheet: https://cdn-shop.adafruit.com/datasheets/tlc5947.pdf).

7.2.2 – Mounting the potentiometers

To finely adjust each LED's peak power, multiple-turn trimmer potentiometer were added to the design. To mount them, one simple solution would be to manufacture the appropriate custom PCB (4 versions were provided for different numbers of channels: 4, 8, 16, 24). These extra PCBs fit tightly into the 3D-printed box. LEDs should be connected to the potentiometer in series as shown in Fig 7.2. All gerber files can be found on https://kitspace.org/

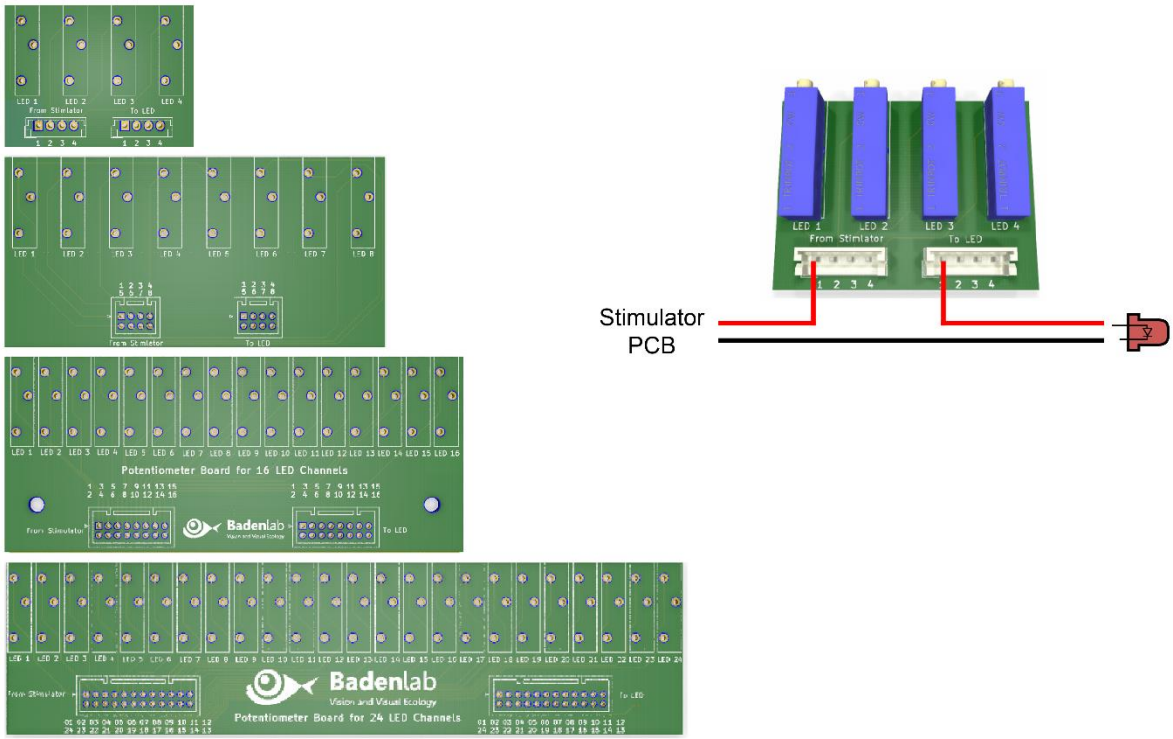

Figure 7.2 | Potentiometer mount PCBs. a) Rendering of all four PCB options available and wiring schematics between the stimulator and the LEDs.

7.2.3 - Printing the Stimulator Box

We used OpenSCAD (freely available at www.openscad.org) to design the stimulator enclosure. The tolerance of the printer can be adjusted in the “USER Parameters” section of the script (tol = 0.1 mm by default, suitable for a reasonably well-calibrated Prusa i3 MK3 or Ultimaker 2). Each component can be displayed/designed individually in the “switches” section. Variables such as LED number (4 by default) and the potentiometer board dimensions can be adjusted in the “component parameters” section.

Default STL files can also be found on the repository and printed directly (4 stimulation LEDs + 4 proxy LEDs).

The PCB is mounted by adding 50mm M3 screws from the top via fitting holes in the stacking parts. The potentiometer board is fitted to the “back” part of the box, with trimmers fitting to their respective holes (Fig. 7.3).

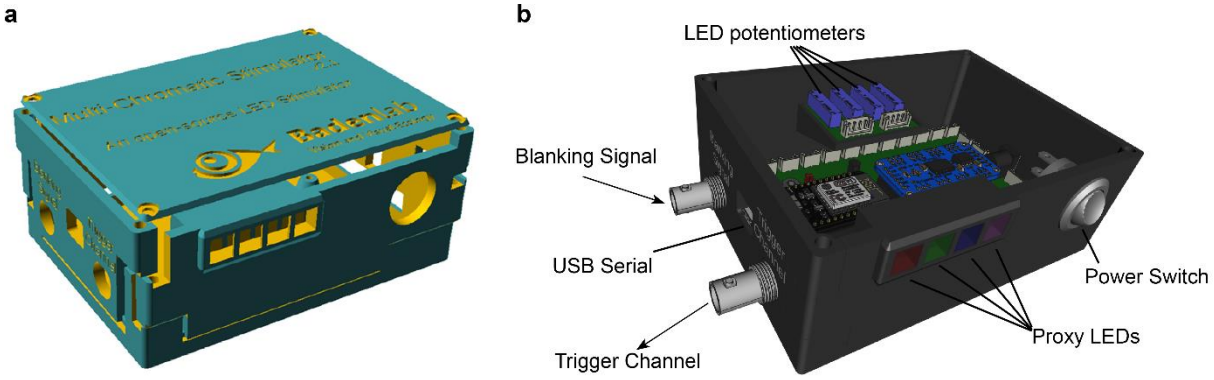

Figure 7.3 | Stimulator box. a. Rendering of the stimulator box 3D files set here by default for 4 LED channels and 4 proxy LEDs. **b.** Rendering of the fully mounted stimulator with all PCBs and components tightly fitting their respective space.

7.2.4 - Mounting the proxy LEDs

The proxy LEDs provide convenient visualisation of the stimulus state for the experimenter. If this option is selected, 3 mm LEDs should be mounted at the back of the LED holder using 3 mm LED mounts and connected directly to their channel pins on the stimulator board (by default channels 5, 6, 7 & 8). As the LEDs are directly connected to an LED driver, no resistors are needed. Take note of their polarity (long LED leg should be connected to pin +). For aesthetics, cuttings of Teflon sheet or white paper (e.g.) can be placed in the LED holder slot to diffuse the LED light.

7.2.5 - Mounting the stimulation LEDs

Each stimulation LED must be connected to its respective channel, taking note of their polarity (long LED leg should be connected to the positive pin).

For our visual stimulation setup, we combined all LED light sources into one beam which is projected through the objective to our model retina. We therefore constructed an optical cage system using a mixture of Thorlabs parts and 3D-printed objects to hold all filters and dichroic mirrors (Fig. 7.4a). This LED cage system was also used for the spatial stimulator described in chapter 4.

For the optogenetics experiment we 3D-designed arenas where the sample sits, surrounded by four LEDs (Fig. 7.4c-d).

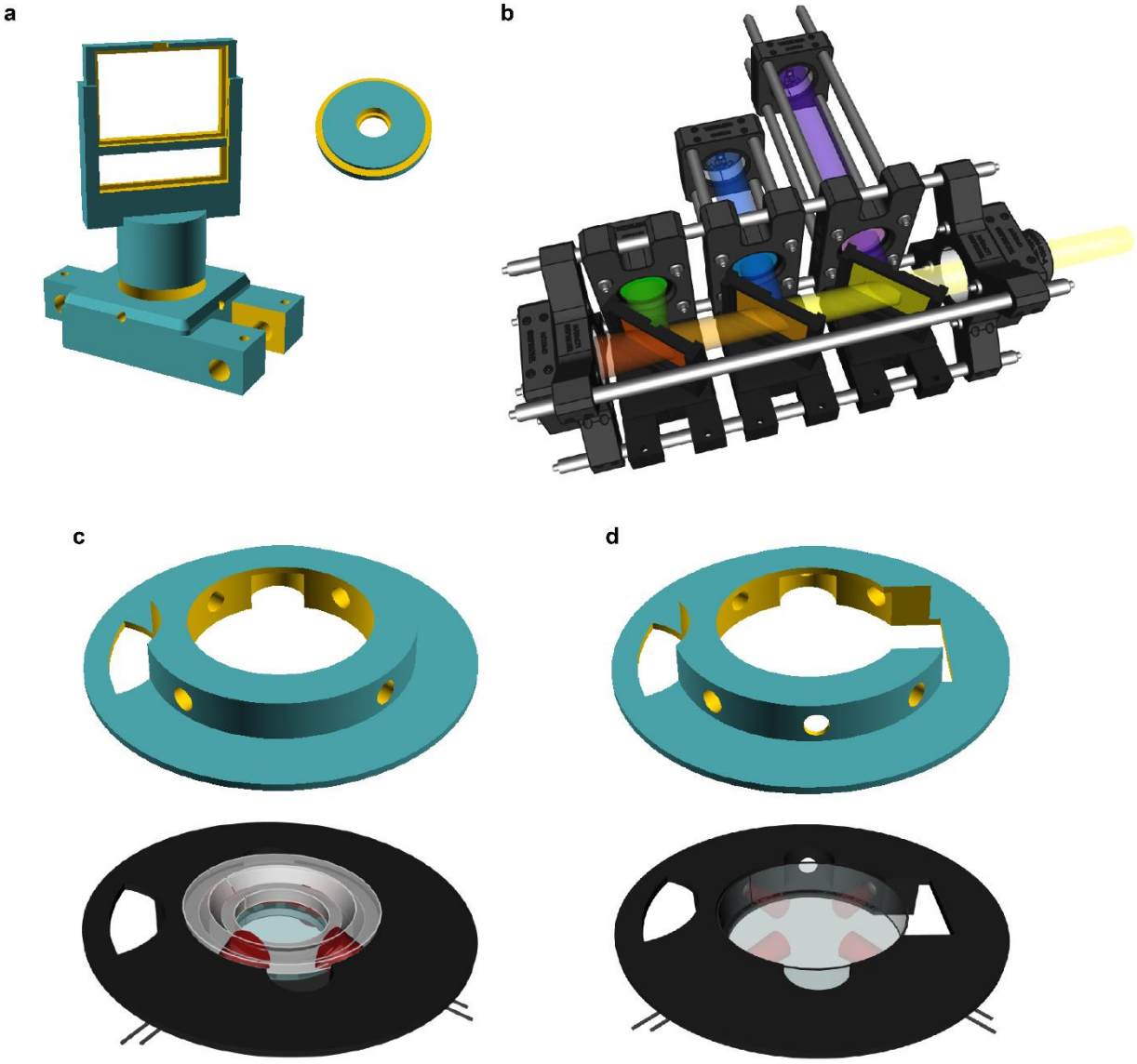

Figure 7.4 | 3D-printed illumination systems. a. SCAD files for adapting 5mm LEDs and dichroic mirrors to standard 30mm optomechanical system. **b.** Rendering of the LED illumination system for the visual experiment. **c.** For optogenetics experiments, we designed a mounting platform that holds four

5mm LEDs and can fit a RC-40HP chamber (SmartEphys, Warner Instrument). **d.** Same as **c.** but designed to fit a small petri dish (ø 35mm) lid.

7.2.6 - Connecting the stimulator to LEDs, the microscope's DAQ and a computer

The stimulator can be externally powered anywhere between 5-30 V via the power port. Since the TLC5947 is a constant current LED driver, the voltage selection is not critical, however it should be slightly higher than the LED forward voltage (cf. LED driver datasheet). If desired, multiple LEDs can be connected to the same channel, however in this case the voltage supply must be adjusted accordingly (cf. LED driver datasheet).

For the standard line-synched stimulator version with an ESP32, a line-synched 5V TTL blanking signal BNC must be fed into the stimulator from the microscope's DAQ (if the TTL is different from 5V, this can still be accepted provided the associated resistor is changed accordingly – see soldering paragraph). Note: Since for the default ESP32 version the blanking signal is used as the external clock, the stimulator will not execute any stimuli without it. If such line-synching is not required, consult the "simple" non-synchronised version that can be used with a simple Arduino Nano.

If required, connect the output trigger channel to the microscope's DAQ. This signal generated by the stimulator by default sends a 3.3V pulse (if ESP32 is used, 5V for Arduino Nano) once at the start of the stimulus and then again, every 1,000 ms (1 Hz exactly). The trigger signal can for example be used to time-align acquired imaging data with the stimulus in postprocessing.

Finally, the board is connected to a computer via USB (micro USB for ESP32, mini USB for Arduino Nano).

7.3 – Operation instructions

7.3.1 - Programming the ESP32 (or Arduino) on Windows systems

1- Download and install Arduino environment on the computer (www.arduino.org).

2- To use the ESP32, in addition:

a. Install the latest SiLabs CP2104 driver (https://www.silabs.com/products/development-tools/software/usb-to-uart-bridge-vcp-drivers).

b. Follow the installation instructions from the Espressif repository (https://github.com/espressif/arduino-esp32/blob/master/docs/arduino-ide/boards_manager.md).

3- Install the TLC5947 library

a. Start Arduino and from the “Sketch” tab, select “Include Library” and open “Manage Libraries”

b. From the search bar enter “TLC5947”

c. Select and install the library

4- Open the Arduino script (2 versions available on the repository: *“2Photon_LED_Stimulator”* and “*Simple_LED_Stimulator”*, the second one being a simplified version of the first, independent of an external *blanking signal* input).

5- From the “Tools” tab:

a. For the ESP32:

i. Select from “Boards” the “Adafruit ESP32 Feather”.

ii. From “Upload Speed”, select 921,600 (baud rate).

iii. From “Flash Frequency”, select 80 Hz.

iv. From “Port”, select the computer port to which the ESP32 is connected (if in doubt, unplug the board to see which ports are available, re-plug and observe which port is added). If the ESP is not recognised, check the driver installation (2a.), then check the micro USB cable (some USB cables do not work as not all their internal lines are connected).

b. For the Arduino Nano

i. Select from “Boards” the “Arduino Nano”

ii. From “Processor”, select “ATmega328P” (option “Old Bootloader” for Arduino clones or older Arduino versions – if in doubt, try both)

iii. From “Port”, select the computer port to which the Arduino is connected. If an Arduino clone is used, check that the proper driver is installed on the computer (consult its datasheet) and check the mini USB cable.

6- Compile and upload the code (clicking on the sideways arrow button on the top left).

7- The stimulator is ready to be used.

7.3.2 - Operating the stimulator

The code is organised in five parts:

Stimulus Parameters

The code is designed to iteratively loop a pre-programmed stimulus sequence after an initial one-off optional preadaptation period.

– The number of loops is determined by “nLoops”. The stimulus will stop after finishing the n^{th} loop.

– IMPORTANT, the number of entries within the arrays must be the same and manually entered in “nArrayEntries” (including the pre-adaptation at position 1, see below).

– The “Scan_Logic” parameter corresponds to the x-mirror scan period in ms (i.e. = 2.0 if line speed is 2 ms per line and scan rate is 500Hz). This value must be changed if a different scan logic is used. This value defines the tempo of the entire stimulus (each time a blanking signal is counted, the code advances by an internal time-counter of Scan_Logic in milliseconds).

– The “array_LED#” arrays correspond to the stimulus sequence for each LED number. Here the number of arrays must be adjusted to the number of stimulation LEDs. All array positions will be read in synchrony, based on the timing array detailed below. IMPORTANT: The first entry is not part of the to-be-looped stimulus sequence, but instead defines the LED’s brightness for the preadaptation period. Note also that the first trigger output will start with the second entry (= the first entry of the stimulation sequence). The value entered at each position is the light intensity where 0 corresponds to no light and 100 to maximal light intensity. The value entered must range between 0 and 100.

– The “array_Time” array corresponds to the duration of each entry in ms; the first entry being the pre-adaptation that will only be played at the start of the stimulus, the sequence will then loop starting at the second position.

For example, if…

nLoops = 3;

nArrayEntries = 3;

```
Scan_Logic = 1.0;
Array_LED1 = {50,100,0};
Array_LED2 = {50,0,100};
Array_Time = {5000,3000,3000};
```

…the resultant stimulus will start with 5 seconds of both LEDs being set to 50% intensity (preadaptation) and will thereafter switch back and forth every 3 seconds between 100% and 0% power for the two LEDs in antiphase, for 3 repetitions (Fig. 7.5). Alongside, it will output one trigger signal every 1 s (fixed to this interval by default) once the looped portion of the stimulus starts (e.g. for later aligning the stimulus to imaging data). Throughout, the LEDs will be line-synched to a 1 ms scan logic.

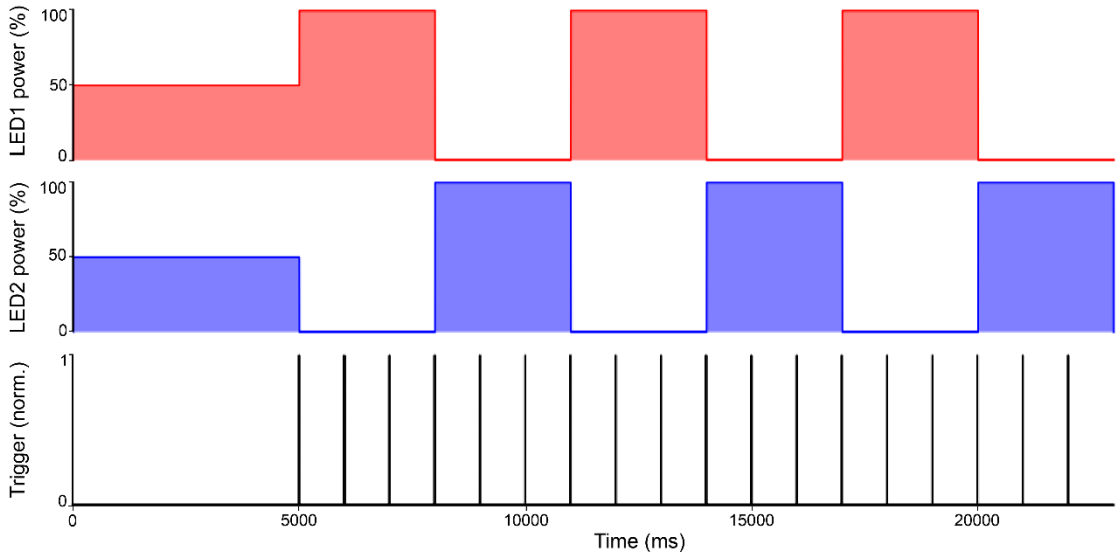

Figure 7.5 | Stimulus example. LED sequence (On/Off steps of light over three loops) described above, along with trigger recording.

Microcontroller Board Selection

Select if an ESP32 or an Arduino Nano is used.

Internal Definitions

This is the main definition part of the code which can be modified to:

- Add more LEDs than the 4 main and 4 proxy defined by default. (Global variables, the LED pins correspond to the pin number on the TLC5947).

- Adjust the trigger duration (25 ms by default).
- Adjust the trigger interval (1,000 ms by default).

Internal Methods

This is the main core of the code and should not be structurally changed (apart from adding more LEDs, as required).

Main Loop

This is where the serial user controls are defined. By default, when the serial monitor is open (magnifying glass on the top right corner in the Arduino IDE) and the baud rate at the bottom right of the window has been changed to 115,200. In this configuration, a manual command followed by pressing “enter” will trigger a stimulus:

By default:

- When “a + ENTER” is entered in the serial monitor, the stimulator will play the sequence with intensity scaled relative to the predefine “max1_LED#” powers (see below)
- When “b + ENTER” is entered, the same stimulus sequence will be played, but this time at the intensities defined by “max2_LED#” powers (see below)
- If “0 + ENTER” is entered during a stimulus sequence, all LEDs will be turned off and all loop counters will be reset.
- Further commands can easily be programmed by the user from the “Main Loop” part of the Arduino code.

It is important to note that the stimulation will only be played if a blanking signal is sent to the board.

7.3.3 - Calibrating the stimulator

Stimulation LEDs can be approximately brought into a desired intensity regime by adding a serial resistor to limit the current they receive. They can also be further calibrated within the code:

The TLC5947 is a 12-bit PWM grayscale driver, meaning that it offers up to 4,096 grey levels to adjust each LED power.

In the Arduino code there is a second tab called “LED_values” which hard-codes the maximum power an LED can get. Those values range from 0 (no current) to 4,095 (max current, 15 mA by default with potentiometer tuned all the way down).
In the default script we defined two distinct max values (max1 & max2) that can be called individually. The purpose here is to have the opportunity to use the same stimulus sequence at two different regimes of light intensities. More can be added manually by the user.
For the calibration, we suggest setting the max_LED# value to 4,095 (full power) and use successively a spectrometer and a power meter to adjust the LED brightness by finely turning the trimmer potentiometer at the back of the stimulator. As the LED output is linear relative to the values entered here (Fig. 3.2), any max_LED# value will be proportional to the LED power set up for the 4,095 value. The LED value (0-100%) entered in the stimulus sequence is linearly mapped to 0-max_LED#.

For a clear calibration procedure, an easy step by step Jupyter notebook manual is provided on the online repository: https://github.com/BadenLab/LED-Zappelin

Appendix 2

Material and instruction manuals for the Open Visual Stimulator

As described in chapter 4, published as: **An arbitrary-spectrum spatial visual stimulator for vision research.** Franke K, Chagas AM, Zhao Z, Zimmermann MJY, Bartel P, Qiu Y, Szatko K, Baden T, Euler T. and documented on https://github.com/BadenLab/Open-Visual-Stimulator

In this appendix will be presented detailed instructions for the reproduction and operation of this stimulator. All electronics blueprints, PCB gerbers, 3D-design SCAD files, etc. can be found on the online repository where they are regularly updated.

8.1 – Bill of materials

In the following paragraph will only be detailed the stimulator used for zebrafish experiments, described in Chapter 4 and consisting of four LED input dispatched on two LCrs.

Description	Component	Number	Unit price	Total	Source of materials
LightCrafter	0.45'' DLP Fiber couple E4500MKII Development module FC/PC	2	$2299	$4598	EKB Technologies Ltd.
PCBs	LCr add-on + LED driver board	1 of each	~$10	~$20	JLCPCB
LCr add-on PCB components (x2: RGB & UV units)					
BNC coaxial Connectors	Right angle BNC jacks	8	$2.5	$20	RS-components
LCr Connector	JST, PHD, 14 ways 2 rows	2	$1.25	$2.5	RS-components
Voltage regulator	LM2596 5V	2	$5	$5	RS-components
Inductor	33µH Neosid MA-Bs75	2	$0.25	$0.5	RS-components
Capacitor	680µF	2	$0.5	$1	RS-components
Capacitor	220µF	2	$0.5	$1	RS-components
Diode	Schottky 5A DO-201AD	2	$0.5	$1	RS-components
Resistor	1 k Ω	2	$0.15	$0.3	RS-components
Jumper connector	SSW-103-01-G-S	2	$0.1	$0.2	RS-components
AND gate	TC7S08F (T 2-Input AND Logic Gate, 5-Pin SSOP	12	$0.24	$2.6	RS-components
Signal inverter (NOT gate)	**TC7SH14F(F), 1 Schmitt Trigger Inverter, 5-Pin SSOP**	2	$0.24	$0.5	RS-components
LED driver PCB components (x4: R,G,B & UV channels)					
P-Channel MOSFET	**10 A, 20 V, 8-Pin SOIC ON Semiconductor FDS6575**	4	$1.2	$4.8	RS-components
N-Channel MOSFET	**N-Channel MOSFET, 10 A, 40 V, 8-Pin SOIC Vishay**	4	$1.4	$5.6	RS-components

	SI4840BDY-T1-GE3				
Resistors	220 Ω through hole resistor	8	$0.15	$1.2	RS-components
Resistors	1k Ω through hole resistor	4	$0.15	$0.6	RS-components
Resistor	**500 mΩ Thick Film Resistor 20W ±1% PWR220T-20-R500F**	4	$3.85	$15.4	RS-components
Potentiometer	**Linear 25 Ω potentiometer**	4	$3.25	$13	RS-components
PCB terminal block	2-way 5mm	8	$0.5	$4	RS-components
BNC coaxial Connectors	Right angle BNC jacks	4	$2.5	$10	RS-components
Total cost for 4 stimulation LEDs and 4 proxy LEDs stimulator				$4,707.2	

Table 8.1| Stimulator electronics component BoM

For this spatial stimulator, similar optical components were used to combine LED lights before condensing them onto light fibres, directly orientated on the DLP chip within the LCrs. Then each LCrs output needs to be combine on a beamsplitter before being projected onto a screen (Fig 4.3).

Description	Component	Number	Unit price	Total	Source of materials
LCr mounting components (x2: RGB & UV units)					
x-y stage	13mm translational stage	4	$236	$944	ThorLabs
z stage	13mm translational stage	2	$690	$1380	ThorLabs
External LED units (x2: RGB & UV units)					
Red LED	B5B-434-TY	1	~$5	~$5	Roithner
Green LED	RLS-5B475-S	1	~$5	~$5	Roithner
Blue LED	VL415-5-15	1	~$5	~$5	Roithner
UV LED	XSL-365-5E	1	~$5	~$5	Roithner
Plano-convex lens	f=25mm	4	$51	$204	ThorLabs
Red LED filter	FF01-586/20 BrightLine HC	1	$394	$394	AHF
Green LED filter	ET 480/40	1	$403	$403	AHF

Blue LED filter	ET 420/40	1	$406	$406	AHF
UV LED filter	FF01-370/36 BrightLine HC	1	$394	$394	AHF
B/RG Beamsplitter	T 450I LPXR	1	$332	$332	AHF
G/R Beamsplitter	T 560 LPXR	1	$263	$263	AHF
Collimator	5mm LLG Collimating adapter	2	$342	$684	ThorLabs
Light guide	Liquid light guide 5mm 1.2m	2	$491	$982	ThorLabs
Cage System Right-Angle Adapter	LCP30	2	$44	$88	ThorLabs
Cage Plate 30mm	CP02T/M	4	$23	$92	ThorLabs
Cage Plate 60mm	LCP09	2	$45	$90	ThorLabs
Assembly Rod	ER4	16	$7	$112	ThorLabs
Assembly Rod	ER6	4	$9	$33	ThorLabs
Assembly Rod	ER8	4	$12	$46	ThorLabs
LCr beams projection system					
U/RGB Beamsplitter	T 400 LP	1	$263	$263	AHF
Bi-convex lens	f = 50mm LB1844-ML	2	$40	$80	ThorLabs
Achromatic doublet lens	f = 50mm ACA254-050-A	1	$524	$524	ThorLabs
Achromatic doublet lens	f = 100mm AC508-100-A-ML	1	$148	$148	ThorLabs
Cage cube 60mm	LC6W	1	$146	$146	ThorLabs
Cage System Right-Angle	LCP30	4	$44	$176	ThorLabs

Adapter					
Cage Plate 30mm	CP02T/M	1	$23	$23	ThorLabs
Assembly Rod	ER4	4	$7	$27	ThorLabs
Assembly Rod	ER12	4	$17	$68	ThorLabs
Total cost for 4 stimulation LEDs				$8,322	

Table 8.2| Stimulator optical component BoM

8.2 – QDSpy

QDSpy is a software for generating and presenting stimuli for visual neuroscience. It was developed in the former department of biomedical optics at the Max Planck Institute for medical research in Heidelberg and was mainly written by Thomas Euler. QDSpy is open source project, the source code and documentation can be found on the online repository http://qdspy.eulerlab.de/. It includes a graphical user interface (GUI), which facilitates spatial stimulus alignment, stimuli presentation and LCr individual and coupled control. A complete documentation for the installation, configuration and operation of QDSpy can be found on the online repository, along the instructions on how to generate stimulus scripts with the available libraries.

The following section was originally detailed in the project publication (Franke et al. 2019):

QDSpy relies on the frame sync of the graphics card/driver for stimulus display. By measuring the time required to generate the next frame, the software can detect dropped frames and warn the user of timing inconsistencies, which cannot be altogether excluded on a non-real-time operating system like Windows. Such frame drops, including all other relevant events (e.g. which stimulus was started when, was it aborted etc.) as well as user comments are automatically logged into a file. To account for any gamma correction performed by the LCr firmware when in video mode and/or by non-linearities of the LEDs/LED drivers, each measured LED's intensity curve generates a lookup table (LUT) that is then used in QDSpy to linearise the colour channels (Materials and methods).

As default, the LCr runs in ‘video mode’, where it behaves like an HDMI-compatible display (60 Hz, 912 × 1,140 pixels). In this mode, each colour channel in an RGB frame (3 × 8 = 24 bitplanes) is assigned to one of the 3 LCr LEDs via the QDSpy software. It is possible (and supported by QDSpy) to reconfigure the LCr firmware and run it in the so-called ‘pattern mode’, which, for instance, allows trading bit depth for higher frame rates and assigning each of the 24 bitplanes of every frame to an arbitrary combination of LEDs.

The stimulation software generates digital synchronisation markers to align presented stimuli with recorded data. In addition to digital I/O cards, QDSpy supports Arduino boards as digital output device. While the software attempts generating the synchronisation marker at the same time as when presenting the stimulus frame that contains the marker, a temporal offset between these two events in the tens of millisecond range cannot be avoided. We found this offset to be constant for a given stimulation system, but dependent on the specific combination of PC hardware, digital I/O device, and graphic cards. Therefore, the offset must be measured (e.g. by comparing synchronisation marker signal and LCr output measured by a fast photodiode) and considered in the data analysis.

When two LCrs are combined, QDSpy opens a large window that covers both LCr ‘screens’ and provides each LCr with ‘its’ chromatic version of the stimulus (screen overlay mode). To this end, the software accepts colour definitions with up to six chromatic values and assigns them to the six available LEDs (three per LCr). For example, the first LCr provides the red, green and blue channels, whereas the second LCr adds the UV channel. Here, QDSpy presents the stimulus’ RGB-components on the half of the overlay window assigned to the first LCr and the stimulus’ UV-component on the half of the overlay window assigned to the second LCr.